

NASA TECHNICAL
MEMORANDUM

N72-26010
NASA TM X-62,152

**CASE FILE
COPY**

NASA TM X-62,152

FEASIBILITY STUDY OF A BIDIRECTIONAL JET FLAP DEVICE FOR
APPLICATION TO HELICOPTER ROTOR BLADES
PHASE II: LIFT CONTROLLER DEVELOPMENT

Raymond E. Rose, Tom M. Wynn, Gary A. Smith, and Glen L. Merrill

Honeywell Inc.
St. Paul, Minnesota 55113

and

Ames Research Center
and
U.S. Army Air Mobility R&D Laboratory
Moffett Field, Calif. 94035

April 1972

FEASIBILITY STUDY OF A BIDIRECTIONAL JET FLAP
DEVICE FOR APPLICATION TO HELICOPTER ROTOR BLADES

Phase II: Lift Controller Development

By Raymond E. Rose, Tom M. Wynn*, Gary A. Smith
and Glen L. Merrill

*U.S. Army Air Mobility R&D Laboratory,
Moffett Field, California 94035

and

Honeywell Inc.
Systems and Research Division
Research Department
St. Paul, Minnesota 55113

April 1972

NATIONAL AERONAUTICS AND SPACE ADMINISTRATION

FOREWORD

This is the final report describing the work performed for the Ames Directorate, U.S. Army Air Mobility Research and Development Laboratory, under Contract Number NAS 2-4389. The feasibility of using a fluidically controlled, bidirectional jet flap called the Variable Deflection Thruster (VDT) to improve helicopter rotor blade performance was studied. The program was conducted jointly by Honeywell and AAMRDL. The contract monitor is Mr. Thomas Wynn.

The authors wish to express their gratitude to Mr. H. M. Melrose for his contribution to the experimental program; to Messrs. N. E. Miller, S. M. Johnson, and K. C. Van Langen for their assistance in analyzing the results of the experimental work; and especially to Mr. J. M. Hammer for his analytical treatment of the lift controller presented in the Appendix.

ABSTRACT

A bidirectional jet flap device called the Variable Deflection Thruster (VDT) has been investigated for possible application to helicopter rotors. This investigation included the development and testing of a fluidic lift control system for the VDT-blade model making use of the Phase I test result that VDT-blade lift can be sensed from the differential pressure at midchord. This study constitutes Phase II of a long-range program to develop blown control techniques for stabilizing the higher harmonic modes of helicopter rotors.

Wind tunnel tests were conducted using a three-sectioned, two-dimensional VDT-blade model having individually controlled VDT jet flaps in each section. Steady-state tests were conducted without the fluidic lift controller (open loop) for both full-span blowing and for the model center section blowing only. Steady-state tests were conducted with the center section blowing only using the fluidic lift controller (closed-loop) to control the lift on the model center section. Dynamic tests were conducted using the complete model with the VDT jet in the model center section oscillating at various frequencies and also using the model center section alone on a single endplate to obtain finite-aspect-ratio effects. Fair agreement was obtained between theory and experimental results.

The fluidic lift controller maintained approximately constant lift on the VDT-blade at zero angle of attack ($\theta_j > 0$) for a dynamic pressure range from approximately 10 to 90 psf. Since the control system gain was less than designed for, the ability of the lift controller to maintain constant lift decreased with increasing angle of attack. However, the test results proved the concept feasibility of a fluidic lift controller. The dynamic test results indicate that the ratio of dynamic lift to steady-state lift increased with increasing VDT jet oscillation frequency more rapidly for finite than for infinite aspect ratio. These results are consistent with those shown in reference 1.

LIST OF SYMBOLS

A_c	Effective area of first preamplifier orifice (control port)
A_o	Effective area of pressure tap orifice for outbleed at model surface
A_s	Effective area of bias orifice in outbleed supply
AR	Aspect ratio
B, C	Coefficients in Spence's equation (ref. 5)
b	Nozzle exit width
b_T	Airfoil semi-span
C_D	Drag coefficient
C_{Dh}	Drag coefficient of hypothetical unblown wing
C_{DL}	Lift-produced drag coefficient
C_{D_o}	Profile and skin-friction drag coefficient
ΔC_D	Drag coefficient difference between blown and unblown wing
C_L	Lift coefficient
$ C_L $	Absolute value of lift coefficient for jet angle oscillations (dynamic lift coefficient)
$C_{M_{c/4}}$	Quarter-chord moment coefficient
$C_{M_{LE}}$	Leading edge moment coefficient
C_N	Normal force coefficient
C_P	Pressure coefficient
ΔC_P	Difference in pressure coefficient between top and bottom of the airfoil
$\Delta C_{P_{c/2}}$	Pressure coefficient differential at midchord

C_{μ}	Blowing coefficient
\bar{C}_{μ}	Total VDT blowing coefficient, $C_{\mu} = C_{\mu 1} + C_{\mu 2}$
c	Airfoil chord
D	Drag
f	Jet angle oscillation frequency
G	Gain of fluidic control system
L	Lift
ℓ	Lift per unit airfoil surface area
M_{∞}	Free-stream Mach number
N_{F_1}	Front component of normal force as measured by the LTV balance system
N_{F_2}	Rear component of normal force as measured by the LTV balance system
P_1	Pressure in top branch of downstream outbleed network
P_2	Pressure in bottom branch of downstream outbleed network
P_1'	Midchord pressure on top surface of model
P_2'	Midchord pressure on bottom surface of model
P_{o_1}	Pressure in top VDT tank
P_{o_2}	Pressure in bottom VDT tank
P_{∞}	Free-stream static pressure
ΔP	Difference in pressure between top and bottom of airfoil
$\Delta P_{c/2}$	Pressure differential at airfoil midchord
ΔP_{OB}	Pressure differential in the outbleed network of the fluidic control system
ΔP_{ref}	Set reference pressure differential for the fluidic control system
ΔP_T	VDT tank pressure differential ($P_{o_1} - P_{o_2}$)

q, q_∞	Free-stream dynamic pressure
R_e	Reynolds number
S	Airfoil surface area
T	Jet thrust
V	Free-stream velocity
V_T	Relative velocity
$[VDT]$	Transfer function for VDT jet angle
x/c	Ratio of distance from airfoil leading edge to airfoil chord length
y/b_T	Ratio of distance from airfoil root to airfoil semi-span

Greek Letters

α	Angle of attack
γ	Ratio of specific heats (1.4 for air)
λ	Percentage of VDT jet blowing that results in drag reduction
θ_j	VDT jet angle downstream of cylinder surface measured from the centerline to the position of maximum jet velocity
θ_{jf}	VDT jet angle obtained from force measurements under static conditions, $\theta_{jf} = \tan^{-1} (L/D)$ ($\theta_{jf} \approx \theta_j$)
θ_{jm}	Mean jet angle during jet angle oscillation
$\Delta\theta_j$	Maximum jet angle amplitude for oscillation
$ \Delta\theta_j $	Absolute value of maximum jet angle amplitude
ω	Reduced jet angle oscillation frequency, $2\pi fc/V$

CONTENTS

	Page
FOREWORD	iii
ABSTRACT	iv
LIST OF SYMBOLS	v
INTRODUCTION	1
FLUIDIC CONTROL SYSTEM DEVELOPMENT FOR VDT-BLADE	4
LIFT CONTROL	
Lift Sensing	4
Control Loop Design	4
Amplifier Development	11
Preliminary Tests of Fluidic Control System	19
Outbleed system tests	19
Open-loop testing for operational limitations	19
HELICOPTER VDT-BLADE MODEL MODIFICATION AND	25
INSTRUMENTATION	
WIND TUNNEL TEST PROGRAM	29
Steady-State Tests (Open-Loop)	29
Steady-State Tests with Lift Controller (Closed-Loop)	30
Dynamic Tests	30
Data Reduction Method	31
VDT-BLADE MODEL TEST RESULTS	33
Steady-State Tests (Open-Loop)	33
Nonblowing characteristics	33
Full-span blowing	37
Full-span, center-section blowing only	57
Steady-State Tests with Lift Controller (Closed-Loop)	64
Fluidic amplifier performance	70
Outbleed system and controller gain	70
Model spanwise lift characteristics	73
Lift controller results	77
Dynamic Tests	83
CONCLUSIONS	90
REFERENCES	91
APPENDIX - LIFT CONTROLLER MATH MODEL	

ILLUSTRATIONS

Figure		Page
1	Basic VDT Configuration	2
2	Theoretical and Experimental Pressure Distributions for the Helicopter VDT-Blade Model	5
3	Midchord Pressure Differential versus Lift per Unit Blade Area - Center Section with End Plates	8
4	Helicopter Control System	9
5	Fluidic Control Loop	10
6	Control System Gain as a Function of Lift Variation	12
7	Fluidic Control System Schematic	13
8	Fluidic Control System Amplifier Components and Assembled Amplifiers	16
9	VDT Fluidic Control System Assembly	17
10	Fluidic Control System Installed in Center Section of Helicopter VDT-Blade Model	18
11	Wing Model in Subsonic Wind Tunnel	20
12	Preamplifier Output versus Angle of Attack for Midchord ΔP on NACA 0012 Airfoil	21
13	Gain Curves for Outbleed Preamplifier System	22
14	Pressure Gain Curve for Complete VDT Control System	24
15	Compliance Joint Assembly	26
16	Helicopter VDT-Blade Mounted in AAMRDL's 7 x 10-foot Wind Tunnel	28
17	VDT Jet Angle as a Function of VDT Tank Pressure Difference	32
18	VDT-Blade Lift Coefficient as a Function of Angle of Attack - Full Span, No Blowing	34
19	VDT-Blade Drag Coefficient as a Function of Angle of Attack - Full Span, No Blowing	35

Figure		Page
20	VDT-Blade Leading-Edge Moment Coefficient as a Function of Angle of Attack - Full Span, No Blowing	36
21	VDT-Blade Quarter-Chord Moment Coefficient as a Function of Angle of Attack - Full Span, No Blowing	36
22	Lift Coefficient as a Function of Blowing Coefficient - Full-Span Blowing, $\alpha = 0$	38
23	Lift Coefficient as a Function of Blowing Coefficient - Full-Span Blowing, $\alpha = 4$ degrees	39
24	Lift Coefficient as a Function of Blowing Coefficient - Full-Span Blowing, $\alpha = 8$ degrees	40
25	Lift Coefficient as a Function of Blowing Coefficient - Full-Span Blowing, $\alpha = 12$ degrees	41
26	Drag Coefficient as a Function of Blowing Coefficient - Full-Span Blowing, $\alpha = 0$	42
27	Drag Coefficient as a Function of Blowing Coefficient - Full-Span Blowing, $\alpha = 4$ degrees	43
28	Drag Coefficient as a Function of Blowing Coefficient - Full-Span Blowing, $\alpha = 8$ degrees	44
29	Drag Coefficient as a Function of Blowing Coefficient - Full-Span Blowing, $\alpha = 12$ degrees	45
30	Linearized Drag Polar for Unblown VDT-Blade	47
31	Drag Reduction Due to Blowing - Full-Span Blowing, $\alpha = 0$	48
32	Drag Reduction Due to Blowing - Full-Span Blowing, $\alpha = 4$ degrees	49
33	Drag Reduction Due to Blowing - Full-Span Blowing, $\alpha = 8$ degrees	50
34	Drag Reduction Due to Blowing - Full-Span Blowing, $\alpha = 12$ degrees	51
35	Quarter-Chord Moment Variation with Blowing Coefficient - Full-Span Blowing, $\alpha = 0$	52
36	Quarter-Chord Moment Variation with Blowing Coefficient - Full-Span Blowing, $\alpha = 4$ degrees	53

Figure		Page
37	Quarter-Chord Moment Variation with Blowing Coefficient - Full-Span Blowing, $\alpha = 8$ degrees	54
38	Quarter-Chord Moment Variation with Blowing Coefficient - Full-Span Blowing, $\alpha = 12$ degrees	55
39	Quarter-Chord Moment Variation with Blowing Coefficient - Full-Span Blowing, $\theta_j = 30$ degrees	56
40	Lift Coefficient as a Function of Blowing Coefficient - Center-Section Blowing Only, $\alpha = 0$	58
41	Lift Coefficient as a Function of Angle of Attack - Full-Span Blowing and Center-Section Blowing Only	59
42	Lift Coefficient as a Function of Blowing Coefficient - Full-Span Blowing and Center-Section Blowing Only, $\alpha = 0$	60
43	Lift Coefficient as a Function of Blowing Coefficient - Full-Span Blowing and Center-Section Blowing Only, $\alpha = 4$ degrees	61
44	Lift Coefficient as a Function of Blowing Coefficient - Full-Span Blowing and Center-Section Blowing Only, $\alpha = 8$ degrees	62
45	Lift Coefficient as a Function of Blowing Coefficient - Full-Span Blowing and Center-Section Blowing Only, $\alpha = 12$ degrees	63
46	Drag Reduction Due to Center-Section Blowing Only - $\alpha = 0$	65
47	Drag Reduction Due to Center-Section Blowing Only - $\alpha = 4$ degrees	65
48	Drag Reduction Due to Center-Section Blowing Only - $\alpha = 8$ degrees	66
49	Drag Reduction Due to Center-Section Blowing Only - $\alpha = 12$ degrees	66
50	Quarter-Chord Moment Due to Center-Section Blowing Only - $\alpha = 0$	67
51	Quarter-Chord Moment Due to Center-Section Blowing Only - $\alpha = 4$ degrees	67
52	Quarter-Chord Moment Due to Center-Section Blowing Only - $\alpha = 8$ degrees	68

Figure		Page
53	Quarter-Chord Moment Due to Center-Section Blowing Only - $\alpha = 12$ degrees	68
54	Quarter-Chord Moment Due to Center-Section Blowing Only - $\theta_j = 30$ degrees	69
55	Fluidic Amplifier Gains from Downstream Side of Outbleed System to VDT Tanks	71
56	Backpressures in Outbleed System Compared to Wing $\Delta P_c/2$	72
57	Control System Gain for Changing q-Tests at Constant α	74
58	Theoretical Lift Values Produced by Fluidic Control System on Two-Dimensional VDT-Blade Model	75
59	Spanwise Midchord Pressure Distribution - 46-percent Blown Span, Infinite-Aspect-Ratio Wing	76
60	Center-Section Lift as a Function of $\Delta P_c/2$ for Center-Section Blowing Only	78
61	VDT-Blade Lift Variation with Free-Stream Dynamic Pressure - $\alpha = 0$	79
62	VDT-Blade Lift Variation with Free-Stream Dynamic Pressure - $\alpha = 4$ degrees	80
63	VDT-Blade Lift Variation with Free-Stream Dynamic Pressure - $\alpha = 8$ degrees	81
64	VDT-Blade Lift Variation with Free-Stream Dynamic Pressure - $\alpha = 12$ degrees	82
65	Normal Force as a Function of Jet-Angle Oscillation Frequency	84
66	Variation of Dynamic Lift with Jet-Angle Oscillation Frequency	85
67	Variation of Uncorrected Coefficient of Lift Amplitude with Reduced Frequency - $\alpha = 0$ and 12 degrees	87
68	Jet-Angle Correction Factor	87
69	Variation of Corrected Coefficient-of-Lift Amplitude with Reduced Frequency - $\alpha = 0$ and 12 degrees	88

Figure		Page
70	Steady-State Lift-Coefficient/Blowing-Coefficient Relationship for Tests of Center Section with a Single Endplate	88
71	Variation of Normalized Coefficient-of-Lift Amplitude with Reduced Frequency - $\alpha = 0$	89

FEASIBILITY STUDY OF A
BIDIRECTIONAL JET FLAP DEVICE
FOR APPLICATION TO HELICOPTER ROTOR BLADES

Phase II: Lift Controller Development

by

Raymond E. Rose
Tom M. Wynn*
Gary A. Smith
Glen L. Merrill

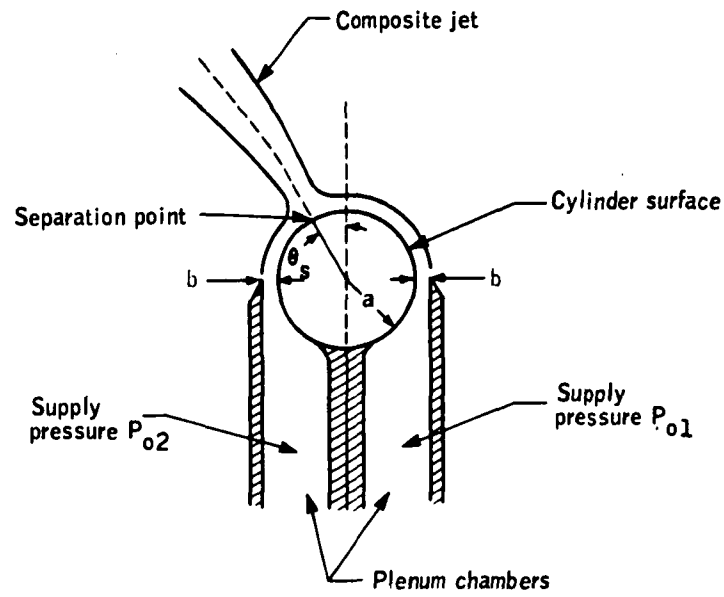
INTRODUCTION

This is the final report of Phase II work in a program directed toward the development of a jet-flap device and fluidic lift control system applicable to helicopter rotor blades.

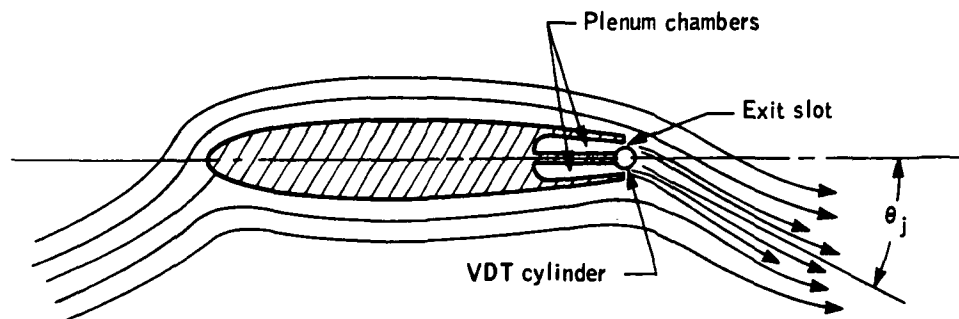
The first phase of investigation (ref. 2) provided preliminary and basic information on the steady-state and dynamic characteristics of a helicopter-blade model incorporating a jet-flap device called the Variable Deflection Thruster (VDT). The basic VDT configuration is shown in Figure 1. During Phase I, a two-dimensional helicopter VDT-blade model (NACA 0012) having a 2-foot chord was designed, fabricated, and wind tunnel tested in AAMRDL's 7 x 10-foot wind tunnel at the Ames Research Center. The model is constructed in three equal sections to allow for control of different blowing rates and jet angles. Complete details of the model are given in reference 2.

Steady-state results showed that the VDT is an effective lift-producing device which provides simultaneous drag reduction. It was also found that the VDT-blade lift can be sensed from the differential pressure at the airfoil midchord. Dynamic results indicated that the ratio of dynamic lift to steady-state lift increases with increasing VDT jet oscillation frequency for a constant oscillation angle.

* Ames Directorate, AAMRDL



(a) Cylindrical VDT concept



(b) Airfoil section with VDT trailing edge

Figure 1. Basic VDT Configuration

The major objective of the Phase II investigation was to develop a fluidic system for sensing and controlling the lift on a VDT helicopter rotor blade. To accomplish this task, a fluidic control system employing the VDT was designed to maintain constant lift on the helicopter rotor blade independent of changes in angle of attack or free-stream velocity. Fluidic amplifier cascades were developed to meet the design requirements. The fluidic control system was installed in the center section of the helicopter VDT-blade model and wind tunnel tested in AAMRDL's 7 x 10-foot wind tunnel at the Ames Research Center. The results of these tests are presented and discussed in this report.

FLUIDIC CONTROL SYSTEM DEVELOPMENT FOR VDT-BLADE LIFT CONTROL

Lift Sensing

The method developed and used in the lift controller design to sense lift is based on Küchemann's approach to calculating the pressure distribution over an airfoil with trailing edge blowing. A detailed discussion of the method is presented in reference 3. Küchemann's method has been successfully applied to elliptical airfoils both by himself (ref. 3) and by Yuan, et al. (ref. 4).

Calculations were made to predict the VDT-blade model surface pressure distribution using the equations developed by Küchemann (ref. 3). The results of several pressure calculations are presented in Figure 2 for a number of combinations of input variables (C_L , α and \bar{C}_μ) and compared with experimental data from the Phase I tests (ref. 2). The distributions are presented in the form of pressure coefficient differences, ΔC_P , between the top and bottom of the airfoil. Good agreement is obtained between the calculated and experimental results.

The calculated pressure distributions predict that the pressure difference between the top and bottom of the airfoil at midchord is directly proportional to lift. Experimental data from reference 1, shown in Figure 3, tend to verify the predicted linear relationship. Therefore, the lift control system was designed to sense the lift on the VDT-blade model simply by measuring the pressure difference across the midchord of the airfoil.

Control Loop Design

A block diagram of the control system, designed as it would operate on a helicopter, is shown in Figure 4. The pilot's input command (commanding

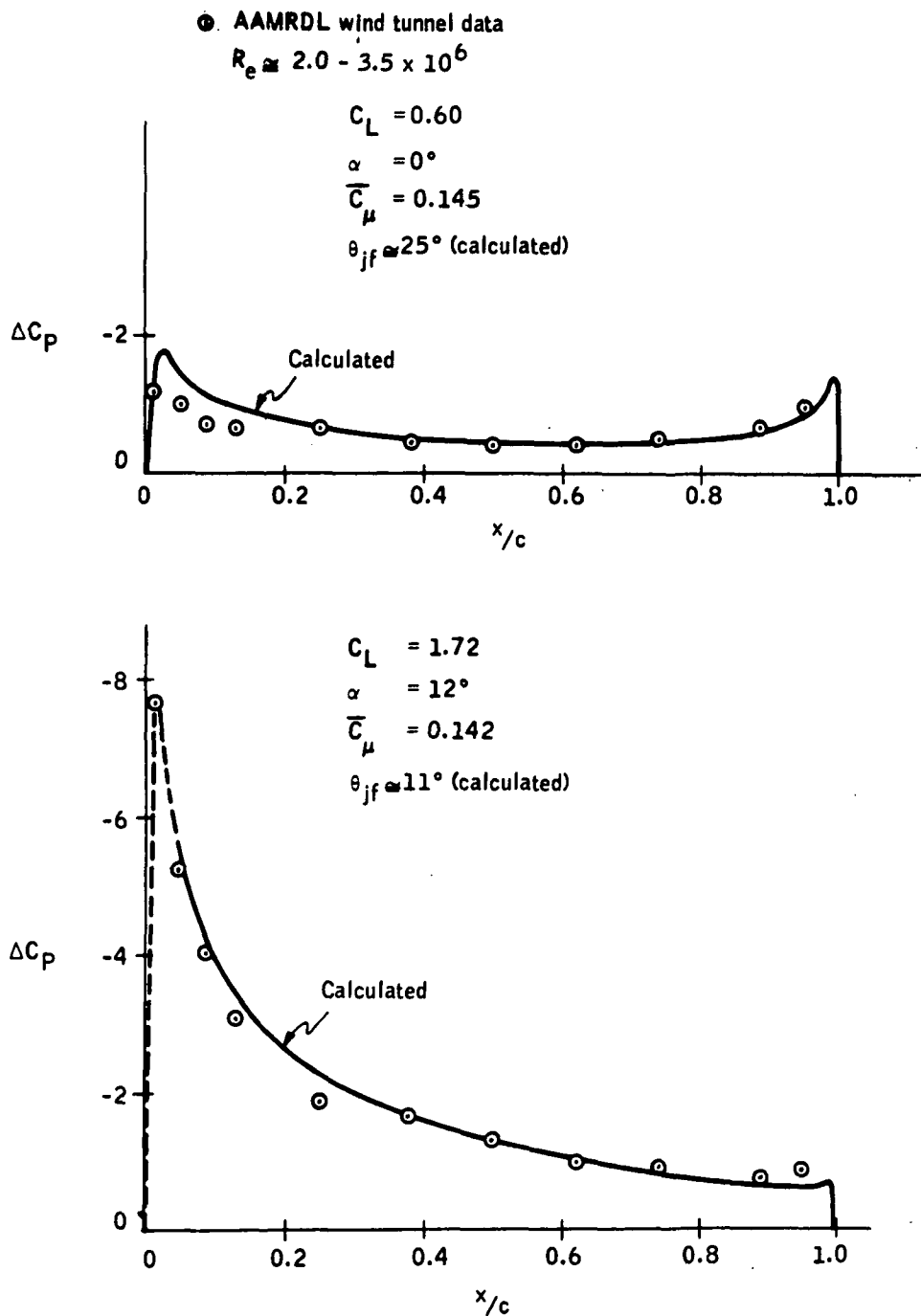


Figure 2(a). Theoretical and Experimental Pressure Distributions for the Helicopter VDT-Blade Model ($C_\mu \approx 0.145$, 0.142)

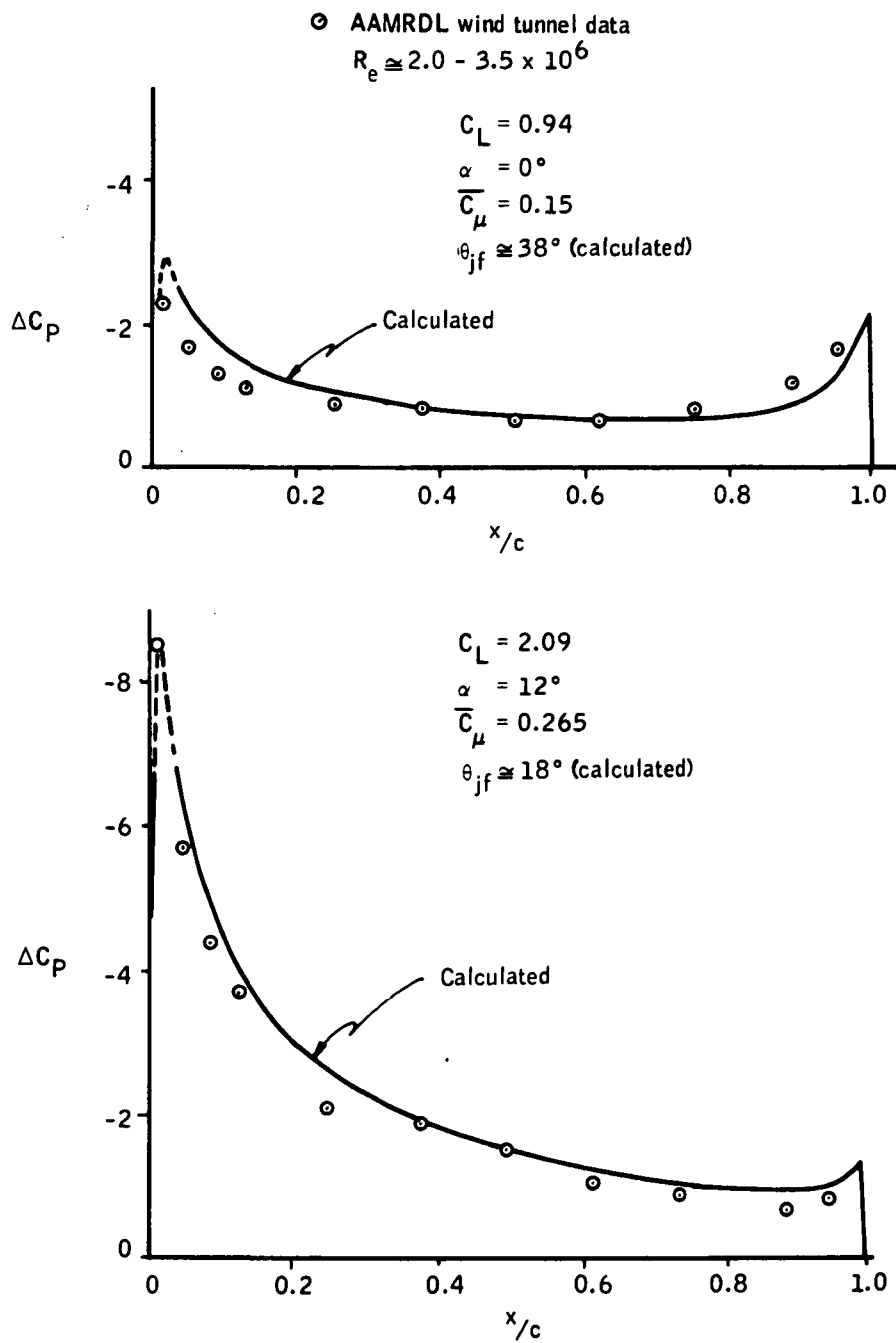


Figure 2(b). Theoretical and Experimental Pressure Distributions for the Helicopter VDT-Blade Model ($C_\mu \approx 0.15$, 0.265)

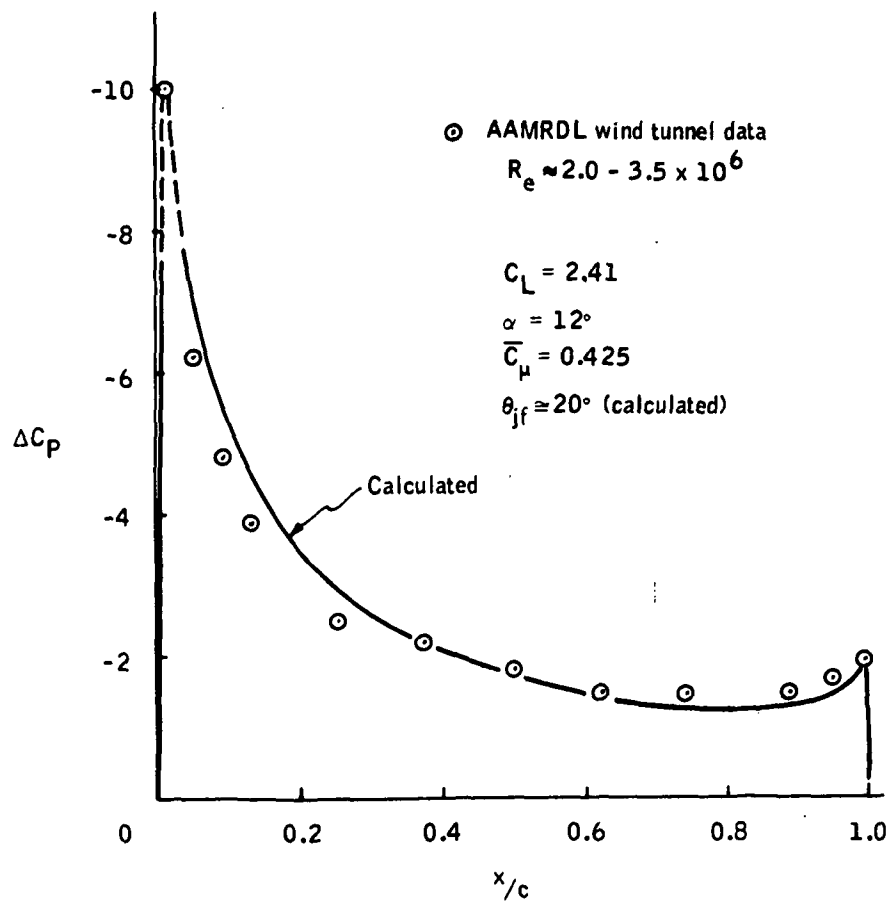


Figure 2(c). Theoretical and Experimental Pressure Distributions for the Helicopter VDT-Blade Model ($C_\mu \approx 0.425$)

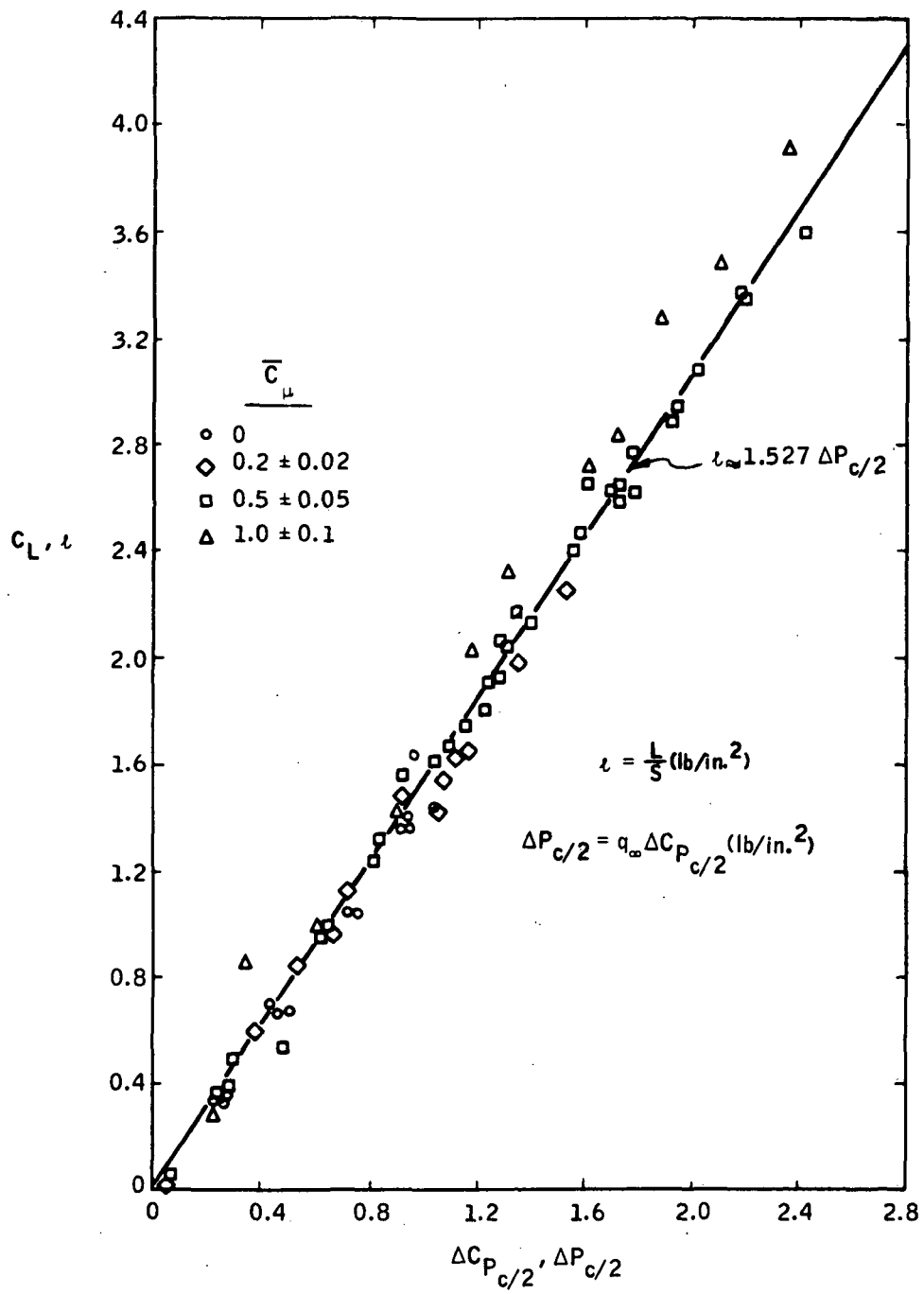


Figure 3. Midchord Pressure Differential versus Lift per Unit Blade Area - Center Section with End Plates (ref. 2)

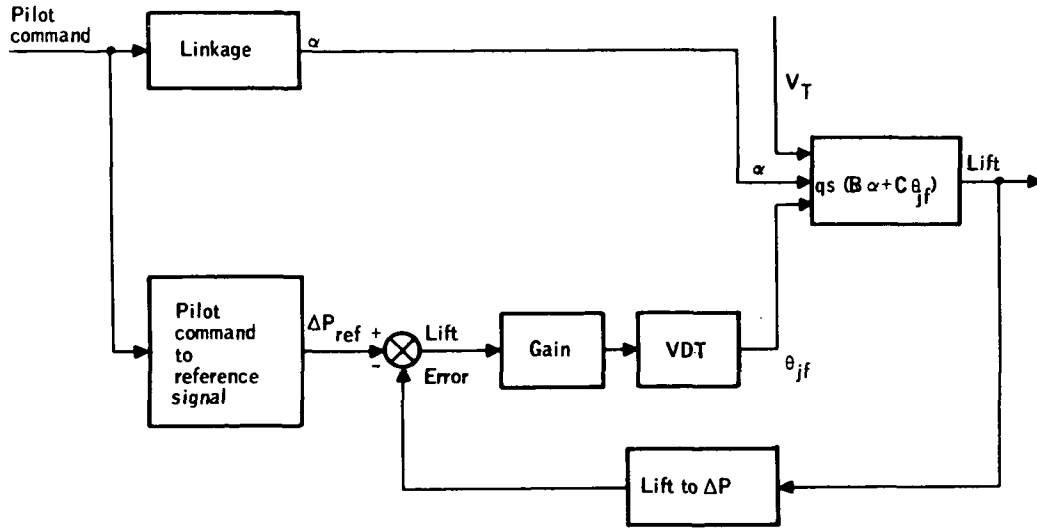


Figure 4. Helicopter Control System

lift) changes the helicopter rotor blade angle of attack, α , through a linkage. This same command also sets the reference signal to the fluidic control system. The commanded angle of attack, the relative velocity over the blade, V_T , and the VDT jet angle, θ_{jf} , combine to produce the lift on the blade.

In the fluidic control loop (Figure 5) pressure taps at the midchord of the VDT-blade surface provide the fluidic signal proportional to lift. This signal is compared with the reference signal, ΔP_{ref} . If an error exists, the resulting signal is amplified and used to deflect the VDT jet, which acts to compensate for the lift error.

Figure 5 is a revised block diagram for operation of the system in the wind tunnel. The gain constants B and C are the coefficients of α and θ_{jf} terms in Spence's coefficient-of-lift equation (ref. 5):

$$\begin{aligned}
 B &= 2\pi + 1.152 \bar{C}_\mu^{1/2} + 1.106 \bar{C}_\mu + 0.051 \bar{C}_\mu^{3/2} \\
 C &= 3.54 \bar{C}_\mu^{1/2} + 0.325 \bar{C}_\mu + 0.156 \bar{C}_\mu^{3/2} \\
 C_L &= B\alpha + C\theta_{jf}
 \end{aligned} \tag{1}$$

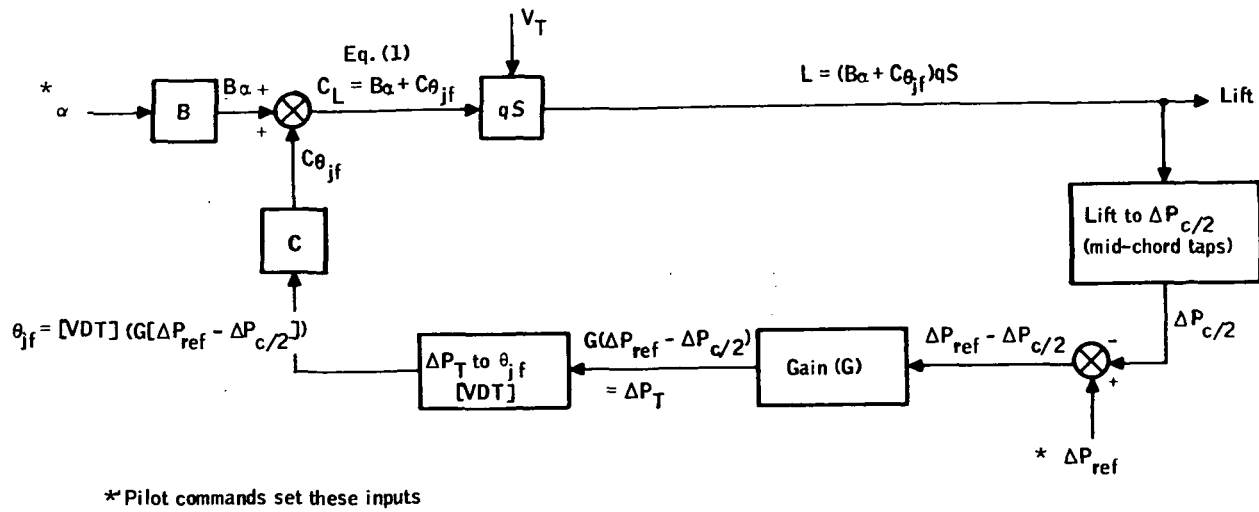


Figure 5. Fluidic Control Loop

The jet blowing coefficient is a function of the plenum chamber pressures. The relation between ΔP_T and θ_{jf} for the VDT jet was obtained from the following approximation:

$$\theta_{jf} = 90^\circ \left(1 - \frac{P_{o2}}{P_{o1}} \right) = 90^\circ \left(\frac{\Delta P_T}{P_{o1}} \right) \quad (2)$$

To avoid flow separation, the range for θ_{jf} was set at $-60^\circ \leq \theta_{jf} \leq 60^\circ$. From the block diagram (Figure 4) the relationship for lift is

$$L = \left(\frac{B \alpha + C \cdot G [\text{VDT}] \frac{\Delta P_{\text{ref}}}{\frac{\Delta P_c}{2}}}{1 + C \cdot G (qS) [\text{VDT}] \frac{\Delta P_c}{2}} \right) qS \quad (3)$$

where [VDT] is the function which transfers the tank pressures to a VDT jet angle according to equation (2).

If the set point is selected so that the VDT angle is zero when the VDT-blade angle of attack is at some set value, then the percentage variation in lift with angle of attack is

$$\frac{\Delta L}{L} = \frac{\Delta \alpha / \alpha}{1 + C \cdot G \left(\frac{\Delta P_{c/2}}{L} \right) [VDT] qS} \quad (4)$$

Equation (4) can be solved to determine the pressure gain, G, needed to maintain lift within a specified limit. Figure 6 shows this relationship for plenum chamber pressures of 50 psig and three air velocities. In this case, a nominal angle of attack of 5 degrees and a variation of ± 10 degrees were used. This figure indicates that relatively high pressure gains will be needed to control lift within reasonable limits. Lower air velocities (M_∞) require higher gains to maintain the same lift control.

Based on the above analysis, a gain (G) of 2000 was selected. Figure 6 shows that a gain of 2000 will give less than 10% variation in lift for values of M_∞ greater than 0.2.

Amplifier Development

Figure 7 is a schematic diagram of the entire fluidic lift control system. The lift control system consists of a fluidic lift-sensing network, an amplifier system, and a VDT configuration. A lift error based on the pressure difference measured by the lift-sensing network and an operator adjusted reference pressure difference, ΔP_{ref} , is computed by a summing amplifier, which is the first stage of the amplifier system. The error signal is amplified by the remainder of the amplifier system and used to deflect the VDT trailing edge jet to compensate for the lift error.

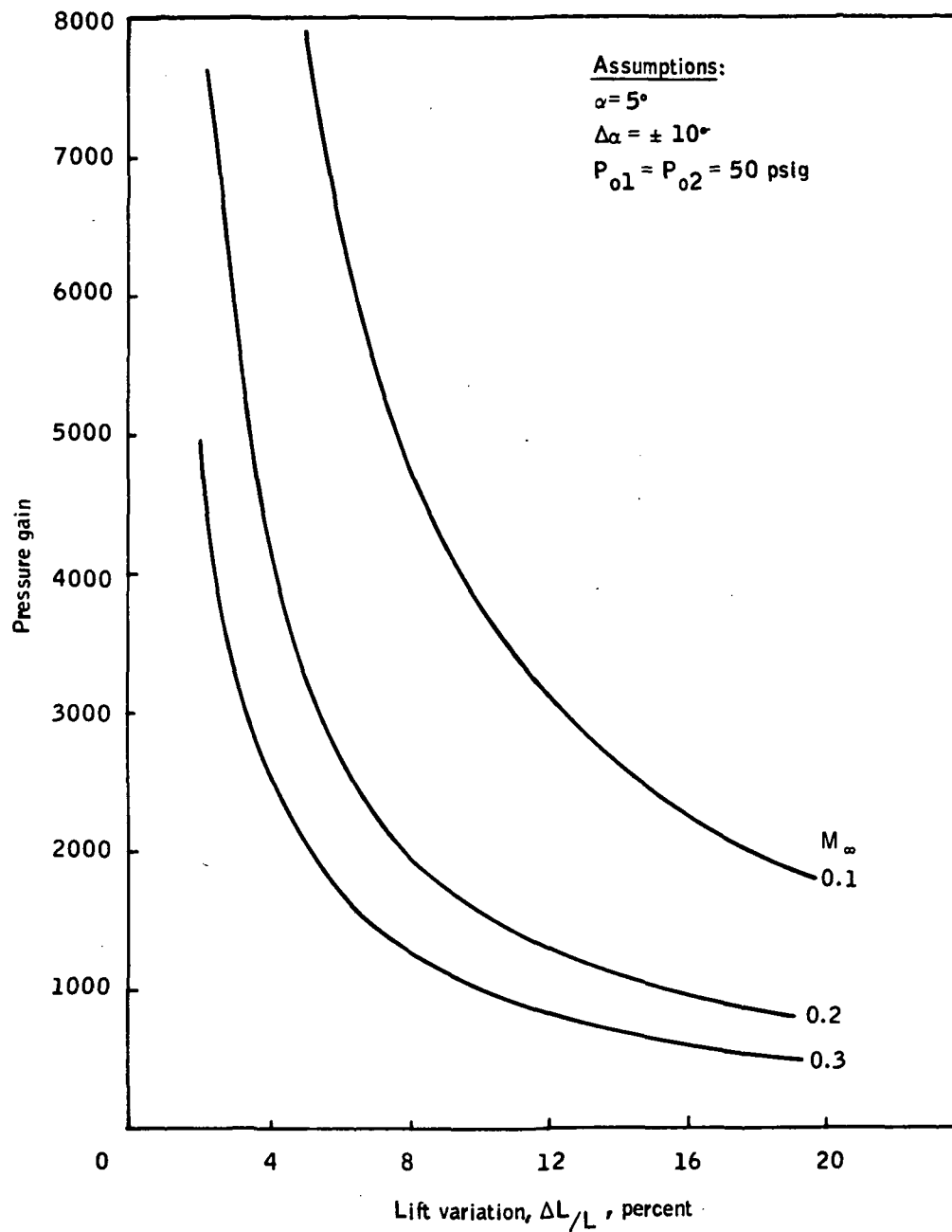


Figure 6. Control System Gain as a Function of Lift Variation

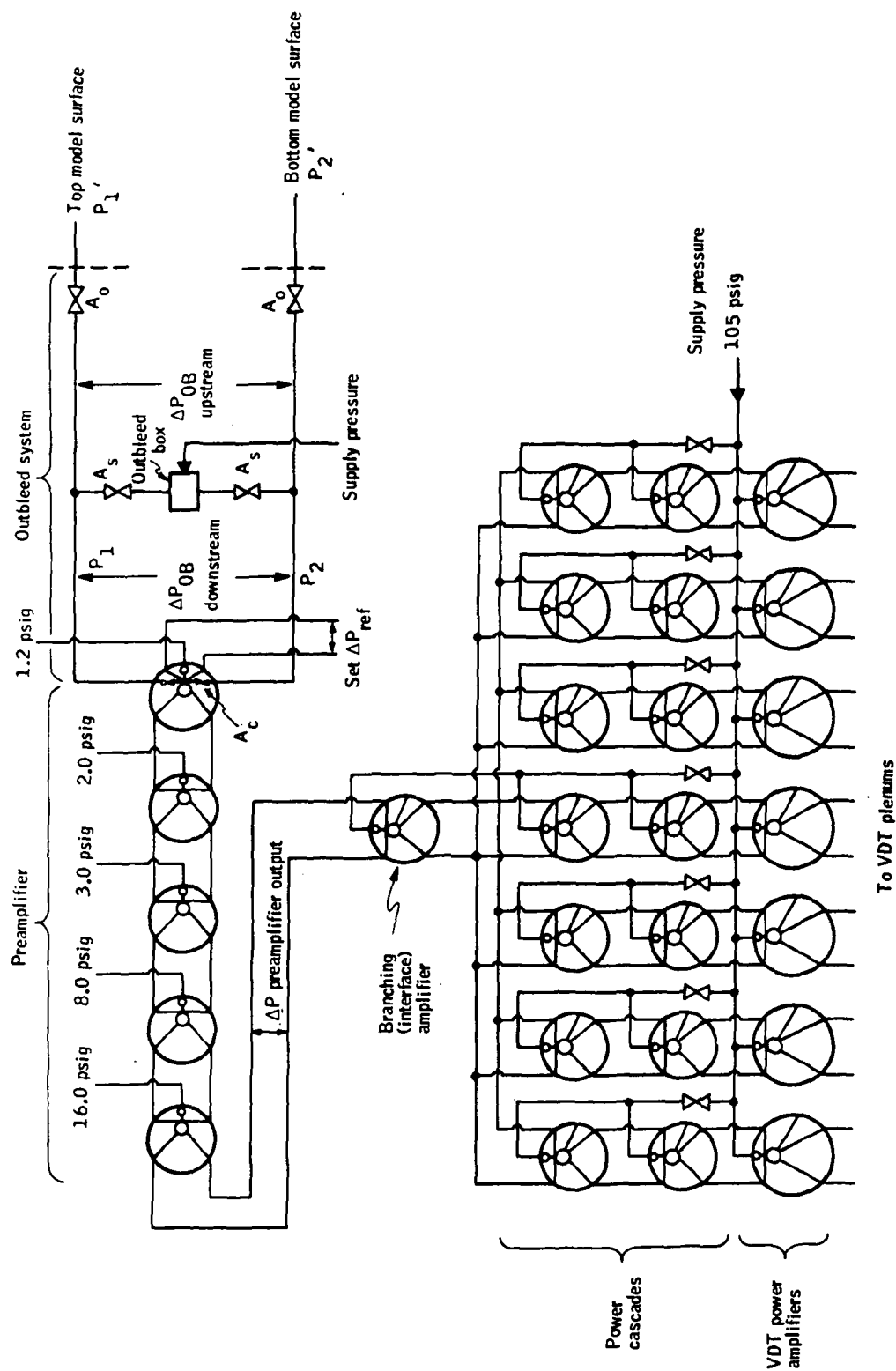


Figure 7. Fluidic Control System Schematic

The two pressure taps used to sense lift on the helicopter VDT-blade model are located at the midchord position on the top and bottom surface of the model. To simulate conditions where it would be required to avoid entraining impurities into the system through the pressure taps, air was exhausted from the taps. Consequently, an outbleed network was devised which provided a signal path from the pressure-sensing ports to the pre-amplifier, as shown in Figure 7. It can be shown that the signal attenuation in the passive resistance or outbleed network is given by

$$\frac{P_2 - P_1}{P'_2 - P'_1} = \frac{1}{\frac{A_s^2 + A_c^2}{A_o^2} + 1} = 0.95 \quad (5)$$

where

P_2, P_1 = pressures downstream of outbleed network

P'_2, P'_1 = pressures upstream of outbleed network

A_s = effective area of bias orifice in outbleed supply

A_o = effective area of pressure tap orifice for outbleed
at blade surface

A_c = effective area of first preamplifier orifice
(control port)

The amplifier system is composed of four sets of amplifiers (Figure 7):

- Preamplifier cascade
- Branching or interface amplifier
- Power cascades
- VDT power amplifiers

The preamplifier consists of five center-dump amplifiers. Four non-summing and one summing amplifier are combined to achieve a gain of approximately 250. The summing amplifier compares the pressure difference measured by the lift sensing network with the reference pressure signal, ΔP_{ref} . The resulting pressure signal is amplified by the remaining non-summing stages of the preamplifier. Amplifier components and the completed preamplifier are shown in Figure 8.

To keep the size of the VDT power amplifier within reasonable limits and to reduce control and airflow problems, seven amplifier units are used to supply the airflow to the VDT plenum tanks. Each amplifier unit consists of a VDT power amplifier with a gain of 2 preceded by a power cascade with a gain of 4. The power cascade is a series combination of two side-vented amplifiers. A completed power cascade-VDT power amplifier unit is shown in Figure 8.

Figure 9 shows the seven amplifier units mounted on the VDT plenum section. Both the power cascades and the VDT power amplifiers are supplied by a common pressure source, but the power cascades are equipped with orifices which drop their supply pressure. The center amplifier unit also has the interface amplifier (interfaces between the preamplifier and the seven power-amplifier cascades) mounted beside the amplifier unit.

Figure 10 shows the outbleed network and amplifier system installed in the center section of the helicopter VDT-blade model. The gain of the assembled system is approximately 2000. Since the amplifiers are vented, holes were drilled in the box beam spar and outside ribs of the center section to allow vented air to escape from the model.

The supply pressures to the control system amplifiers (Figure 9) were adjusted to eliminate noise from the circuit. If high-frequency perturbations are present in the pressure signal during wind tunnel tests, thus introducing system instability, the control system can be stabilized by adding a tank (i. e., capacitive element exhibiting first-order lag) having the appropriate volume.

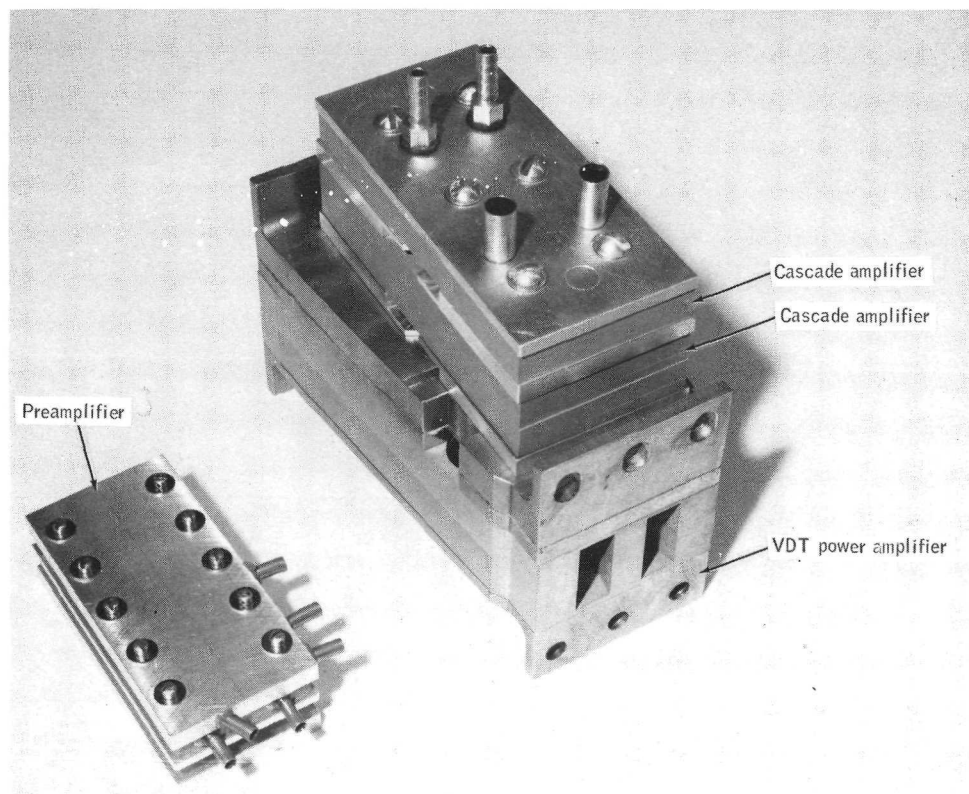
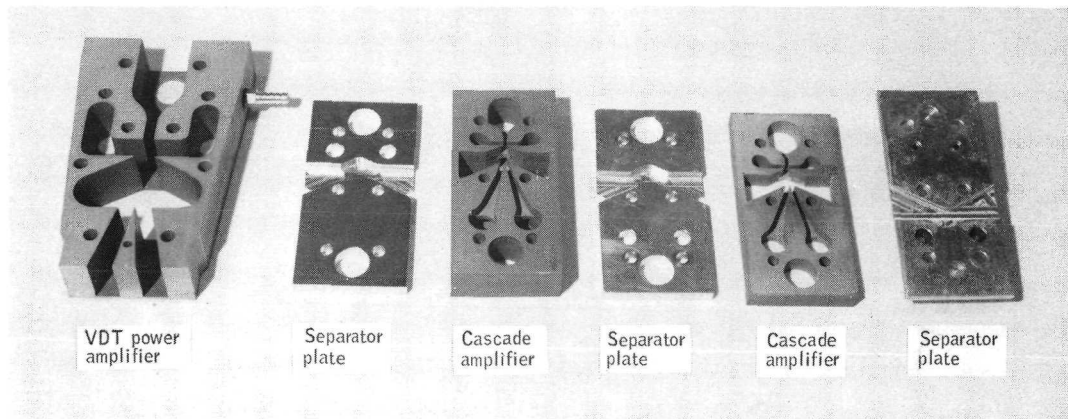


Figure 8. Fluidic Control System Amplifier Components and Assembled Amplifiers

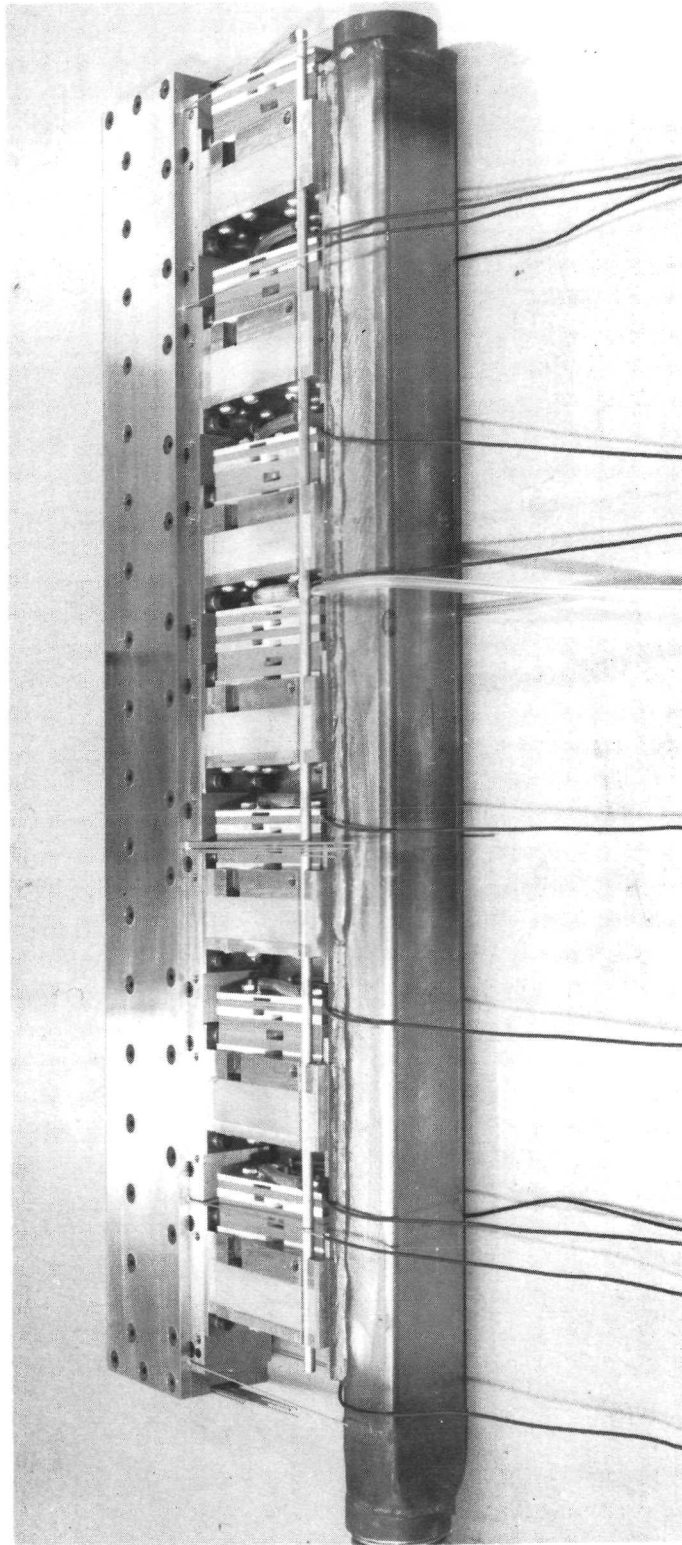
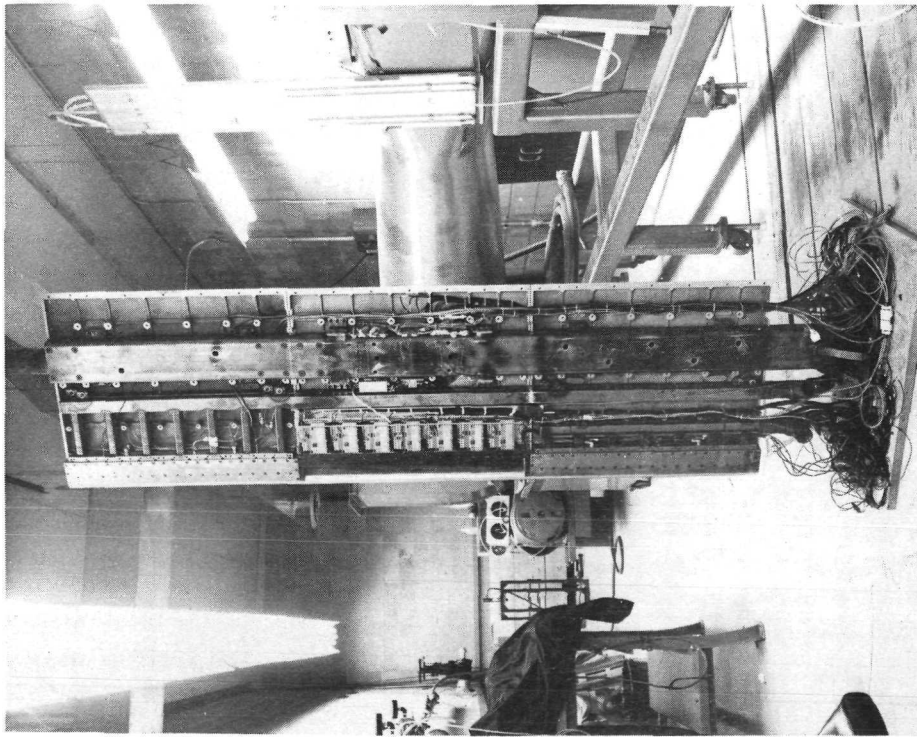
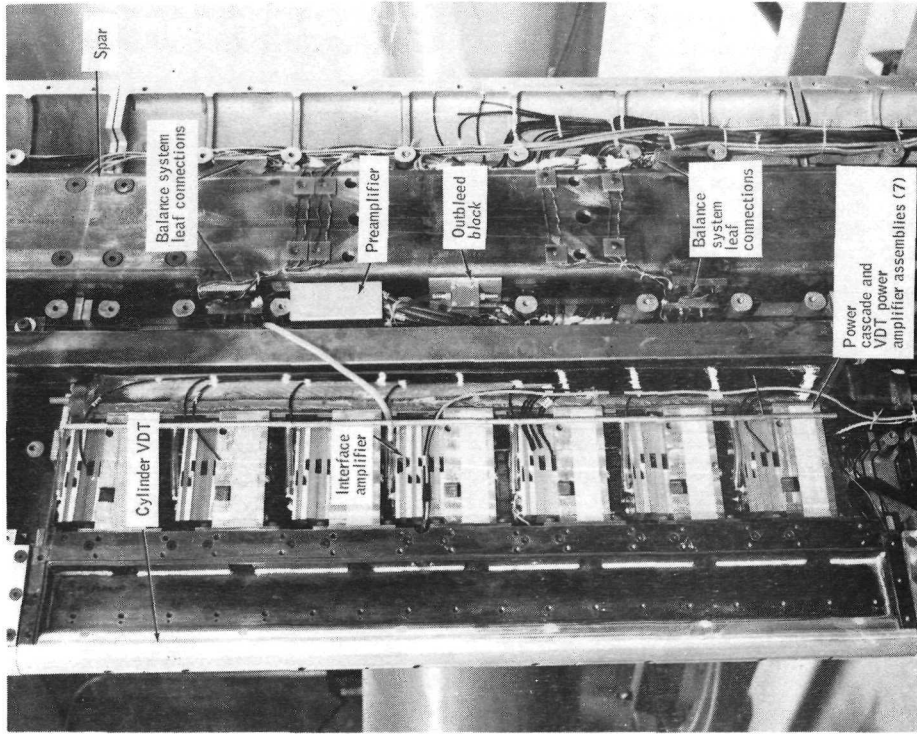


Figure 9. VDT Fluidic Control System Assembly



(a) Overall Internal View of Model



(b) Closeup of Fluidic Control System in Model Center Section

Figure 10. Fluidic Control System Installed in Center Section of Helicopter VDT-Blade Model (internal view)

Preliminary Tests of Fluidic Control System

Outbleed system tests. - The passive resistance network was devised to ensure that the midchord pressure sensing ports remained clear of impurities. Some preliminary tests were completed on this system in combination with the preamplifiers. Tests were conducted in Honeywell's 12 x 17-inch subsonic wind tunnel using the preamplifier and a 6-inch-chord NACA 0012 wooden airfoil model with outbleed orifices at midchord; however, there were no surface pressure taps. Figure 11 shows the model mounted in the wind tunnel test section; a schematic of the outbleed system was shown in Figure 7.

The characteristics of the outbleed system were checked for angles of attack from -5 to +5 degrees (tests were limited to this range by the model's structural characteristics). System noise, gain and linearity with lift were determined. Figure 12 shows the output pressure of the preamplifier as a function of angle of attack of the airfoil. The output of the preamplifier is essentially linear with angle of attack. Since lift should be linear with angle of attack, also, the results indicate that the concept of sensing lift with the outbleed-sensing ports at midchord is feasible.

Figure 13 shows that the gain attenuation through the outbleed system, determined prior to the outbleed orifices, is negligible. The curves represent preamplifier output pressure as a function of pressures upstream and downstream of the outbleed box. The range of angle of attack and other parameters were identical in both cases. The gain for both curves is approximately 300, and the noise amplitude at the output of the preamplifier is roughly 1/4 psi peak-to-peak.

Open-loop testing for operational limitations. - After the preliminary tests of the outbleed system were completed, the entire fluidic control system was installed in the center section of the VDT-blade model and taken to the University of Minnesota Rosemount Aeronautical Laboratories for further testing. Since wind tunnel facilities were not of adequate size, complete

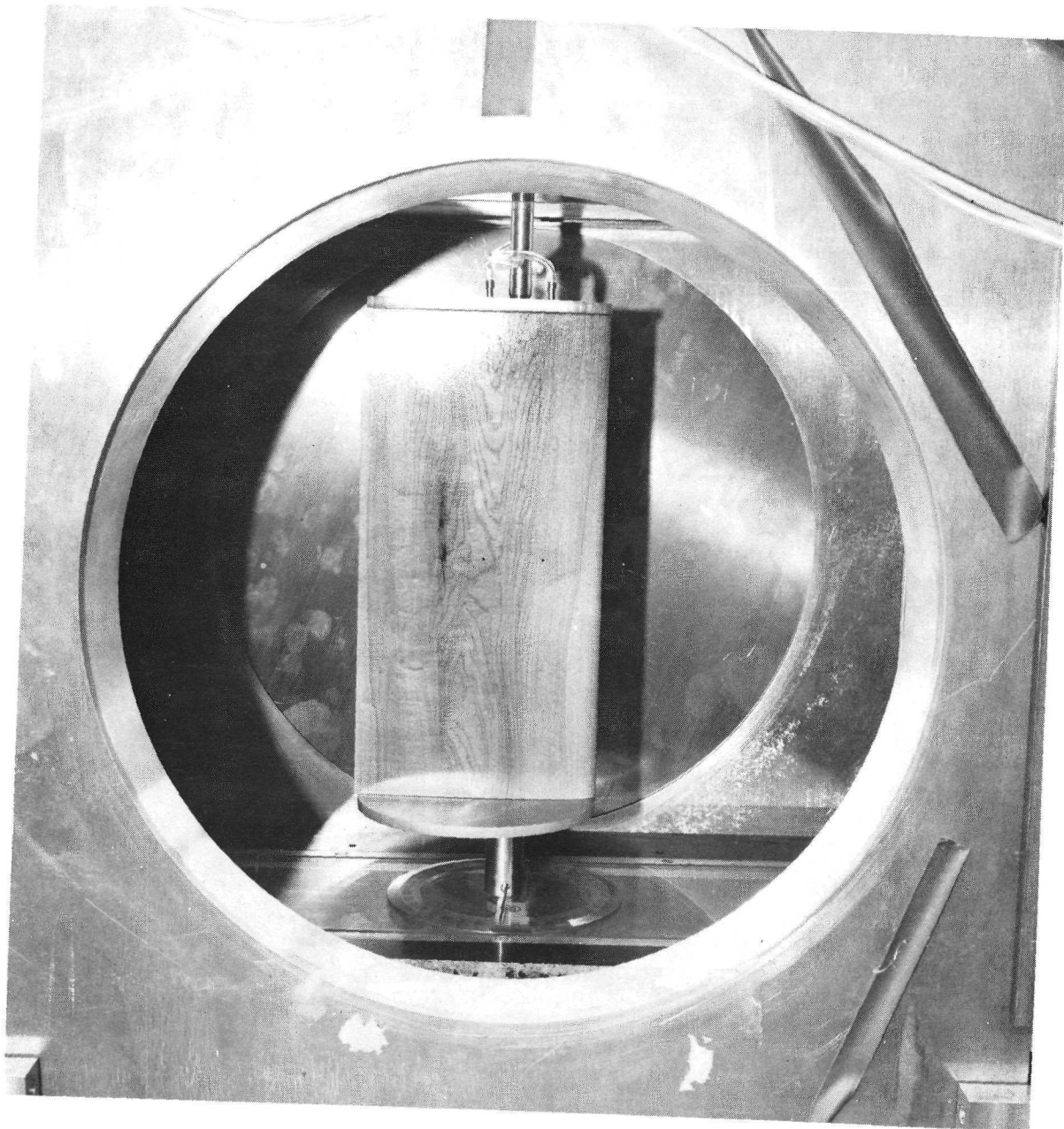


Figure 11. Wing Model in Subsonic Wind Tunnel (NACA 0012)

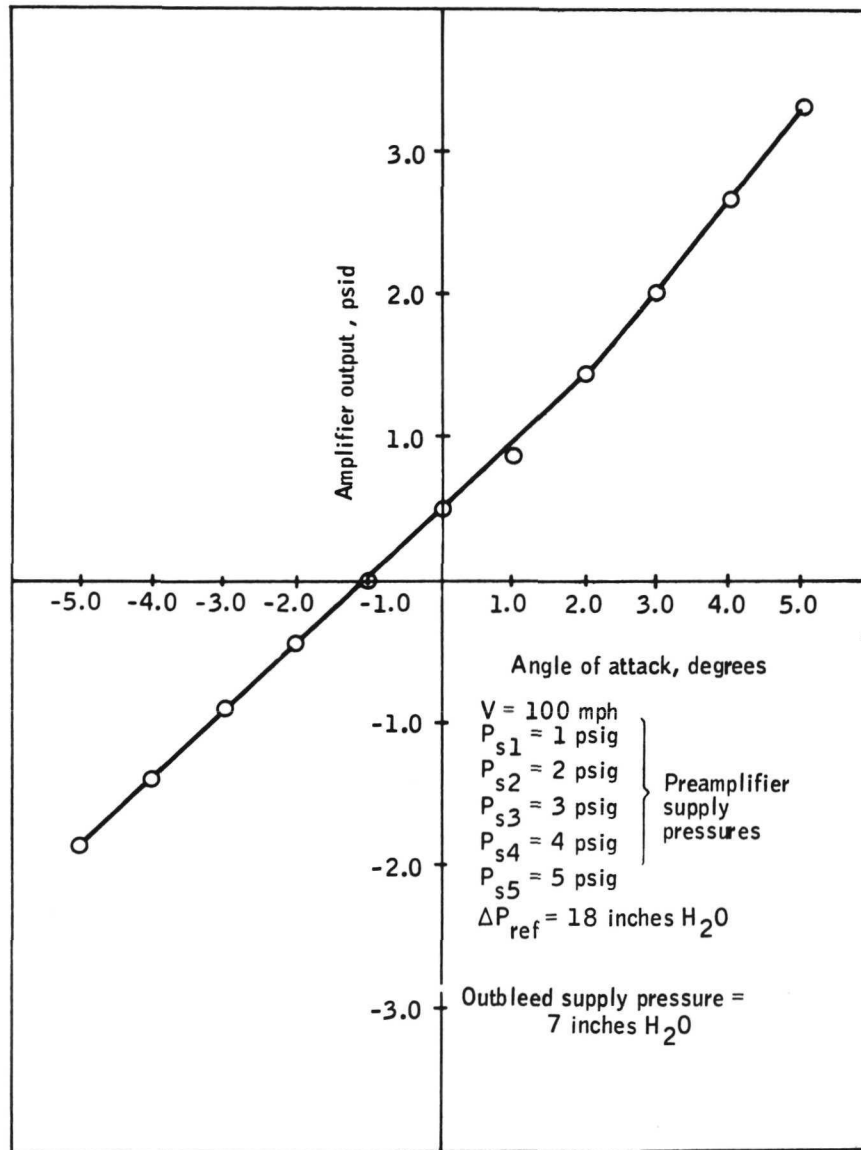


Figure 12. Preamplifier Output versus Angle of Attack for Midchord ΔP on NACA 0012 Airfoil

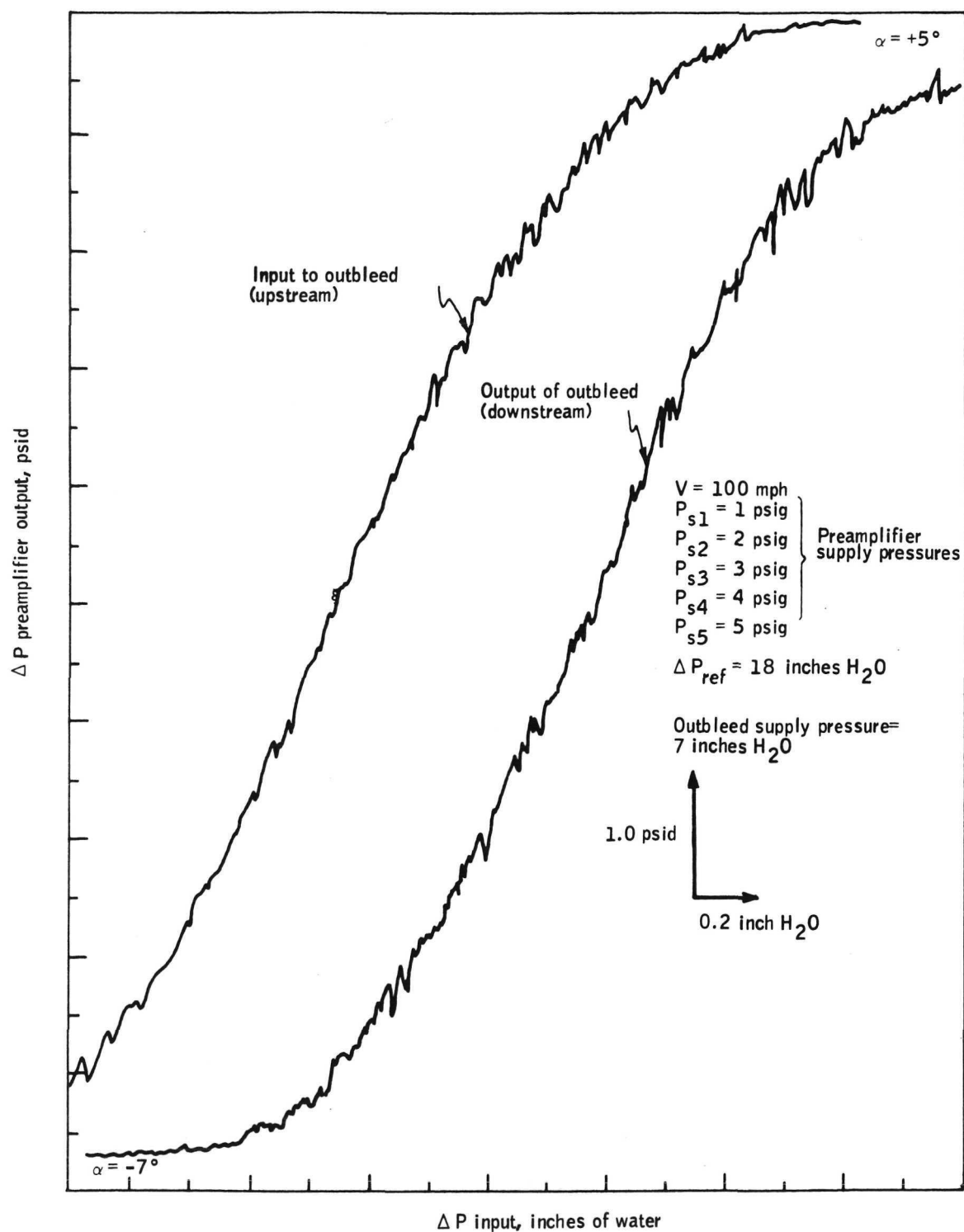


Figure 13. Gain Curves for Outbleed Preamplifier System

closed-loop testing was impossible. These tests provided information about the operational limitations for the VDT jet angle variation and plenum pressures.

By varying the supply pressures to the preamplifier section, gains from 2500 to 4000 could be obtained. A typical gain curve is shown in Figure 14. To effectively change the pressure across the airfoil, air was blown over the airfoil surfaces. Pressure differences were obtained by varying the angle of attack of this airstream. The results indicated that high-frequency pressure pulses did not adversely affect the operation of the system in this static test situation.

It was determined that maximum and minimum plenum pressures were about 45 psig and 15 psig, respectively. The operating characteristics of the proportional amplifier are such that the average of the plenum pressures remains constant at about 30 psig as the jet is deflected through its range.

The fluidic VDT system, as shown in block diagram form in Figure 5, is designed to maintain constant lift on the blade section as angle of attack or airspeed is varied. The open-loop tests of the fluidic system indicated that the system will operate as designed within certain limitations. Pressure recovery within the fluidic amplifiers and saturation levels impose limitations on the maximum jet angle obtainable and on the blowing coefficient (determined by VDT plenum pressure). The performance of the system is, therefore, limited by the maximum obtainable jet angle and the plenum pressures obtainable in the VDT plenums.

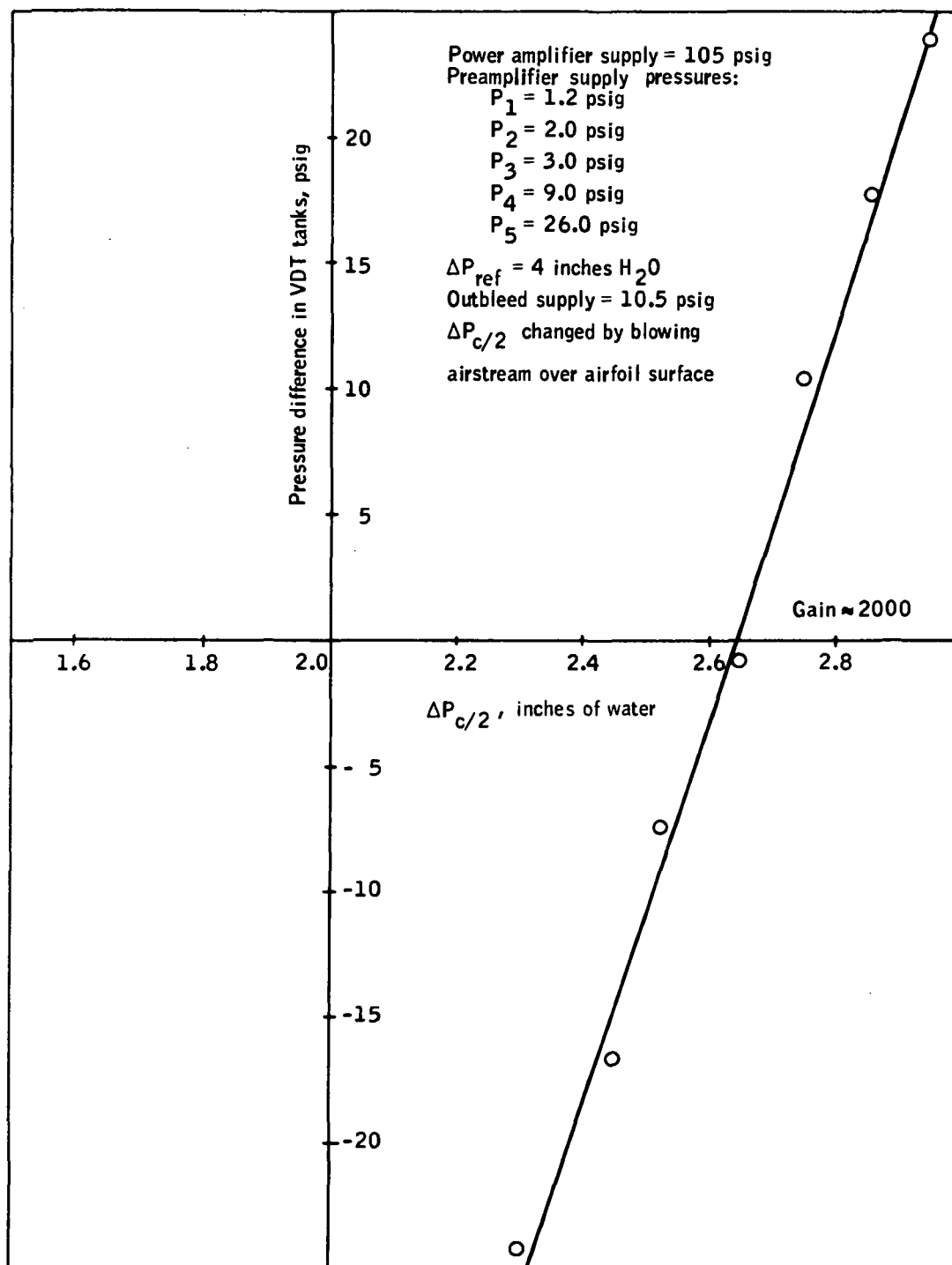


Figure 14. Pressure Gain Curve for Complete VDT Control System

HELICOPTER VDT-BLADE MODEL MODIFICATION AND INSTRUMENTATION

The VDT-blade model and model instrumentation used for the Phase I tests (ref. 2) were used in the current investigations with the exception that a new model center section was designed and fabricated to accommodate the fluidic control system. The model is a two-dimensional, modified NACA 0012 airfoil section having a 7-foot span and approximately a 2-foot chord. The model is made in three equal span sections. Details of the model design and fabrication are given in reference 2.

A series of pressure taps was used to monitor the performance of the fluidic control system. Complete information about the instrumentation for the current model configuration is presented in the operational manual (ref. 6).

For the Phase II tests the model was modified with an improved compliance joint, as shown in Figure 15, to eliminate extraneous model loads on the internal balance system due to air-supply-duct pressurization. The floating cylindrical section extended through the bottom model section (Figure 10) and rested in a base mount fastened to the model baseplate. The possibility of structural binding and the consequent adverse effect on the internal balance system was greatly reduced by the new air-supply-duct arrangement for the model center section. The flexure members of the internal balance system were also stiffened to eliminate adverse effects due to transverse loadings, and additional model internal structural supports were installed to reduce the effect on the balance system of adverse temperature gradient caused by amplifier venting inside the model.

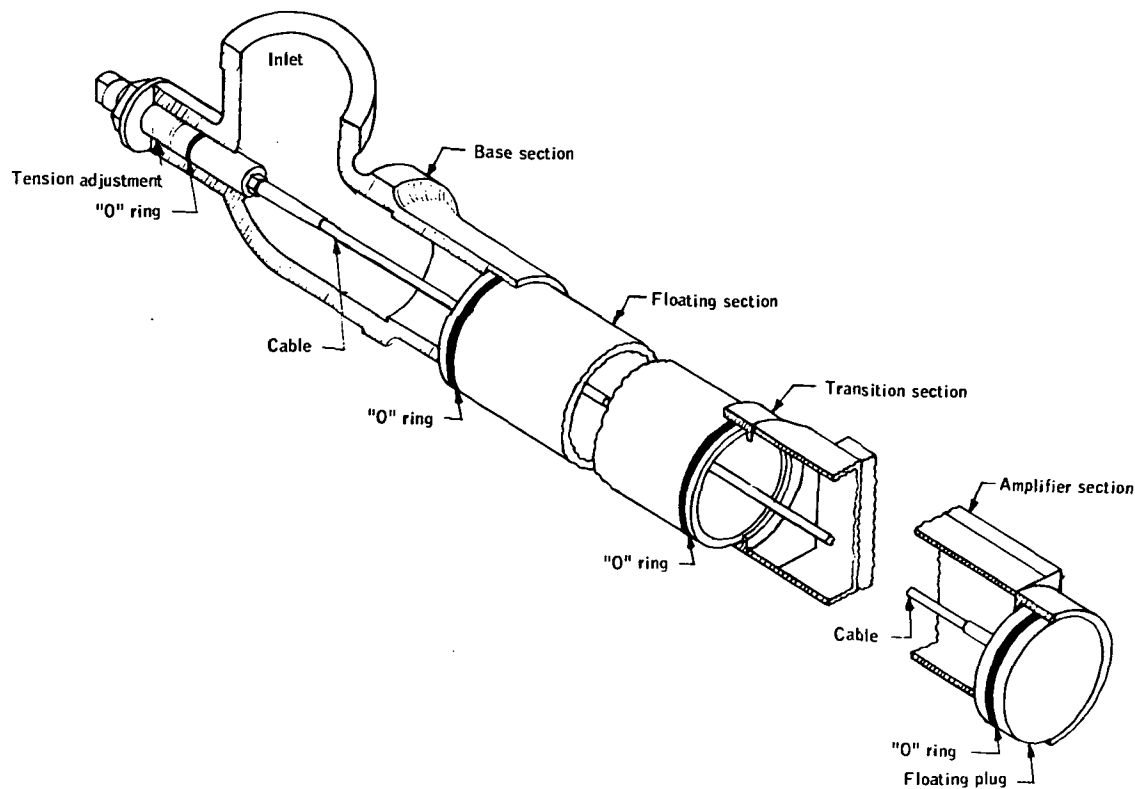


Figure 15. Compliance Joint Assembly

Briefly, the model instrumentation was:

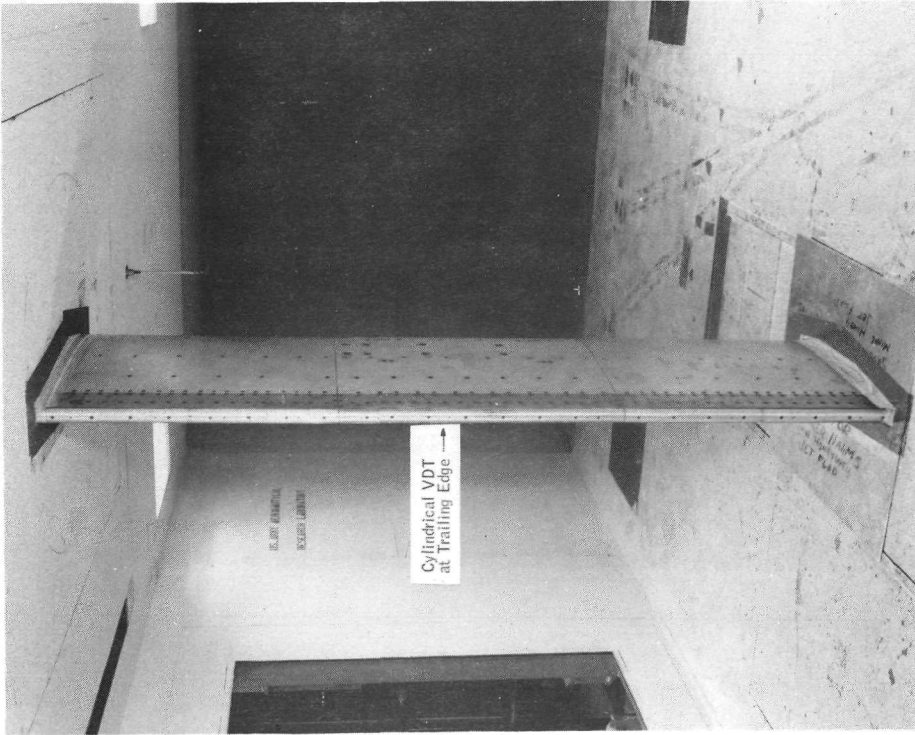
- Model center section --
 - Strain gage balance system for measuring chord force, normal force and moment
 - Two Statham pressure transducers (one each, top and bottom VDT plenum)
 - Four total pressure taps (two each, top and bottom VDT plenum)
 - Forty-two static pressure taps on airfoil surface (mostly chordwise)

- Eighteen static pressure taps on VDT cylinder surface
- Fifteen static pressure taps within fluidic circuitry
- Five thermocouples (one each, top and bottom VDT plenum, two on model surface and one on interior model skin)
- Model end sections --
 - Four total pressure taps for each section (two each, top and bottom VDT plenums)
 - Two thermocouples for each section (one each, top and bottom VDT plenums)

Figure 16 shows the helicopter VDT-blade model installed in AAMRDL's 7 x 10-foot subsonic wind tunnel at NASA-Ames. The gaps between the model sections were covered with Mylar plastic tape to prevent air blowing through from the high- to low-pressure side of the airfoil during testing.



(a) Leading-Edge View



(b) Trailing-Edge View Showing Cylindrical VDT

Figure 16. Helicopter VDT-Blade Mounted in AAMRDL's 7 x 10-foot Wind Tunnel

WIND TUNNEL TEST PROGRAM

Wind tunnel tests were conducted to determine the basic performance of the VDT-blade model for both open- and closed-loop operation. Dynamic tests were also conducted where the VDT jet was oscillated at various frequencies. There are basically three parts to the test data:

- Steady-state tests of the VDT-blade model (open-loop)
- Steady-state tests of the VDT-blade model with lift controller (closed-loop)
- Dynamic tests of the VDT-blade model

The procedures for these tests are described in this section, and test results are presented and discussed in the following section.

Steady-State Tests (Open-Loop)

The open-loop steady-state tests of the helicopter VDT-blade model were made with two different test conditions. The first set of tests was conducted with all three model sections having the same blowing conditions. A second set of tests was conducted with the center section jet blowing at various jet angles with the end sections remaining unblown. Since, for normal helicopter applications, sectional blowing would most likely be used, the tests with only the center section blowing were intended to provide some information as to the effect of sectional blowing on VDT performance. The ranges of parameters for these open-loop steady-state tests were:

- Angle of attack, $0 \leq \alpha \leq 12$ degrees
- Blowing coefficient, $0 \leq \bar{C}_\mu \leq 1.60$
- VDT jet angle, $-30 \leq \theta_j \leq 30$ degrees

- Free-stream dynamic pressure, $10 \leq q \leq 100$ psf
- Maximum VDT tank pressure, ≈ 45 psig

Steady -State Tests with Lift Controller (Closed-Loop)

The performance of the fluidic VDT lift control system was investigated with the control circuitry contained in the model center section. The two end sections remained unblown while the VDT jet angle of the center section was automatically varied by the fluidic control. The jet thrust was constant during these wind tunnel tests. The goal of the lift-control system was to maintain a constant lift value while the airfoil experienced a number of changes in either angle of attack or wind tunnel velocity. Lift data was taken with the controller operating throughout the following range of parameters:

- Angle of attack, $0 \leq \alpha \leq 12$ degrees
- VDT jet angle, $-30 \leq \theta_j \leq 30$ degrees
- Blowing coefficient, $0 \leq \bar{C}_\mu \leq 1.20$
- Free-stream dynamic pressure, $10 \leq q \leq 100$ psf
- Maximum VDT tank pressure, ≈ 45 psig

Dynamic Tests

Dynamic tests were conducted using the VDT-blade model with the center-section jet oscillating at various frequencies. The tests were intended to indicate the dynamic response and dynamic lift characteristics of the VDT-blade model. Jet thrust was held constant throughout the test runs. The fluidic circuitry was used to oscillate the jet by inputting a signal from a fluidic function generator. However, inconsistencies were noted in the data.

Additional tests were conducted using the model center section only with a single endplate to obtain finite-aspect-ratio data. These tests provided more reliable data than the tests using the complete VDT-blade model. The dynamic valve used for the Phase I (ref. 2) tests was used to oscillate the VDT jet angle and the LTV, VSB-8 balance system was used. The ranges of parameters for these dynamic tests were:

- Angle of attack, $\alpha = 0$ and 12 degrees
- Blowing coefficient, $0.26 \leq \bar{C}_\mu \leq 0.946$
- Average jet angle, $\theta_{jm} = 0$
- Free-stream dynamic pressure, $11 \leq q \leq 40$ psf
- Maximum VDT tank pressures, ≈ 35 psig
- VDT jet angle amplitude, $\Delta\theta_j = \pm 85$ degrees
- Jet oscillation frequency, $5 \leq f \leq 45$ Hz

Data Reduction Method

The force measurements obtained from the balance systems were computer-reduced to obtain the aerodynamic coefficients. Because of a large number of malfunctioning pressure taps, very few good pressure distributions could be obtained, and the pressure data was mainly used as a rough check on the balance measurements. For the closed-loop and dynamic tests, the internal balance system was used to measure the normal forces.

Since the amplifiers were vented inside the model, the flow of cold air produced a temperature gradient that adversely affected the internal balance system. Therefore, the air was heated, the temperature of the air to the VDT tanks was modulated during tests runs, and the internal balance system was calibrated for temperature change. Temperature tare corrections were negligible for normal force measurements but were significant for chord force and moment measurements.

The VDT jet angle, θ_j , was determined from the VDT tank pressure differential in accordance with oil-trace calibrations made during Phase I tests (ref. 2). The calibration curve is presented in Figure 17. The blowing coefficient, \bar{C}_μ , was calculated from the VDT tank pressures and corrected by the discharge coefficient (0.94) in accordance with reference 2.

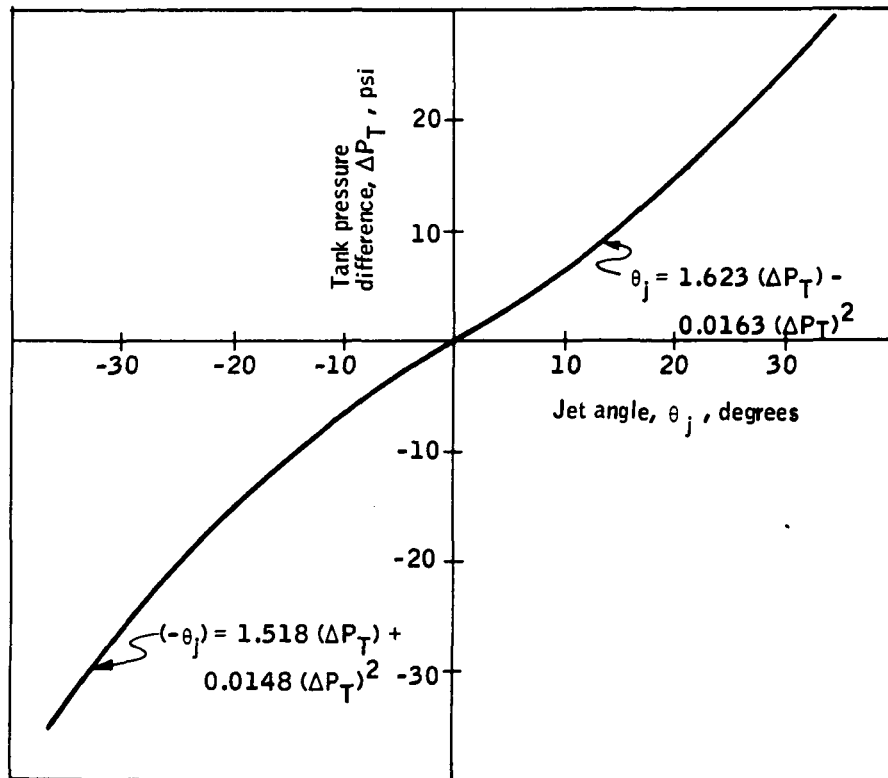


Figure 17. VDT Jet Angle as a Function of VDT Tank Pressure Difference

VDT-BLADE MODEL TEST RESULTS

Steady-State Tests (Open-Loop)

Nonblowing characteristics. - The results for the nonblowing case of the helicopter VDT-blade are presented in Figures 18 through 21. The lift coefficient data in Figure 18 is compared with two-dimensional Joukowski theory (ref. 7). As formerly noted in reference 2, truncating the NACA 0012 airfoil section at the 80% chord to install the VDT-cylinder appears to slightly change the lift characteristics. The helicopter VDT-blade model has a thickness ratio (maximum thickness to chord) of approximately 0.147, and this can account for the lift-curve slope of the model slightly exceeding that of the theory. The internal balance system (IBS) consistently gave lift results slightly higher than the wind tunnel balance as shown in Figure 18. Therefore, in subsequent tests where it was necessary to rely on the IBS lift measurements, a correction factor was determined based on the difference noted between IBS and wind tunnel balance measurements for the same test configurations.

The drag coefficient results in Figure 19 are compared to data for a NACA 0012 wing section taken from references 8 and 9. The drag of the VDT-blade model is higher than that of the standard smooth NACA 0012 airfoil. This can be attributed to the truncation of the airfoil trailing edge for the VDT cylinder.

The leading-edge and quarter-chord moment coefficients for the VDT-blade model are presented in Figures 20 and 21. The leading-edge moment coefficient becomes more negative with increase of angle of attack, as expected. However, the quarter-chord moment coefficient is indicated to increase with angle of attack when it should remain essentially constant for a symmetrical airfoil. For the results shown in Figures 20 and 21, the VDT-blade's aerodynamic center is indicated to be at approximately 0.17 c. However, in reference 2 the pressure integration data for the VDT-blade model

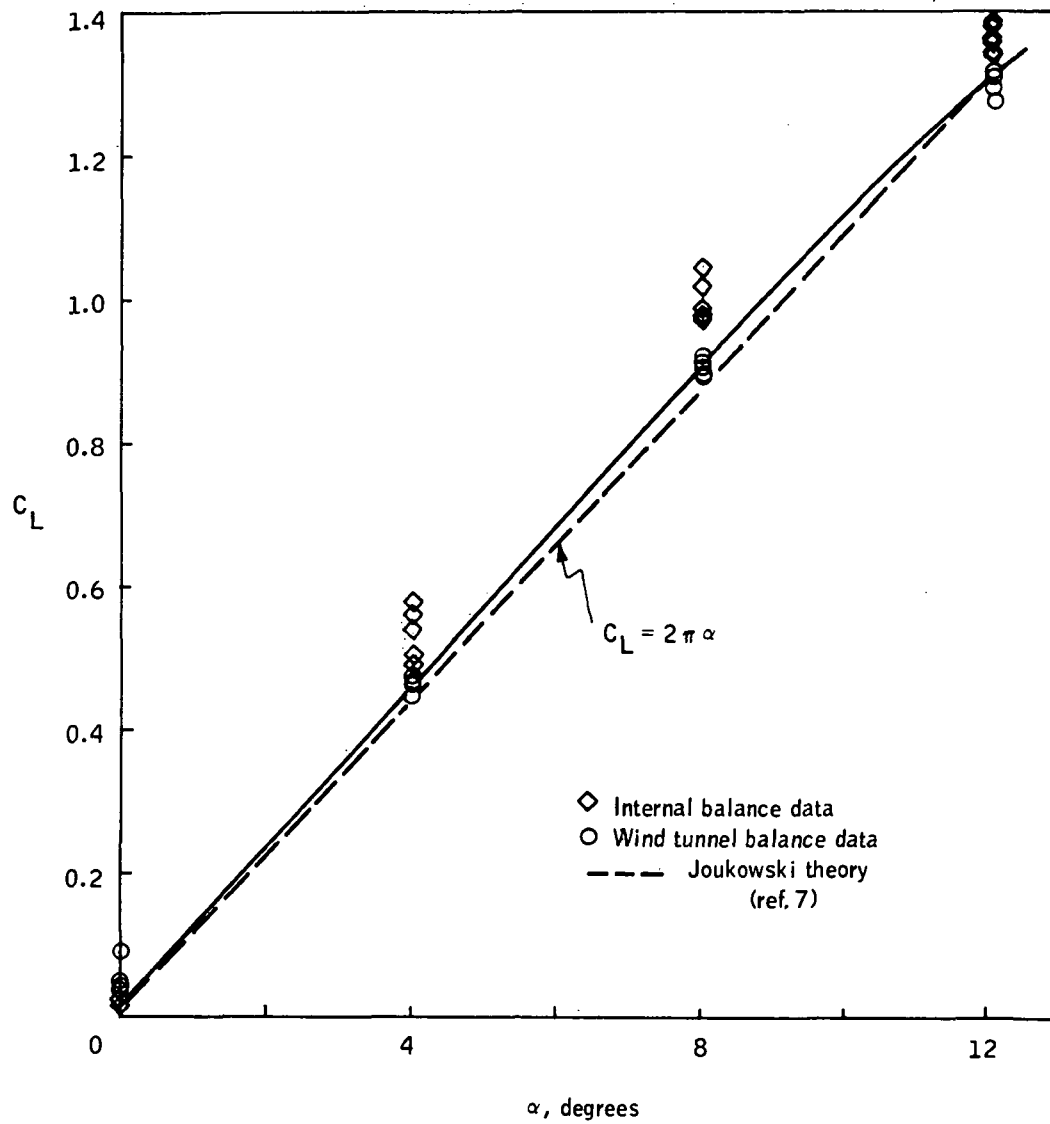


Figure 18. VDT-Blade Lift Coefficient as a Function of Angle of Attack - Full Span, No Blowing

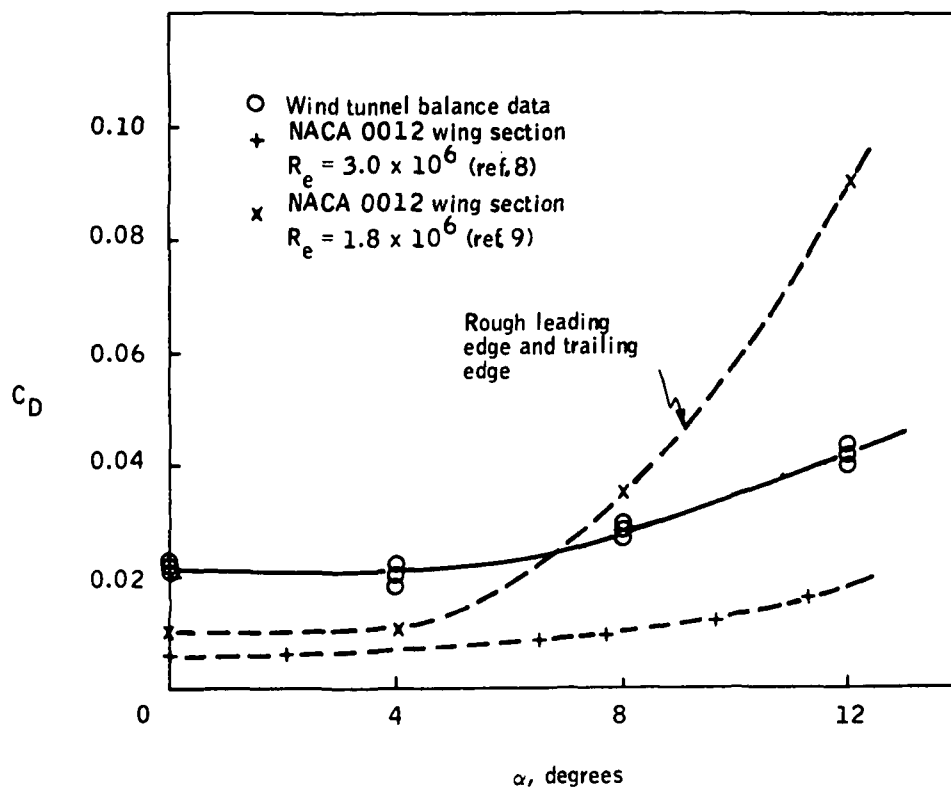


Figure 19. VDT-Blade Drag Coefficient as a Function of Angle of Attack - Full Span, No Blowing

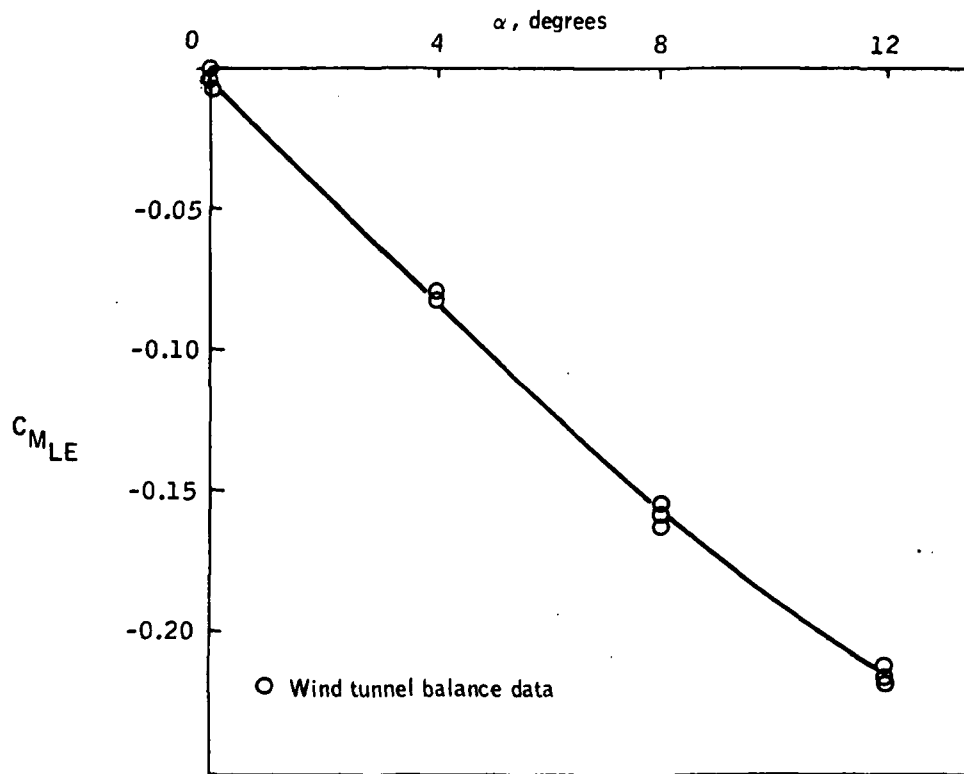


Figure 20. VDT-Blade Leading-Edge Moment Coefficient as a Function of Angle of Attack - Full Span, No Blowing

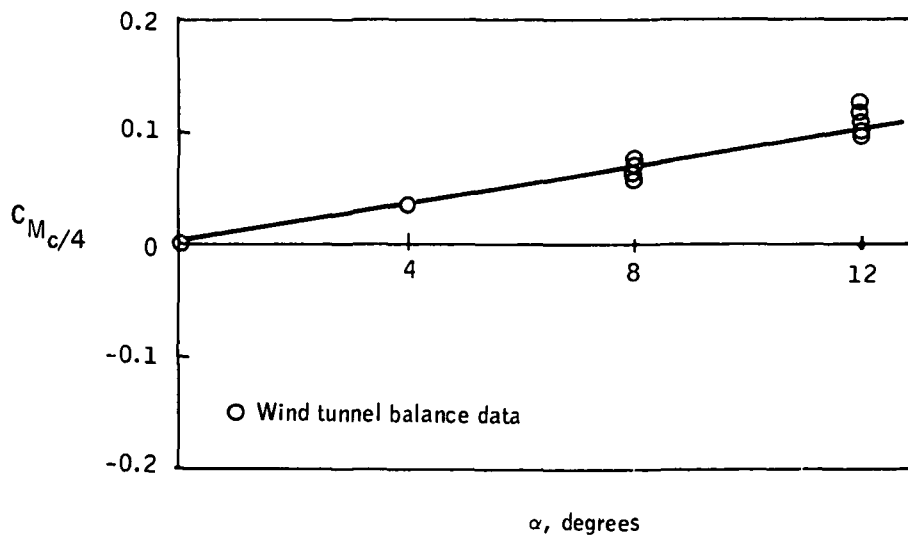


Figure 21. VDT-Blade Quarter-Chord Moment Coefficient as a Function of Angle of Attack - Full Span, No Blowing

showed the aerodynamic center to be at approximately 0.25 c, which is the approximate location for standard airfoils. Therefore, all moment coefficients in this report will indicate higher positive values than the model actually encountered.

Full-span blowing. - The data for the VDT-blade model blowing full span has been plotted for angles of attack of 0, 4, 8, and 12 degrees with jet angles of 0, 10, 20, 30, and -30 degrees. Since some full-span blowing and a similar configuration, center-section blowing with endplates, was done previously in the Phase I wind tunnel tests (ref. 2), many of the results are similar, and a detailed discussion is not presented in this report.

Lift coefficient results for full-span blowing at all angles of attack are shown in Figures 22 through 25. The increase of C_L with increasing \bar{C}_μ for $\theta_j = 0, 10, \text{ and } 20$ degrees compare well with those observed in reference 2 and those predicted by Spence's theory (ref. 5). The agreement between theory and experiment deviates for $\theta_j \geq 30$ degrees.

The drag characteristics with VDT jet blowing are presented for $\alpha = 0$ to 12 degrees in Figures 26 through 29. The drag reduction is shown to remain essentially constant for different jet angles at $\alpha \leq 4$ degrees. At higher angles of attack, however, the drag reduction decreases as the jet angle increases. This characteristic of drag reduction was also found in reference 2 but was more apparent due to the aspect ratio effects of the endplates.

To more fully evaluate drag reduction, it is necessary to determine the recovered thrust. The recovered thrust is defined to be the difference between the measured drag on the blown airfoil and the predicted drag on a similar unblown airfoil which produces the same circulation lift. A complete discussion on the thrust recovery for the VDT jet-flapped airfoil is presented in reference 2. The measured drag coefficient is composed of the zero-lift drag coefficient, C_{D0} , the drag coefficient due to lift, C_{DL} , and the actual thrust due to blowing. In equation form

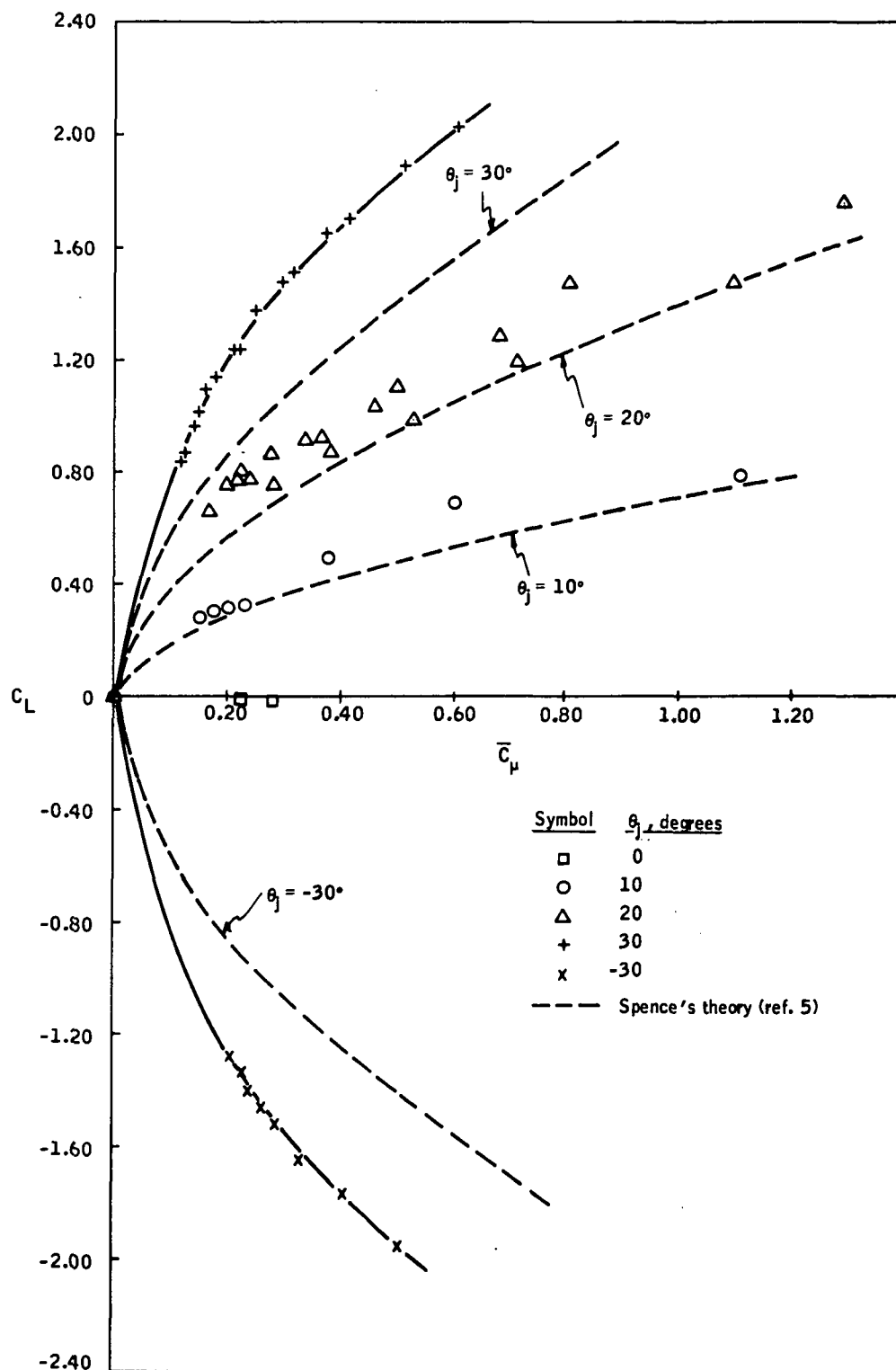


Figure 22. Lift Coefficient as a Function of Blowing Coefficient - Full-Span Blowing, $\alpha = 0$

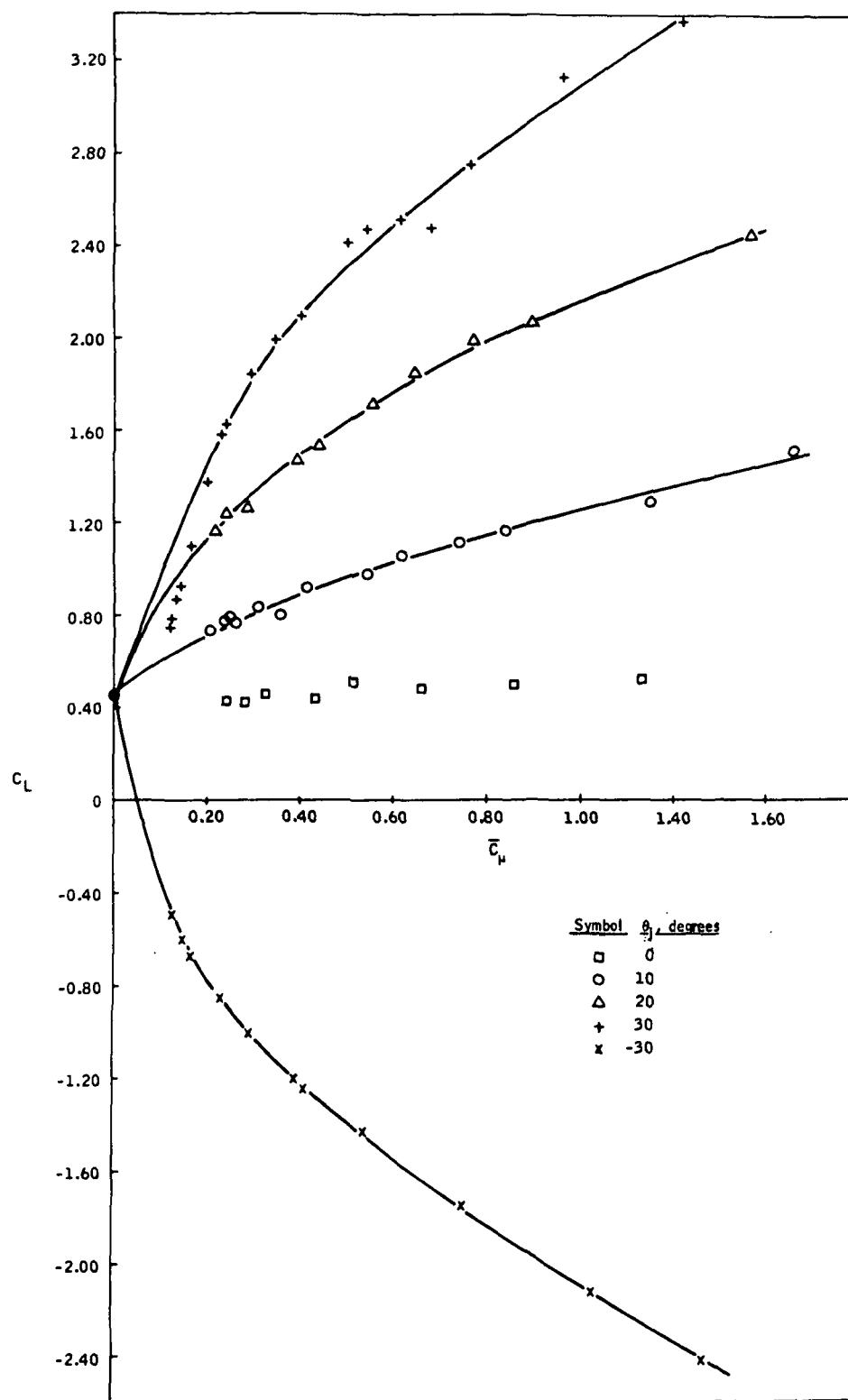


Figure 23. Lift Coefficient as a Function of Blowing Coefficient - Full-Span Blowing, $\alpha = 4$ degrees

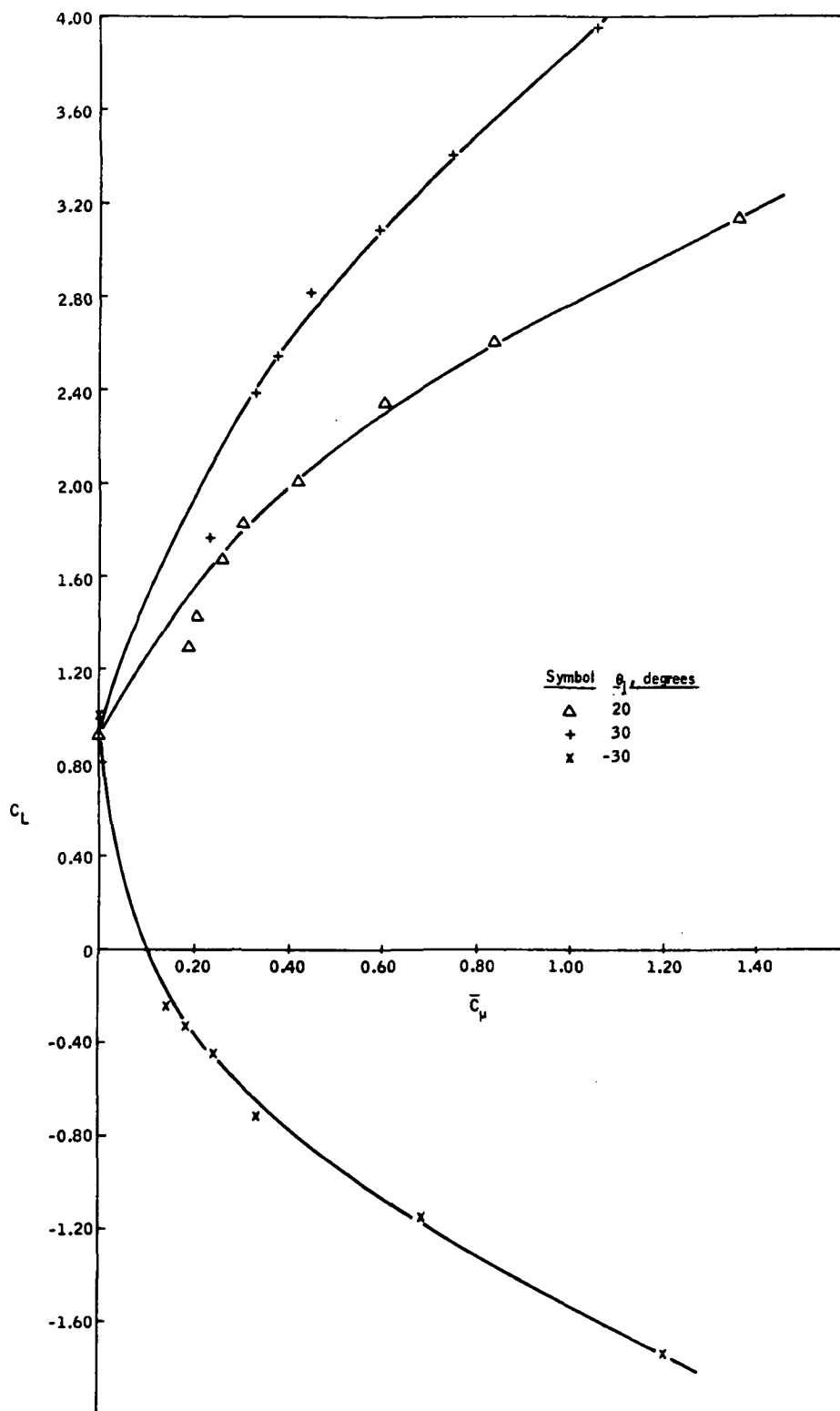


Figure 24. Lift Coefficient as a Function of Blowing Coefficient - Full-Span Blowing, $\alpha = 8$ degrees

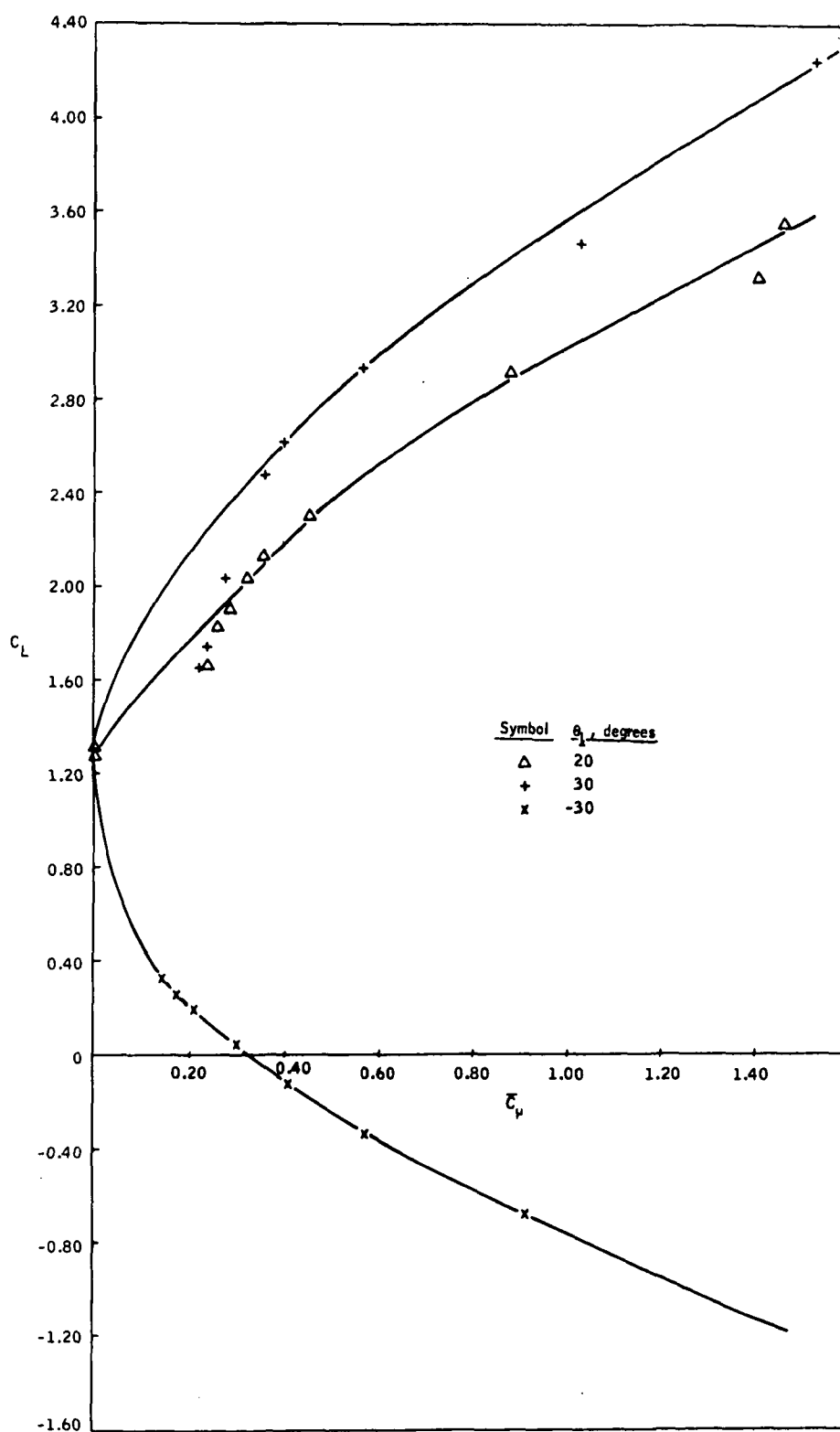
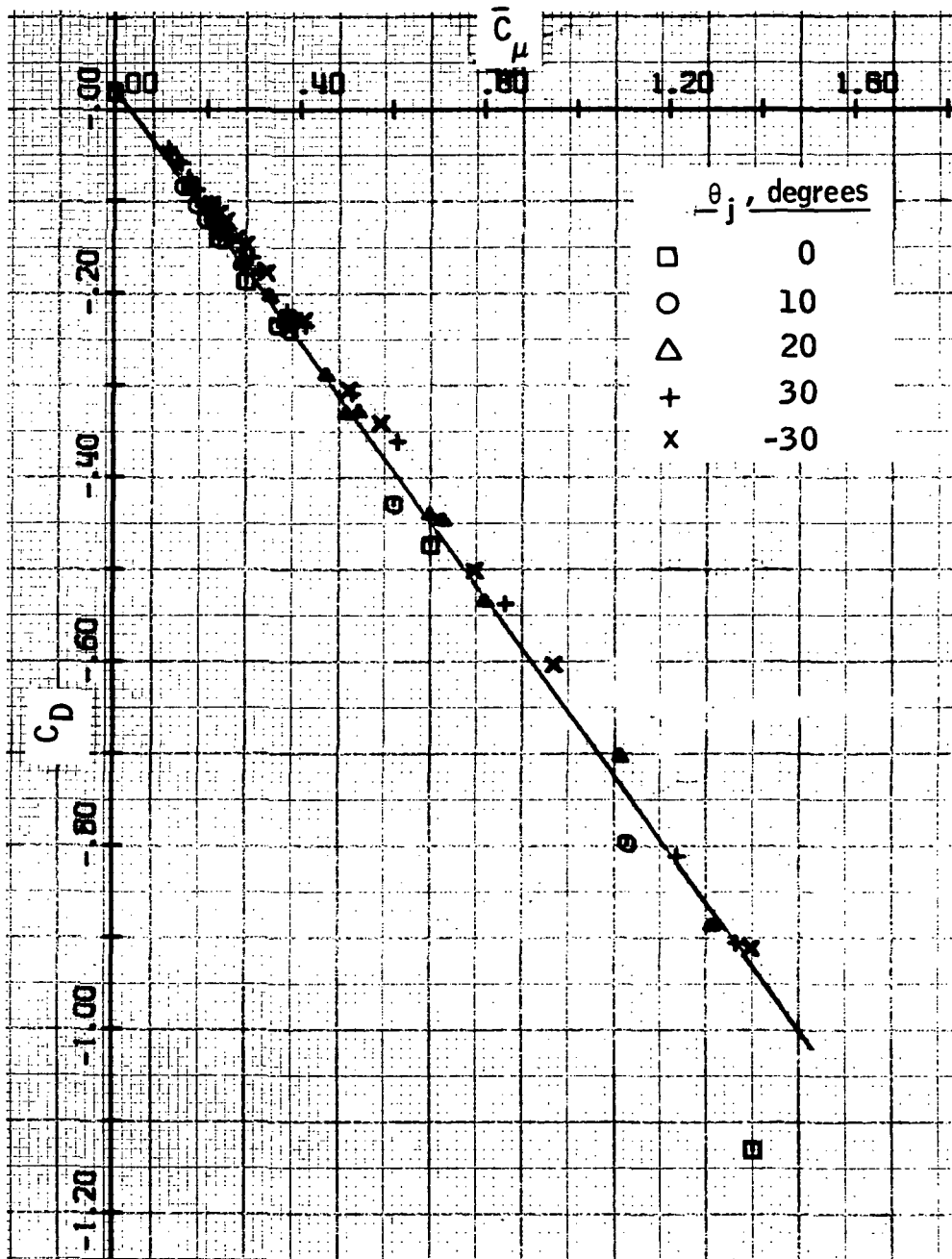


Figure 25. Lift Coefficient as a Function of Blowing Coefficient - Full-Span Blowing, $\alpha = 12$ degrees



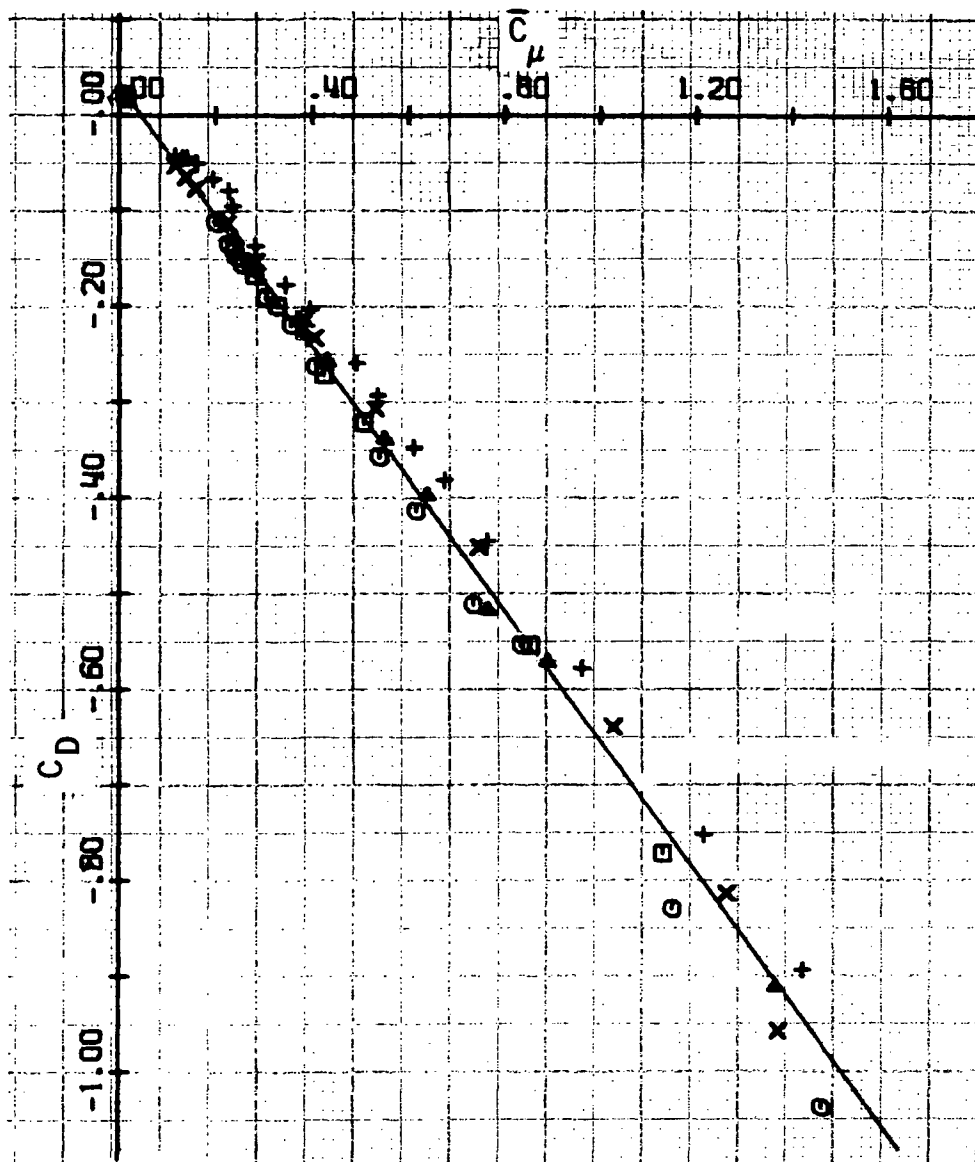


Figure 27. Drag Coefficient as a Function of Blowing Coefficient - Full-Span Blowing, $\alpha = 4$ degrees

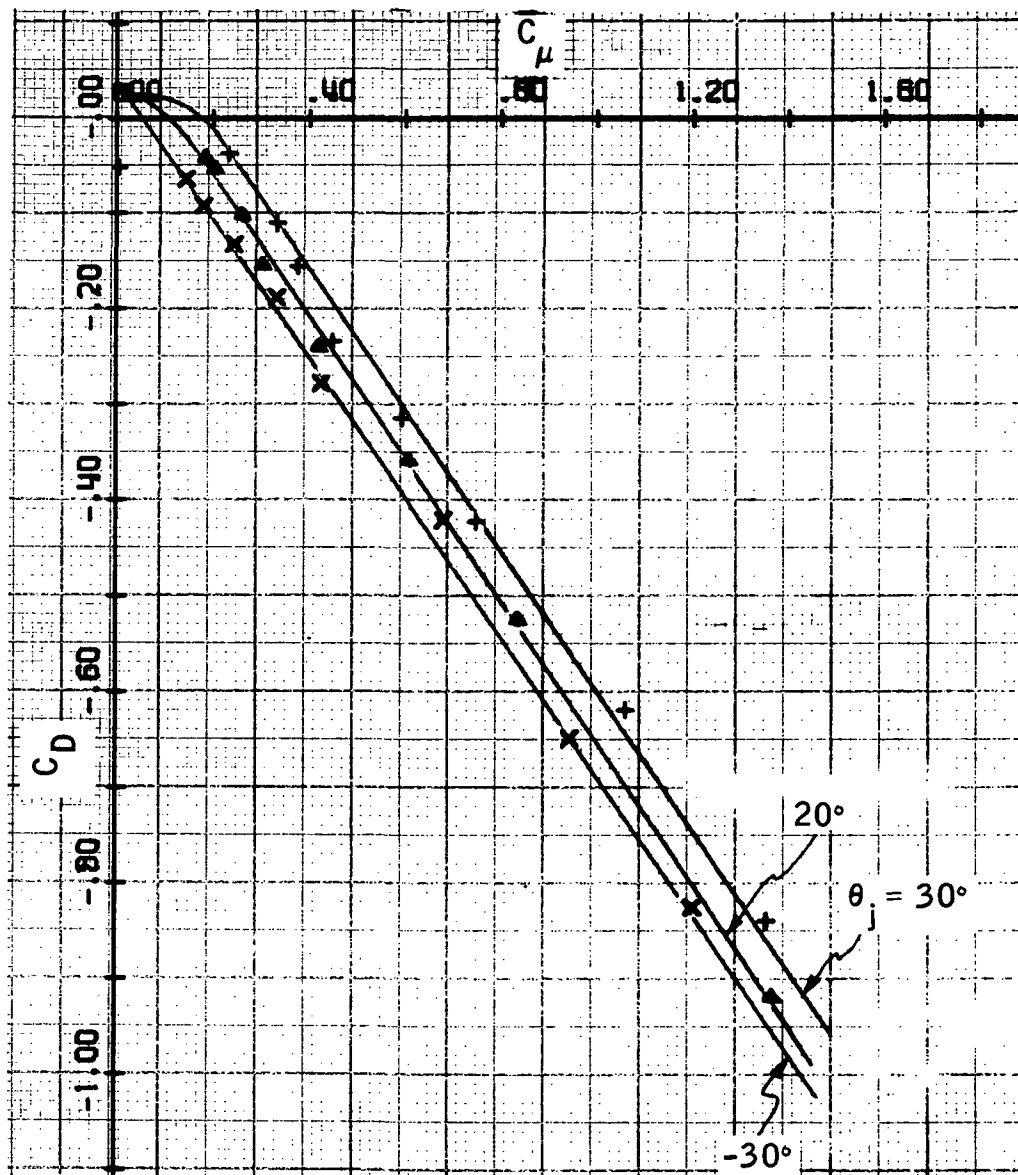


Figure 28. Drag Coefficient as a Function of Blowing Coefficient - Full-Span Blowing, $\alpha = 8$ degrees

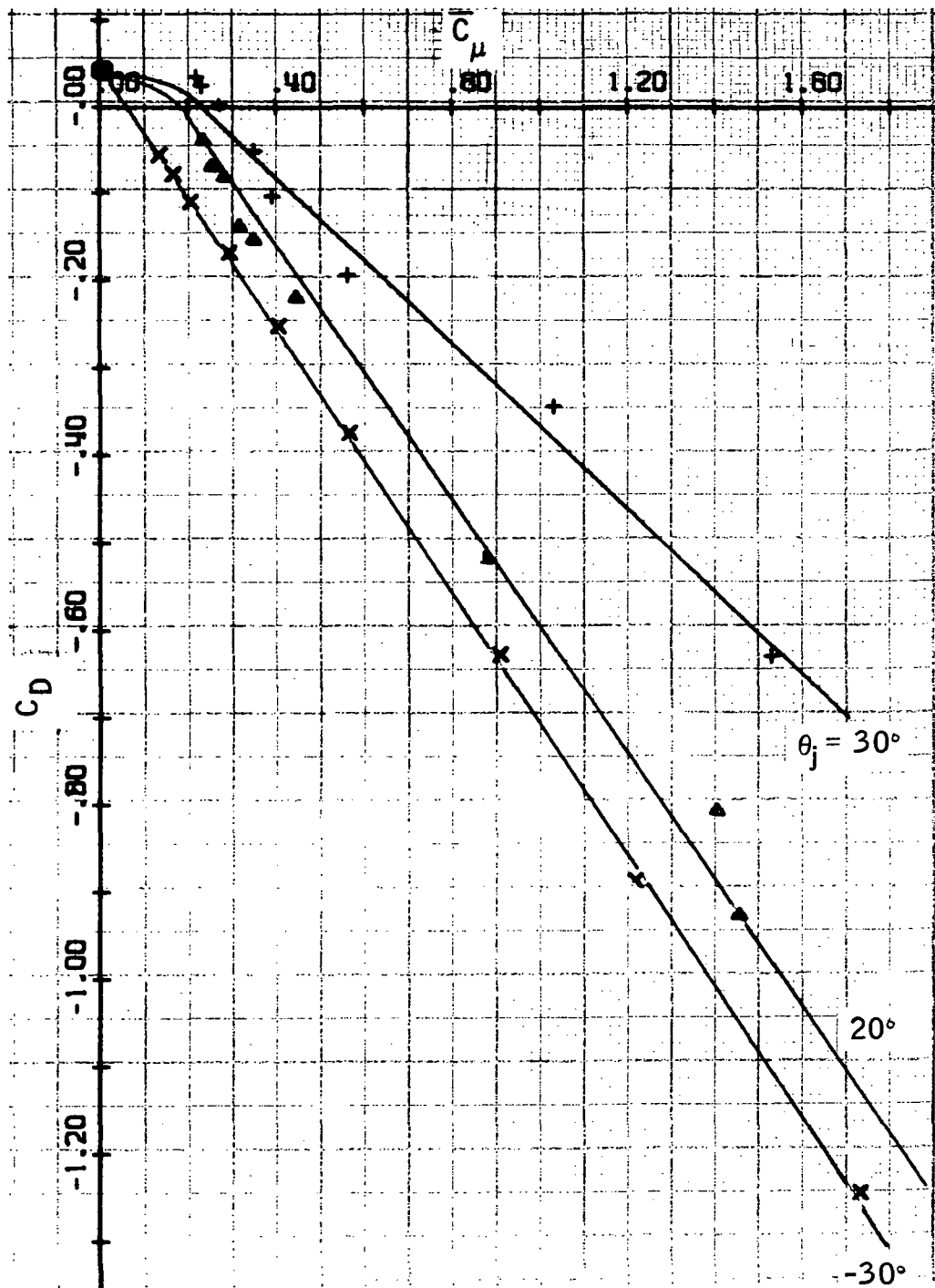


Figure 29. Drag Coefficient as a Function of Blowing Coefficient - Full-Span Blowing, $\alpha = 12$ degrees

$$C_D = C_{D0} + C_{DL} - \lambda \bar{C}_\mu \quad (6)$$

where the percentage of the isentropic thrust which is recovered is indicated by λ . A linearized drag polar, C_L^2 versus C_D , for the unblown wing has been plotted in Figure 30 to determine C_{D0} and C_{DL} . The total drag coefficient for the hypothetical wing can be represented by the following equation:

$$C_{Dh} = 0.02 + 0.0125 C_L^2 \quad (7)$$

The coefficient for C_L^2 , 0.0125, is much smaller than the 0.07 value found in reference 2 for the center-section blowing with endplates. This result again demonstrates the aspect-ratio effect of the endplates on the previous results. As the effective aspect ratio approaches infinity, the coefficient of the C_L^2 term becomes smaller.

The drag reduction due to blowing can then be represented by

$$\Delta C_D = C_D - C_{Dh} = -\lambda \bar{C}_\mu \quad (8)$$

and

$$\lambda = \frac{\Delta C_D}{\bar{C}_\mu} \quad (9)$$

Thus, λ may be determined from plots of ΔC_D versus \bar{C}_μ . These are shown in Figures 31 through 34 for all angles of attack. The average slope of the curves is 0.74 ($\lambda \approx 0.74$), indicating 74% of the isentropic thrust is recovered. Since the ratio of actual static thrust to isentropic thrust is roughly 0.74 for the VDT-blade (ref. 2), the results indicate that 100% of the available thrust is recovered, which is essentially the same result obtained in reference 2 for tests of the model center section only with endplates.

The quarter-chord moment coefficients for all angles of attack are presented in Figures 35 through 38 for $\theta_j > 0$ degree and in Figure 39 for $\theta_j = -30$ degrees. The trends of the results shown are basically consistent with

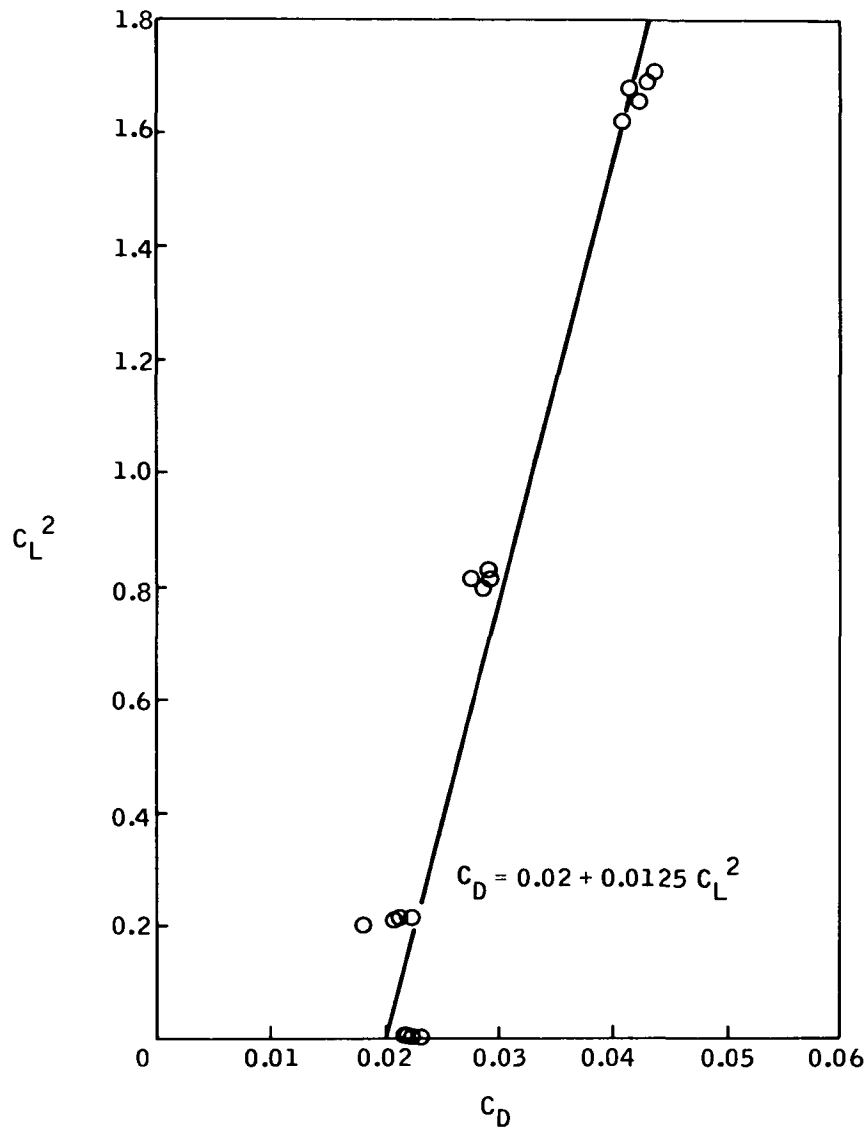


Figure 30. Linearized Drag Polar for Unblown VDT-Blade

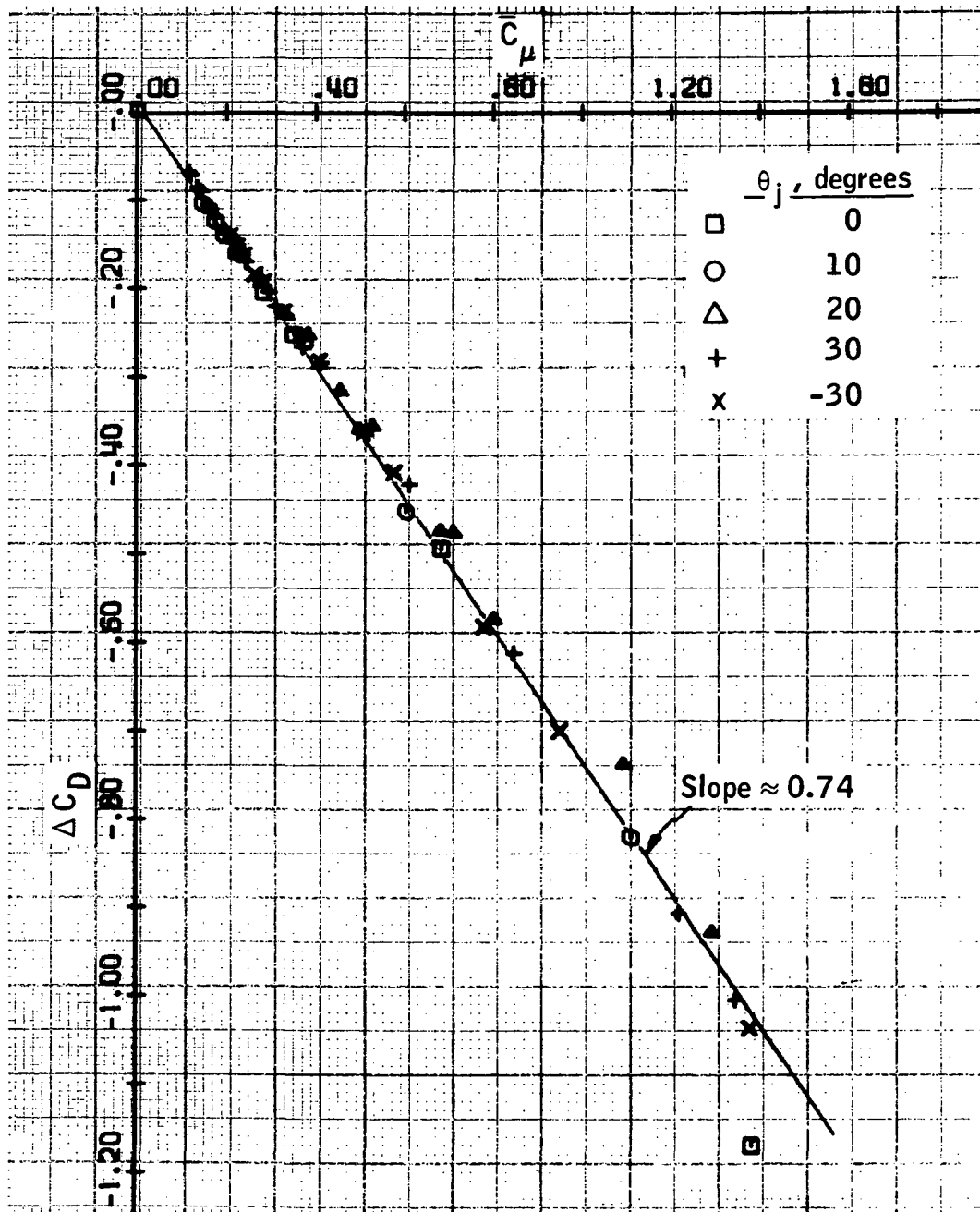


Figure 31. Drag Reduction Due to Blowing - Full-Span Blowing, $\alpha = 0$

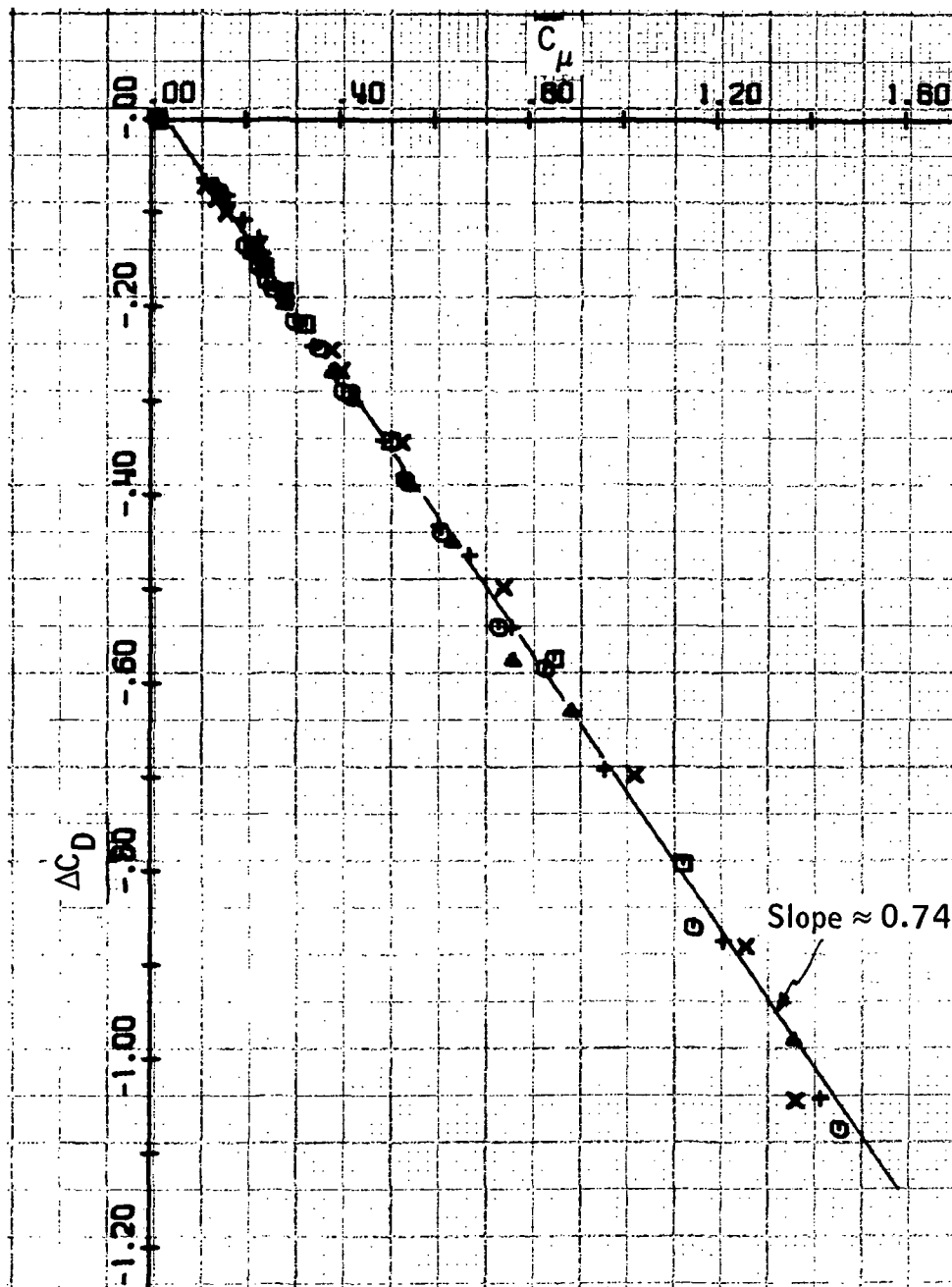


Figure 32. Drag Reduction Due to Blowing - Full-Span Blowing, $\alpha = 4$ degrees

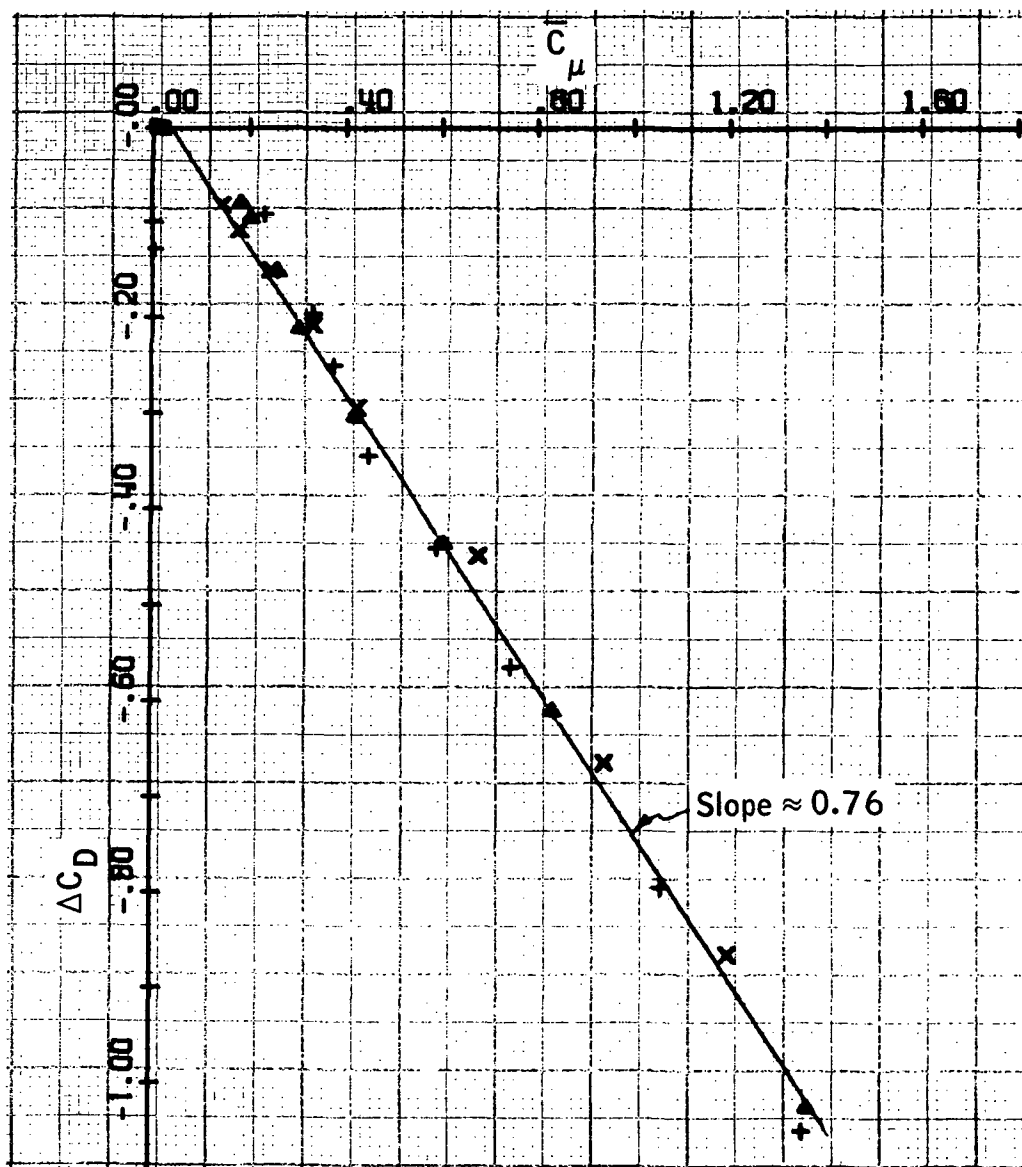


Figure 33. Drag Reduction Due to Blowing - Full-Span Blowing, $\alpha = 8$ degrees

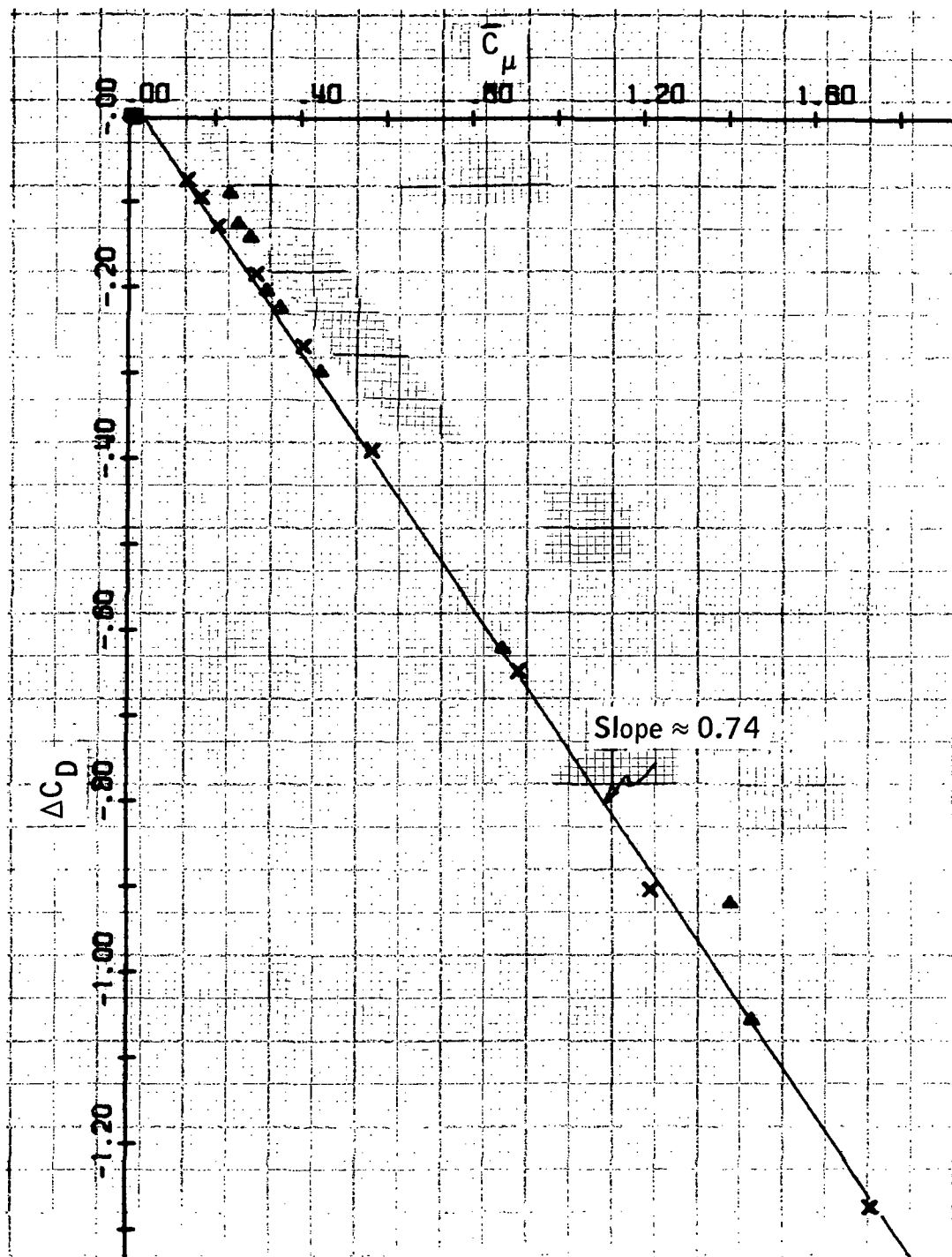


Figure 34. Drag Reduction Due to Blowing - Full-Span Blowing, $\alpha = 12$ degrees

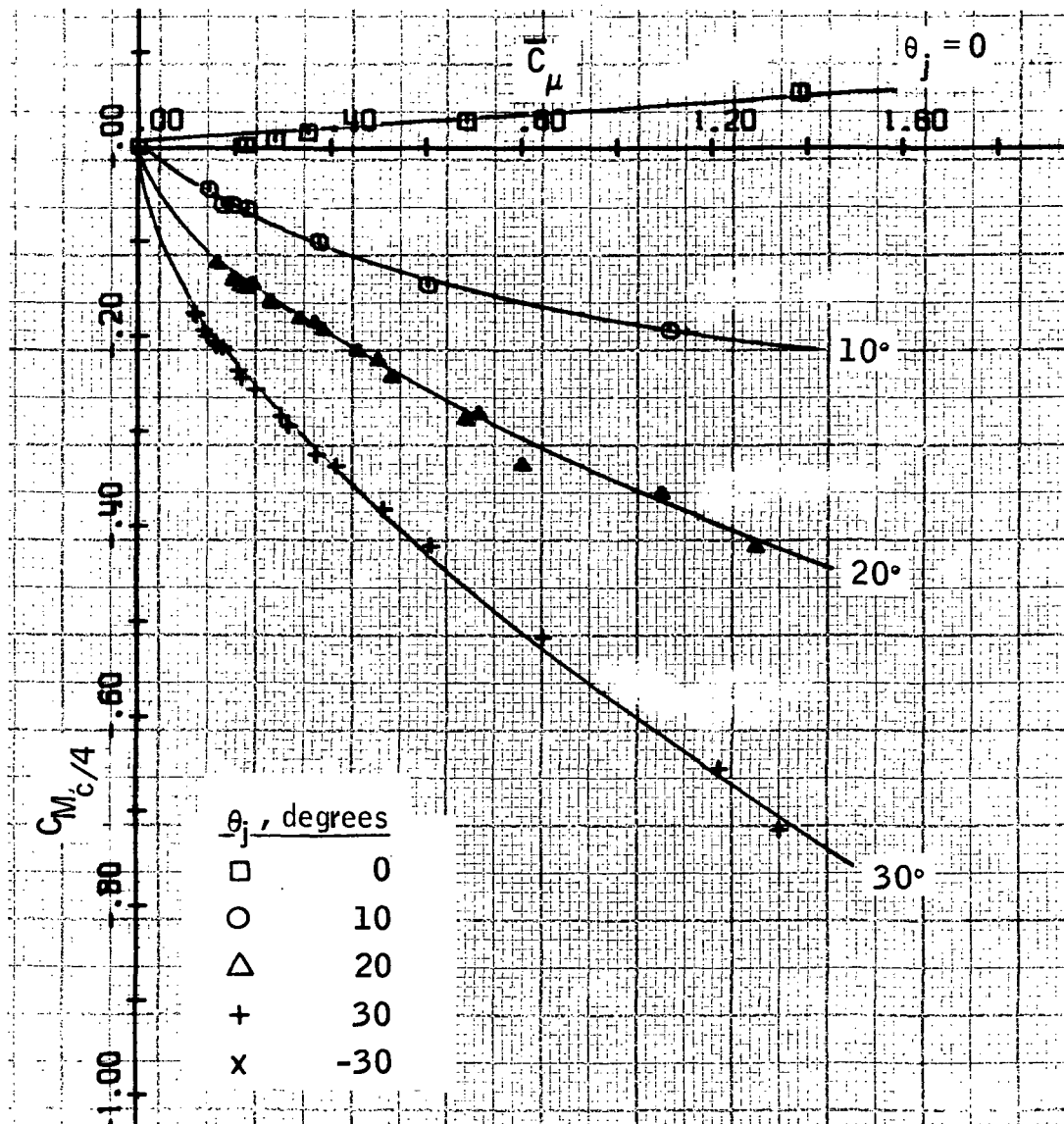


Figure 35. Quarter-Chord Moment Variation with Blowing Coefficient - Full-Span Blowing, $\alpha = 0$

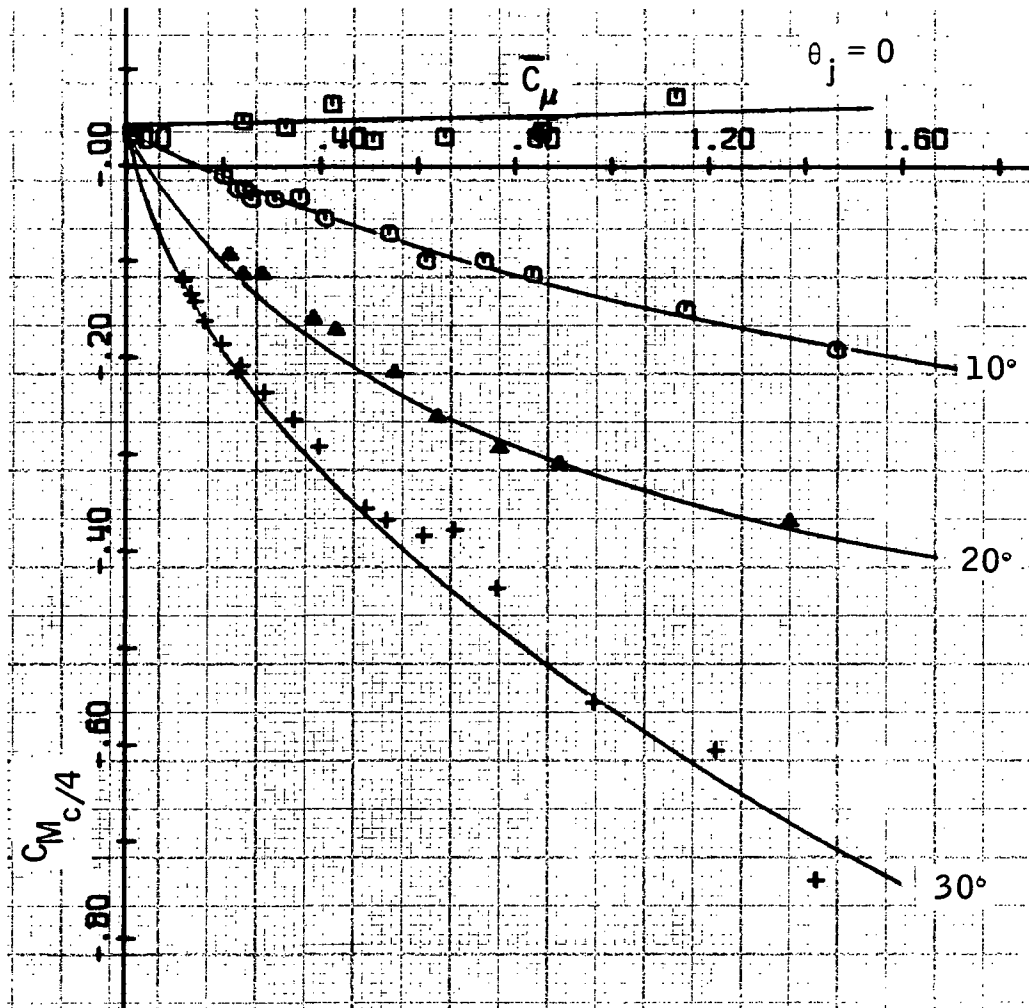


Figure 36. Quarter-Chord Moment Variation with Blowing Coefficient - Full-Span Blowing, $\alpha = 4$ degrees

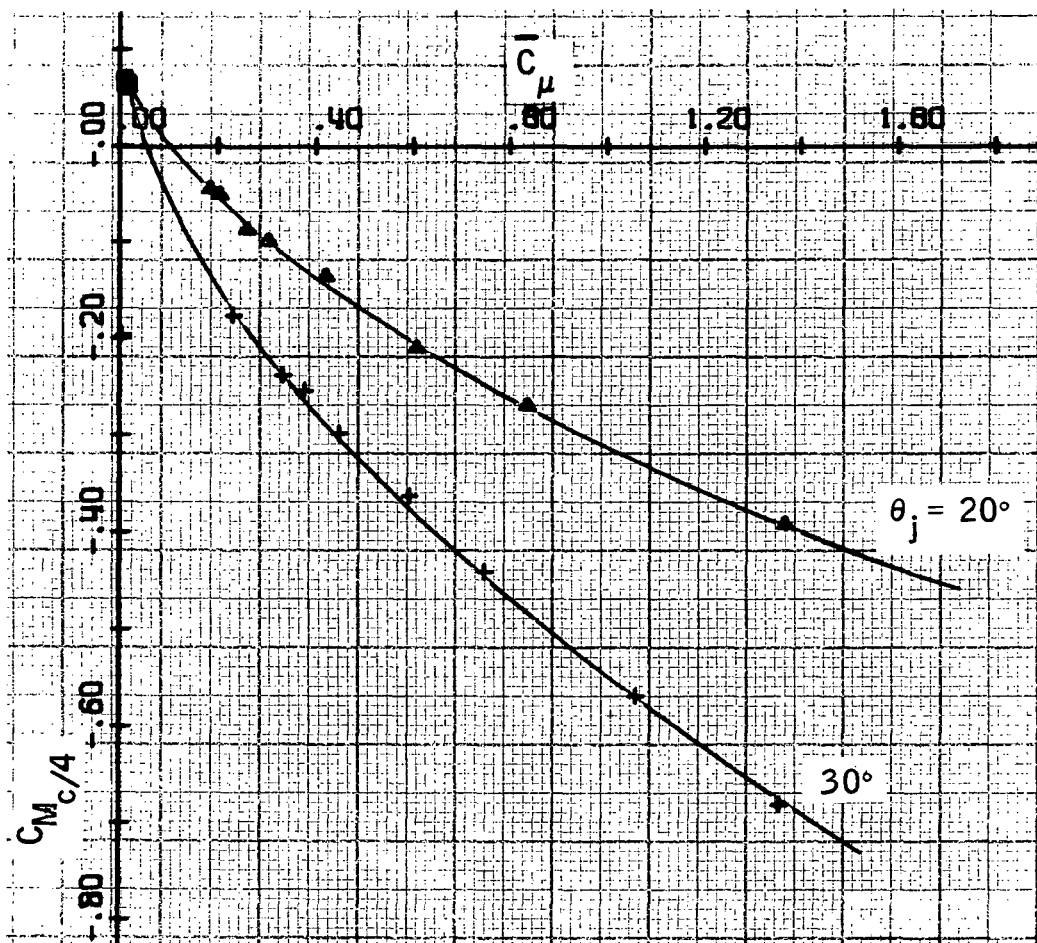


Figure 37. Quarter-Chord Moment Variation with Blowing Coefficient - Full-Span Blowing, $\alpha \approx 8$ degrees

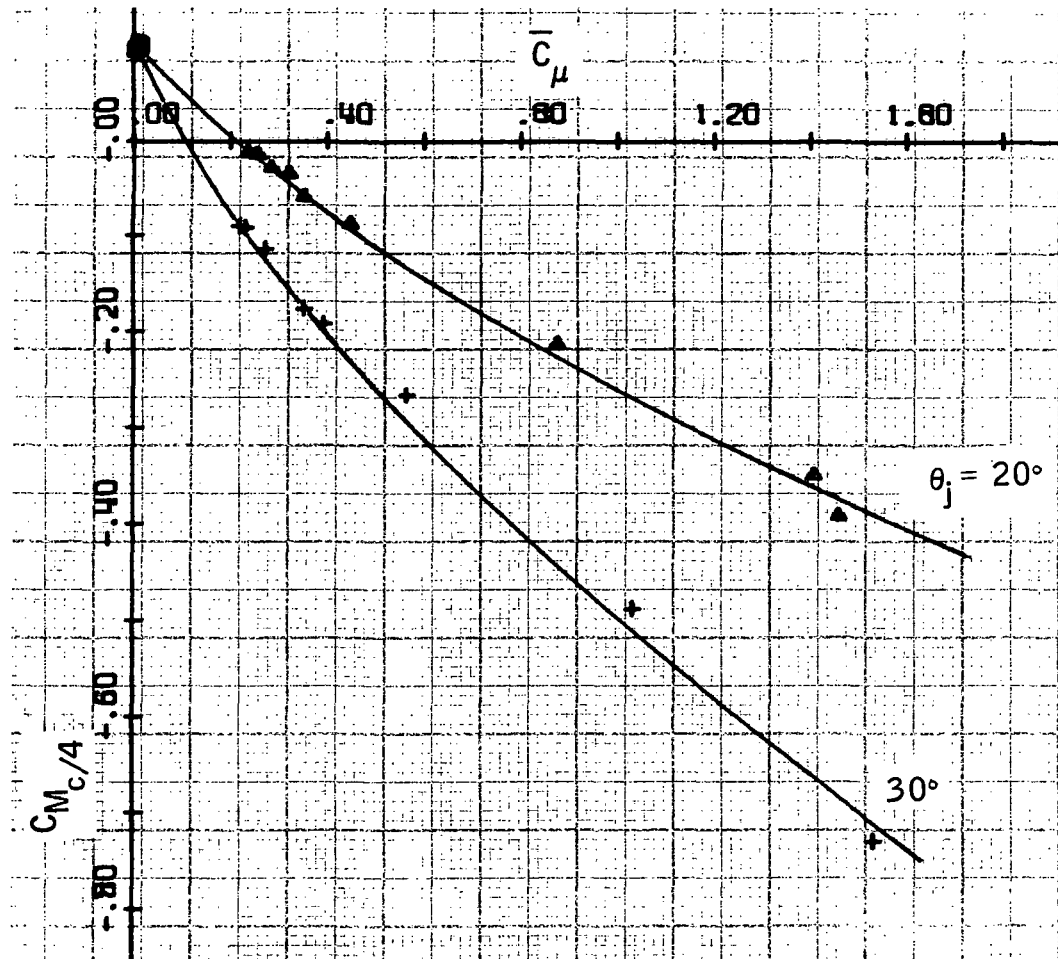


Figure 38. Quarter-Chord Moment Variation with Blowing Coefficient - Full-Span Blowing, $\alpha = 12$ degrees

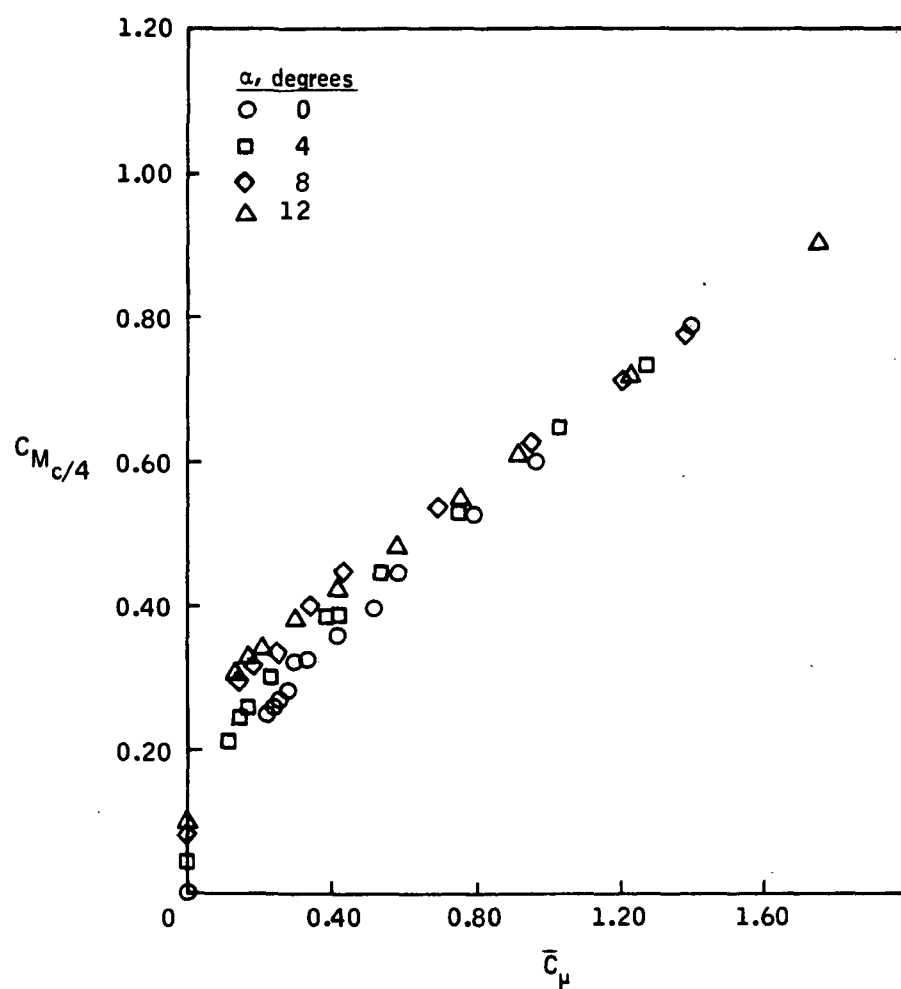


Figure 39. Quarter-Chord Moment Variation with Blowing Coefficient - Full-Span Blowing, $\theta_j = 30$ degrees

the results of reference 2, except as previously noted the values are higher in the positive direction than they should be.

Full-span, center-section blowing only. - The helicopter VDT-blade configuration most likely to be used on an actual helicopter rotor is part-span or sectional jet-flap blowing. This was best simulated in the wind tunnel tests by blowing the center section only, with the end sections unblown but at the same angle of attack.

Test results indicate that center-section blowing only can be used to produce lift forces nearly as effectively as full-span blowing. The effectiveness of this blowing condition would equal that of the full-span blowing if about one-third the lift increase that occurs with full-span blowing is produced with only the center section blowing. Three-dimensional effects at the ends of the blown section, however, may reduce the lift produced.

Figure 40 shows the lift coefficient as a function of blowing for all jet angles tested at zero angle of attack. The lift is approximately one-third the lift of corresponding full-blown data. The curves for $\theta_j = 30$ degrees and -30 degrees are again symmetrical about the zero-lift axis as one would expect. Figure 41 shows that at a specific blowing coefficient, in this case $\bar{C}_\mu = 0.40$, the lift for center-section blowing remains approximately one-third of full-span lift for angles of attack from 0 through 8 degrees.

The lift coefficients for full-span and center-section blowing at $\theta_j = 30$ degrees and -30 degrees are shown in Figures 42 through 45. In Figure 42 for zero angle of attack and 30-degree jet angle, the center-section lift percentage of the full-span lift is shown to be slightly less than 33. This percentage is approached at low-blowing coefficients but declines as the blowing coefficient increases. Figure 42 demonstrates the same trend for the -30 -degree jet angle. This trend may be explained by examining the three-dimensional effects present. When blowing the center section only, the shed vorticity influences the spanwise lift distribution by introducing a downwash over the center section and, in general, an upwash on the adjacent

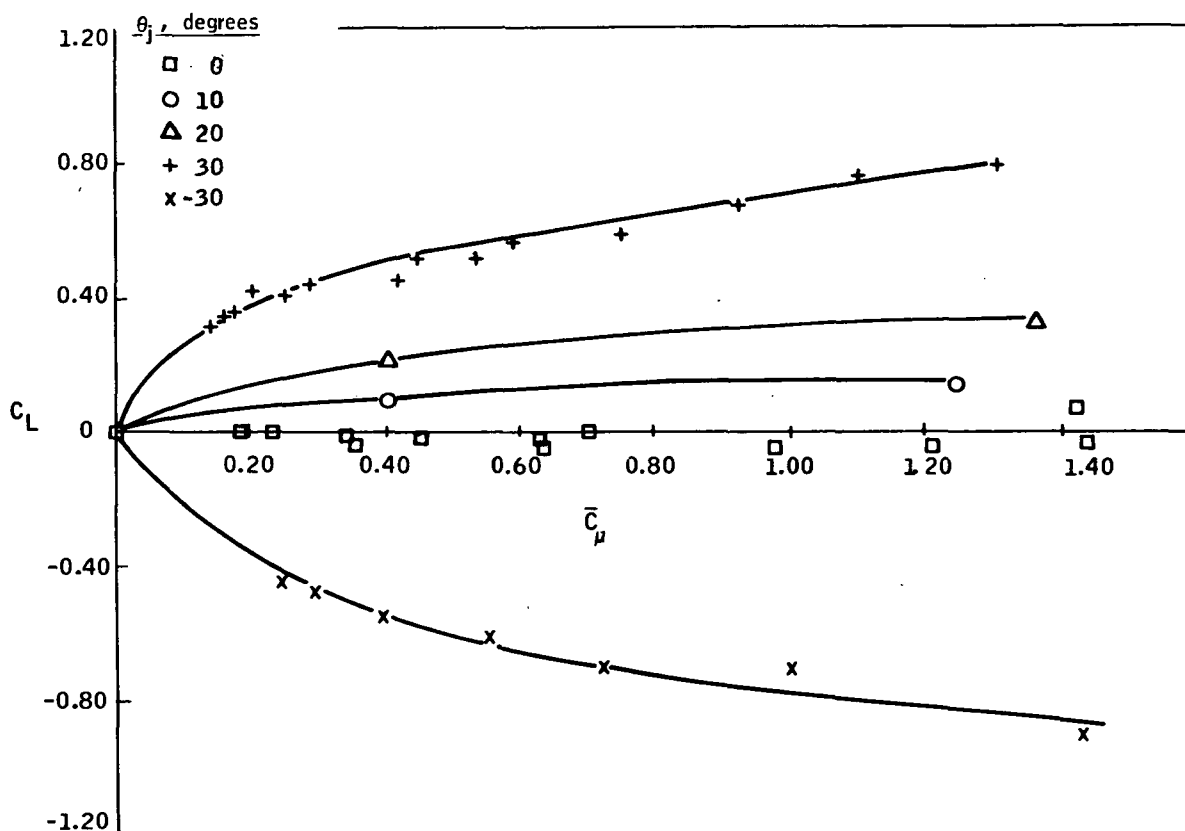


Figure 40. Lift Coefficient as a Function of Blowing Coefficient - Center-Section Blowing Only, $\alpha = 0$

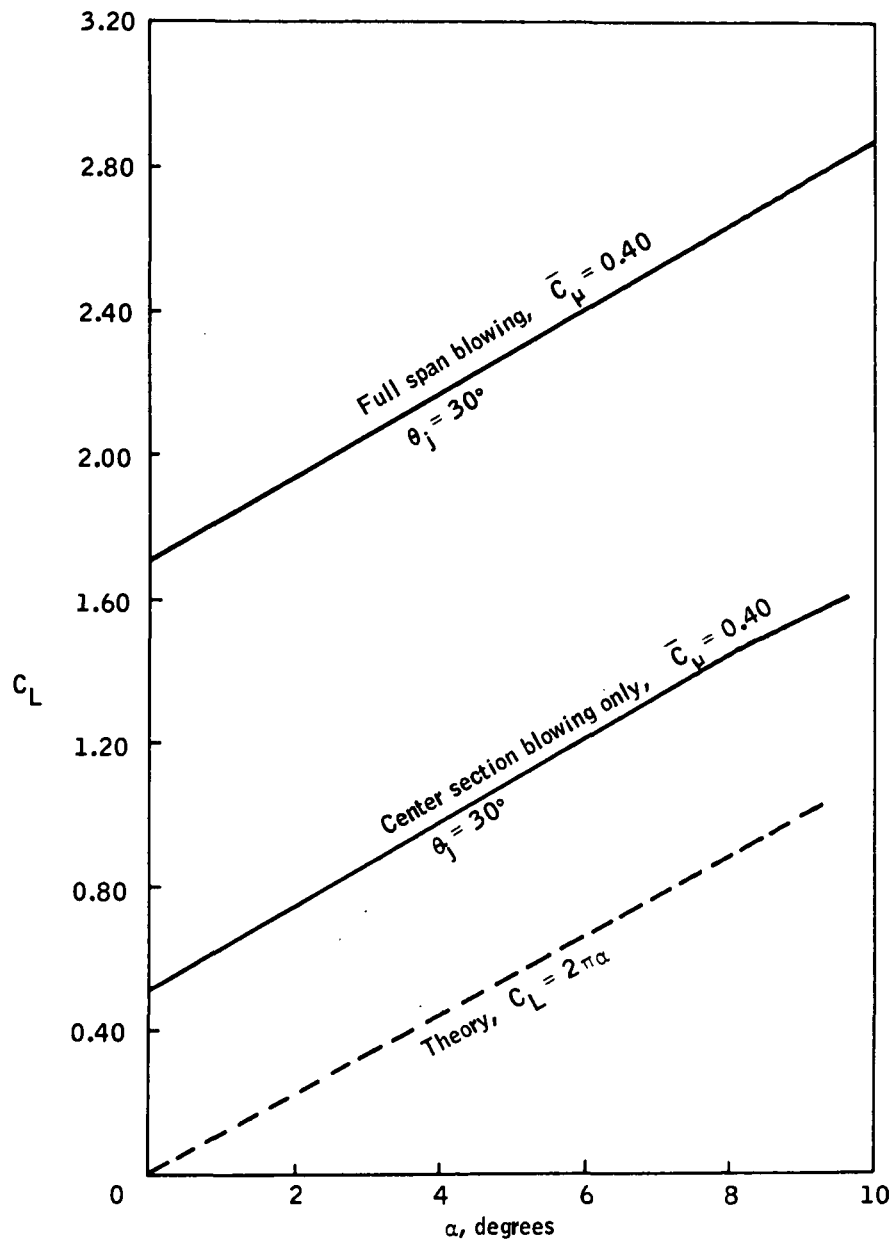


Figure 41. Lift Coefficient as a Function of Angle of Attack - Full-Span Blowing and Center-Section Blowing Only

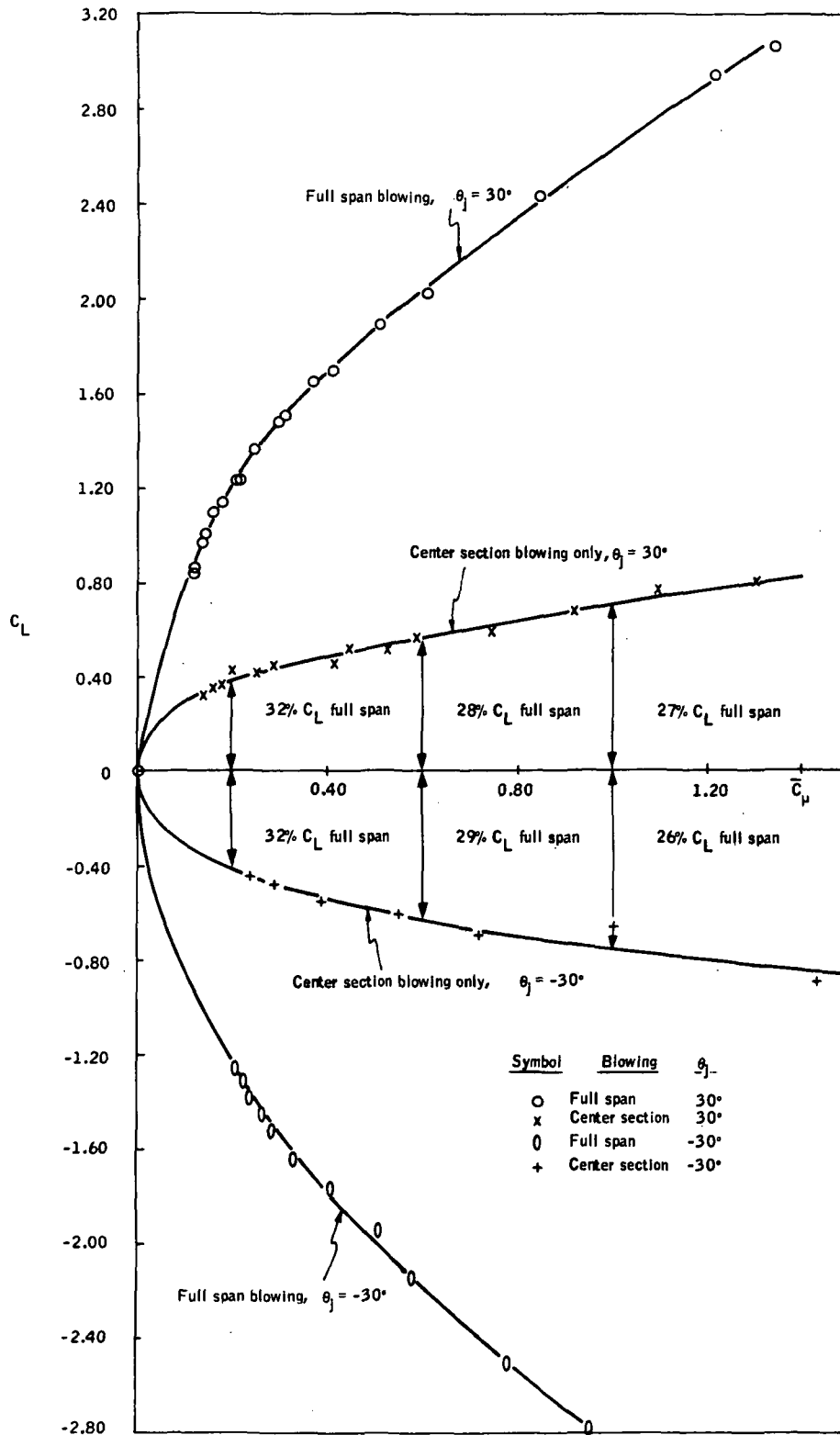


Figure 42. Lift Coefficient as a Function of Blowing Coefficient - Full-Span Blowing and Center-Section Blowing Only, $\alpha = 0$

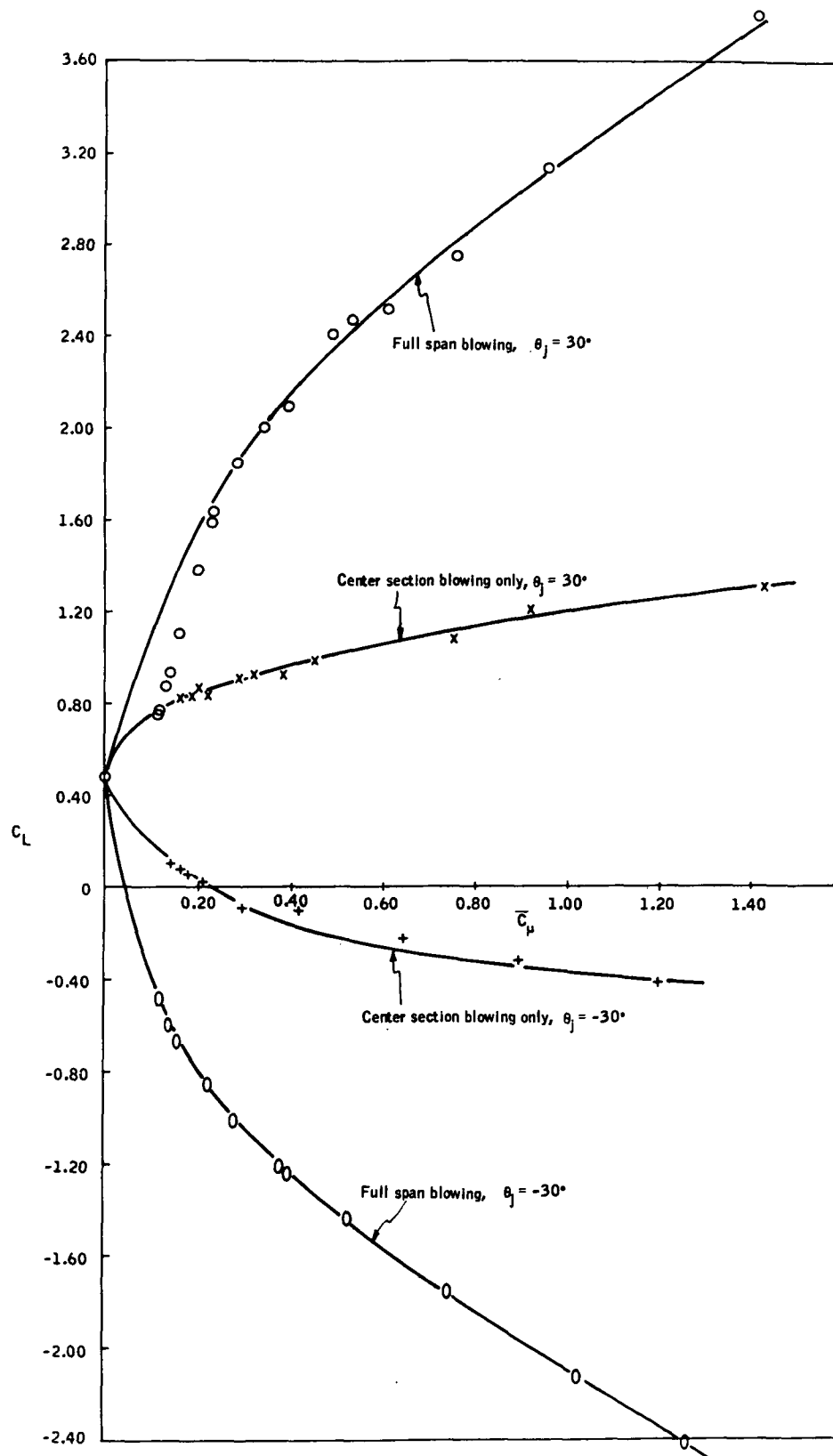


Figure 43. Lift Coefficient as a Function of Blowing Coefficient - Full-Span Blowing and Center-Section Blowing Only, $\alpha = 4$ degrees

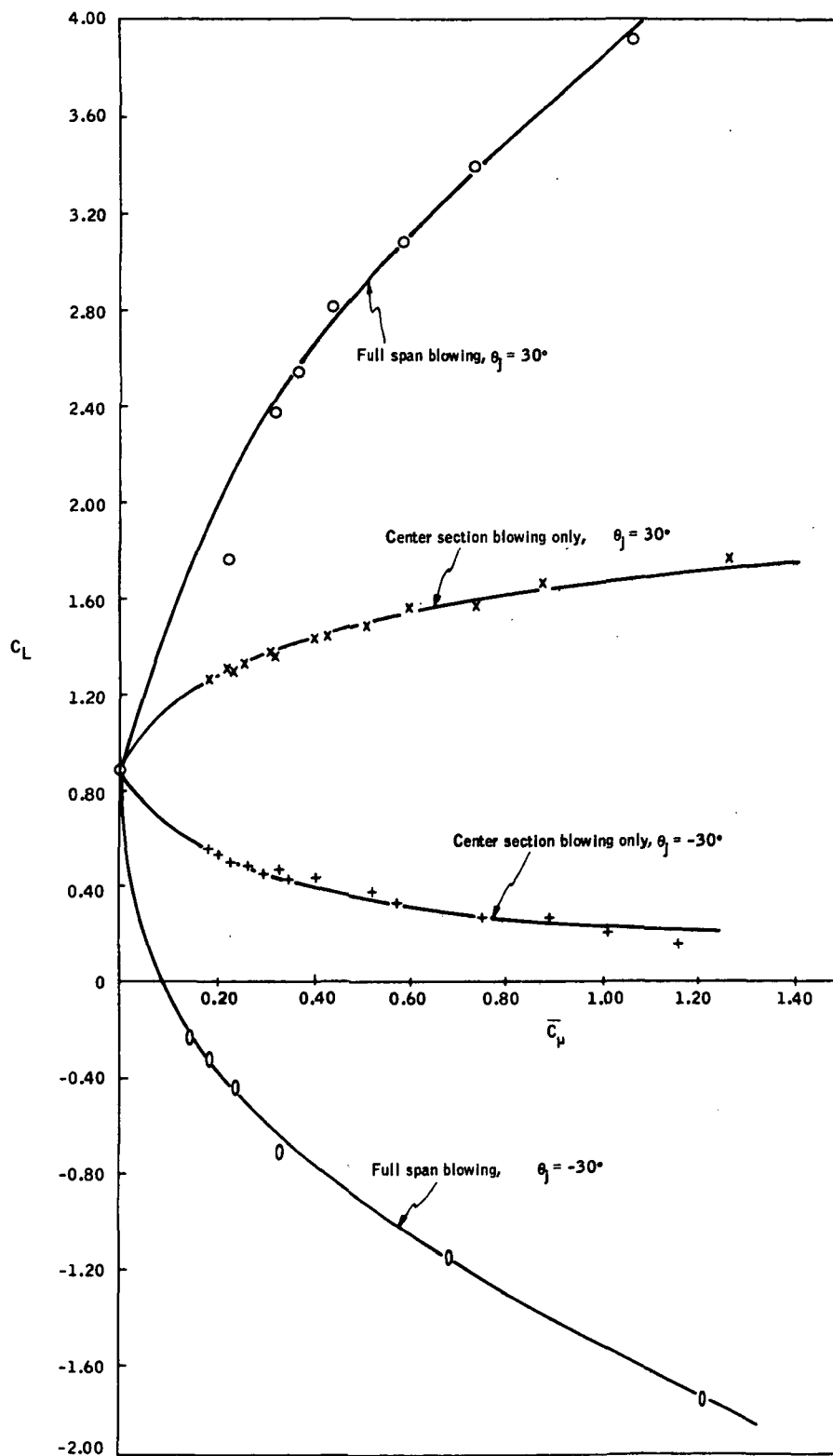


Figure 44. Lift Coefficient as a Function of Blowing Coefficient - Full-Span Blowing and Center-Section Blowing Only, $\alpha = 8$ degrees

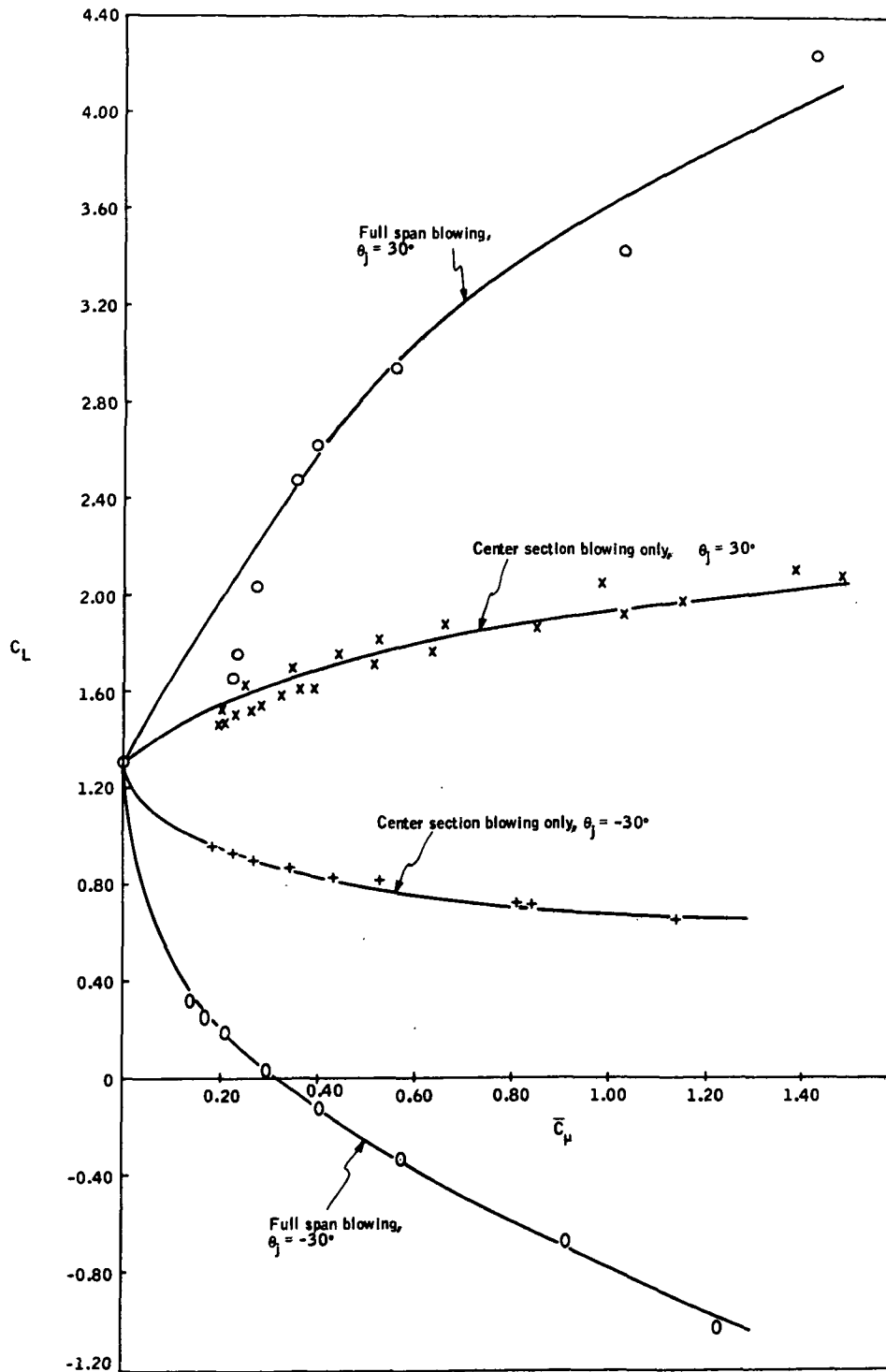


Figure 45. Lift Coefficient as a Function of Blowing Coefficient - Full-Span Blowing and Center-Section Blowing Only, $\alpha = 12$ degrees

end sections. As the blowing coefficient is increased, the strength of the shed vorticity increases, resulting in more three-dimensional effects which reduce the peak of the lift distribution further from the two-dimensional or full-span blowing lift value. The net result of the increased blowing is then a reduction in the ratio of the center-section-blown lift to the full-span-blown lift as shown in Figure 42. Figures 43 through 45 show the same curves for angles of attack of 4, 8, and 12 degrees.

The drag coefficient of the VDT-blade model with center-section blowing only at various jet angles and angles of attack 0 through 12 degrees is shown in Figures 46 through 49. The spread of the curves for center-section blowing is more distinct than that observed for full-span blowing (Figures 26 through 29). As discussed previously, the curve spread is a result of a drag due to lift greater than that encountered in two-dimensional tests. This can be attributed to the three-dimensional effects induced by blowing the center section only. The effect is similar to that produced by finite aspect ratio. A similar curve spread was noted in reference 2 for tests of the center section with endplates, which had an effective aspect ratio of approximately 8.0.

The quarter-chord moment coefficient variation for the complete VDT-blade with center-section blowing only is presented in Figures 50 through 54. These plots show little variation of quarter-chord moment with change of angle of attack. The center-section-blowing-only moment values are approximately one-third the moments obtained for full-span blowing. The values increase very slightly as the angle of attack increases.

Steady-State Tests with Lift Controller (Closed-Loop)

With the VDT-blade model installed in the wind tunnel test section, a number of tests were conducted for two types of parameter changes:

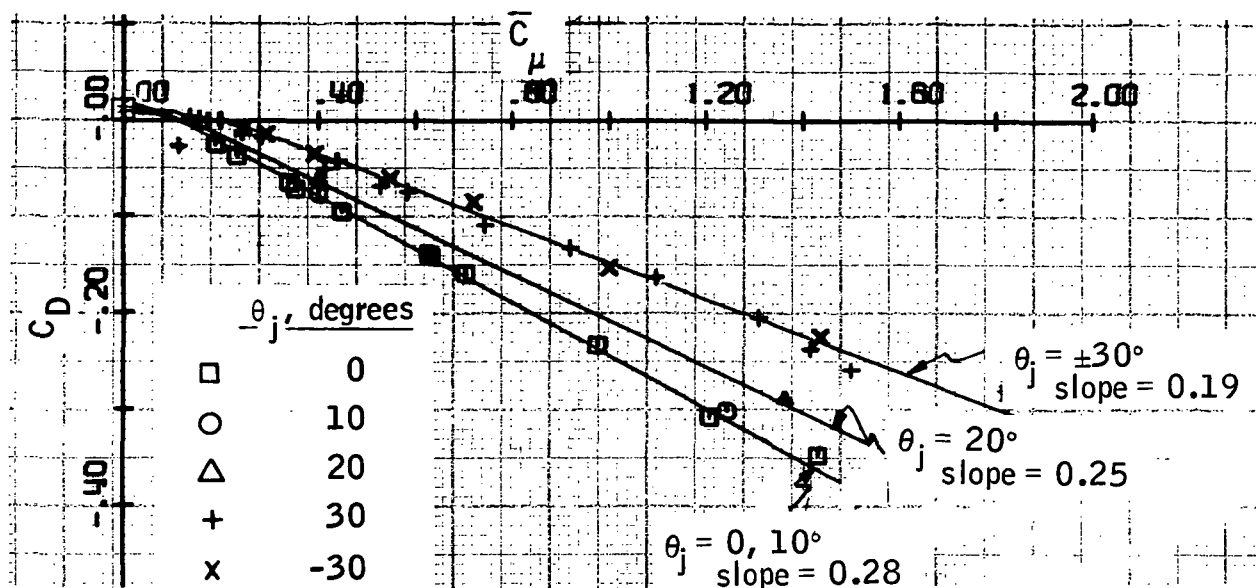


Figure 46. Drag Reduction Due to Center-Section Blowing Only - $\alpha = 0$

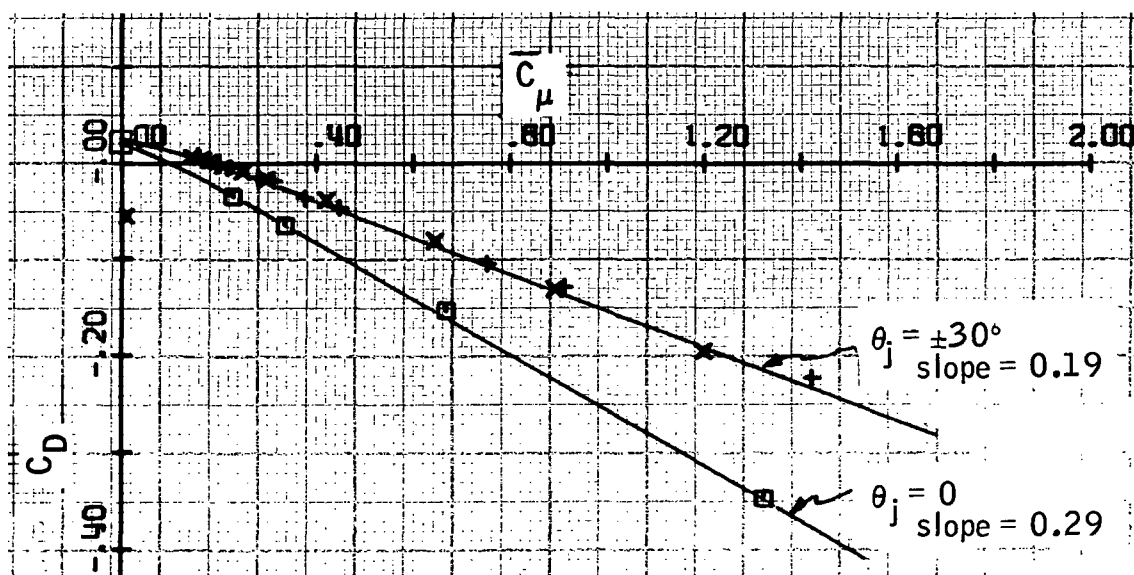


Figure 47. Drag Reduction Due to Center-Section Blowing Only - $\alpha = 4$ degrees

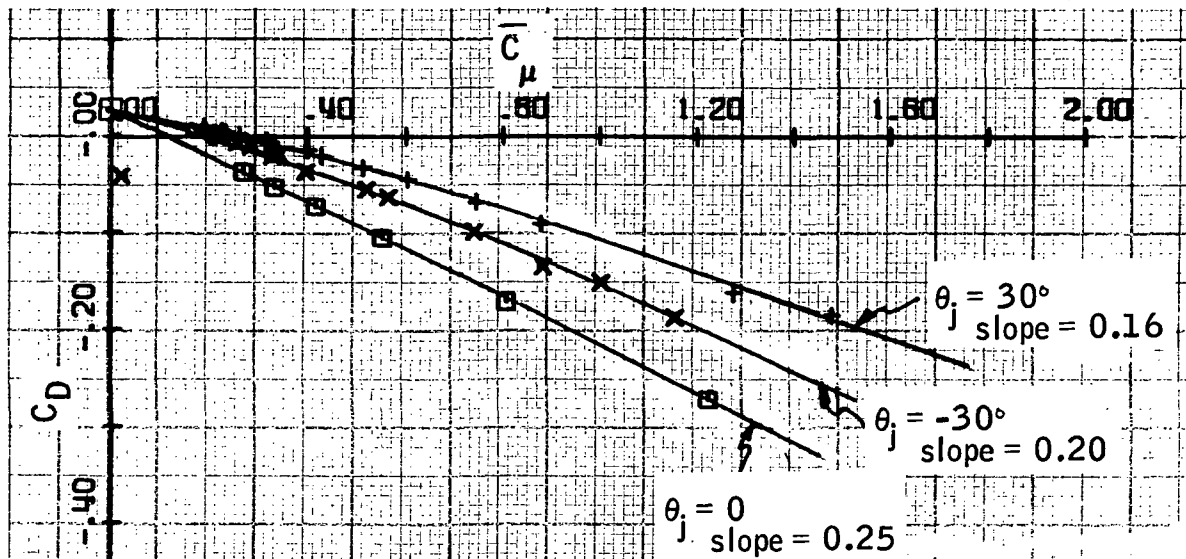


Figure 48. Drag Reduction Due to Center-Section Blowing Only - $\alpha = 8$ degrees

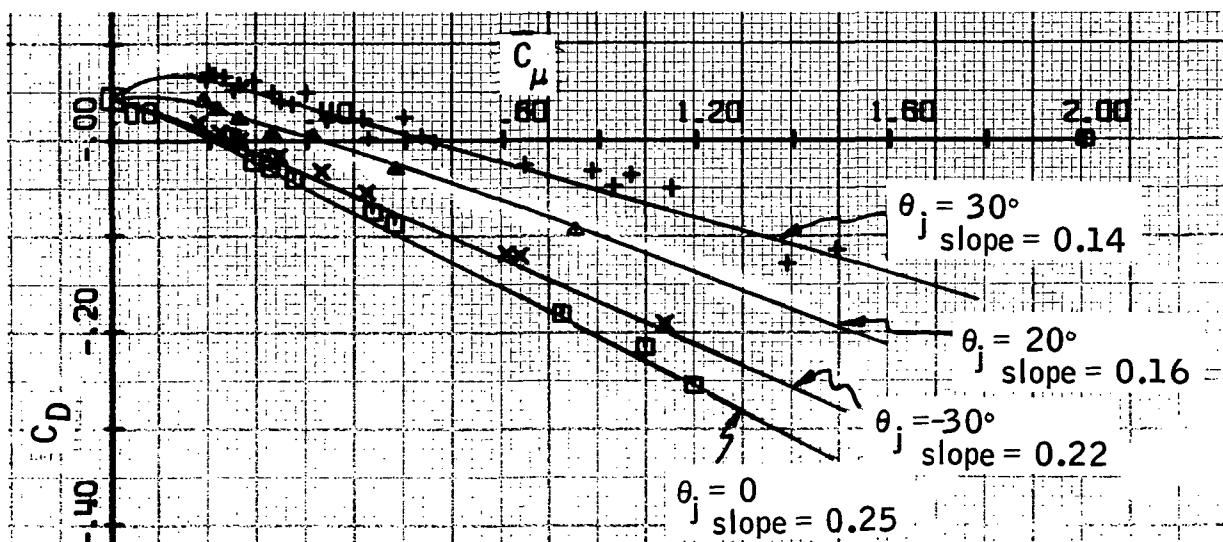


Figure 49. Drag Reduction Due to Center-Section Blowing Only - $\alpha = 12$ degrees

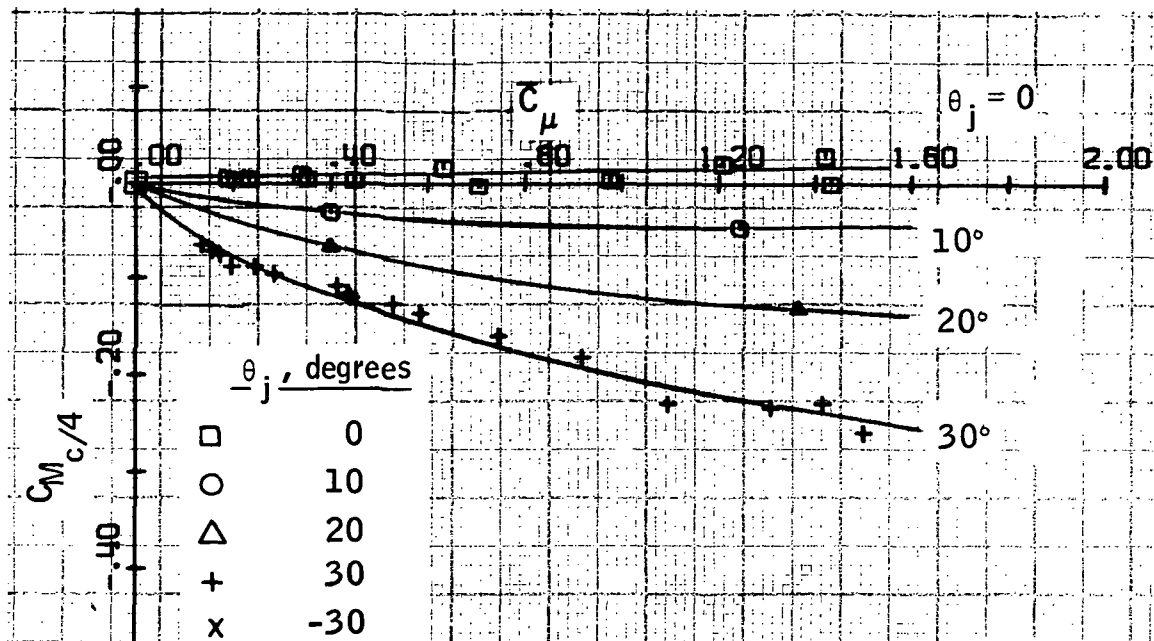


Figure 50. Quarter-Chord Moment Due to Center-Section Blowing Only - $\alpha = 0$

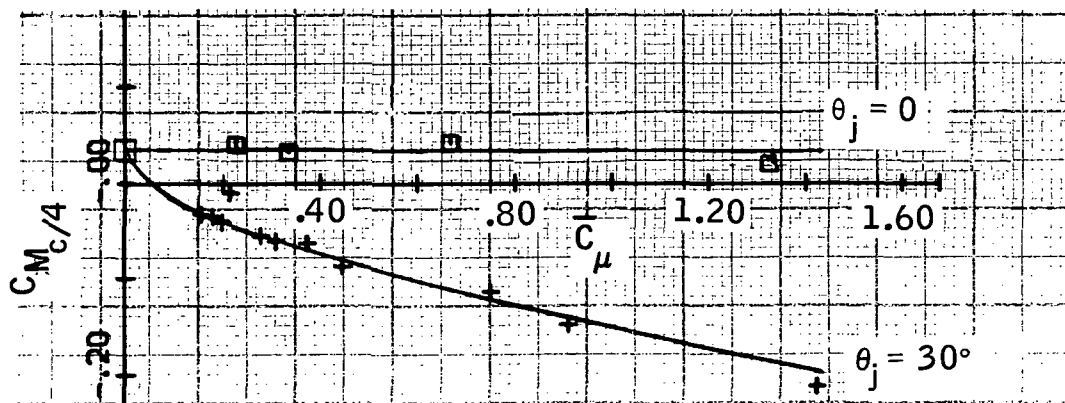


Figure 51. Quarter-Chord Moment Due to Center-Section Blowing Only - $\alpha = 4$ degrees

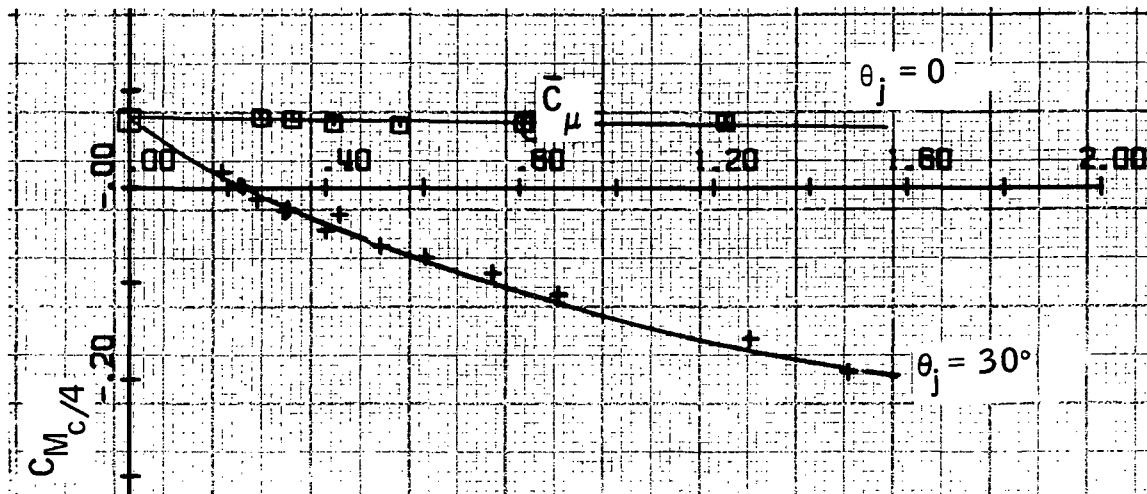


Figure 52. Quarter-Chord Moment Due to Center-Section Blowing Only - $\alpha = 8$ degrees

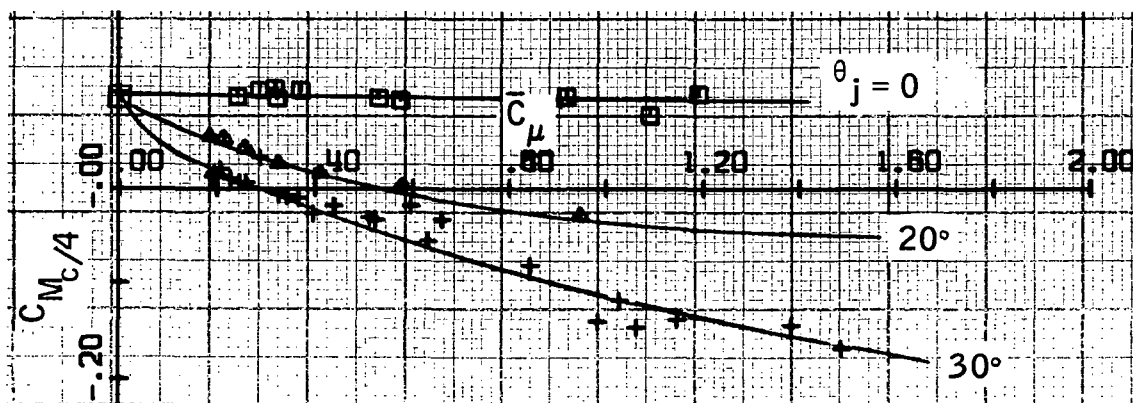


Figure 53. Quarter-Chord Moment Due to Center-Section Blowing Only - $\alpha = 12$ degrees

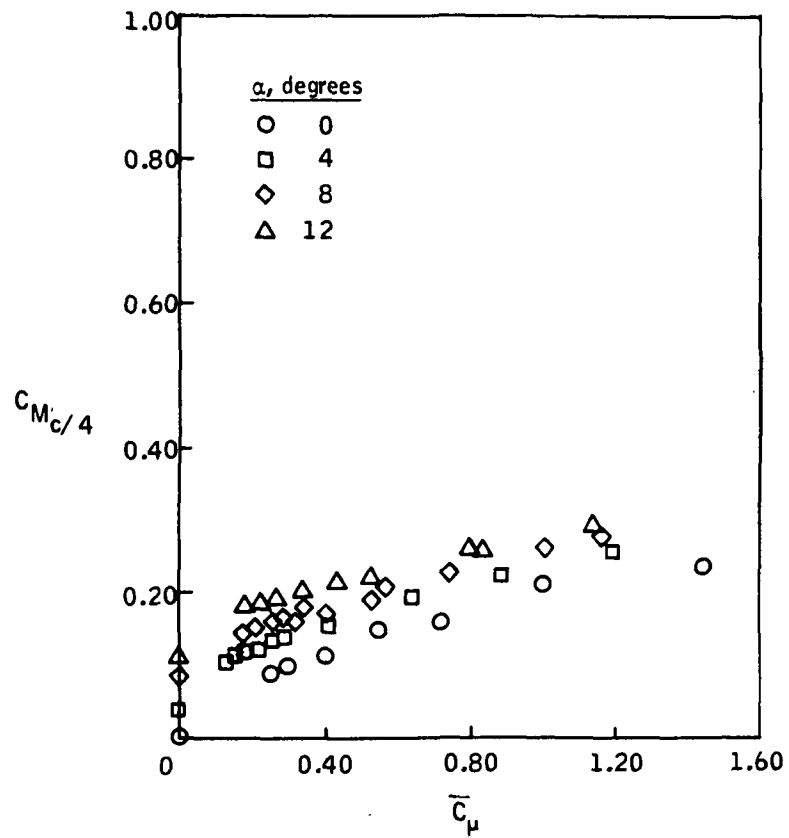


Figure 54. Quarter-Chord Moment Due to Center-Section Blowing Only - $\theta_j = 30$ degrees

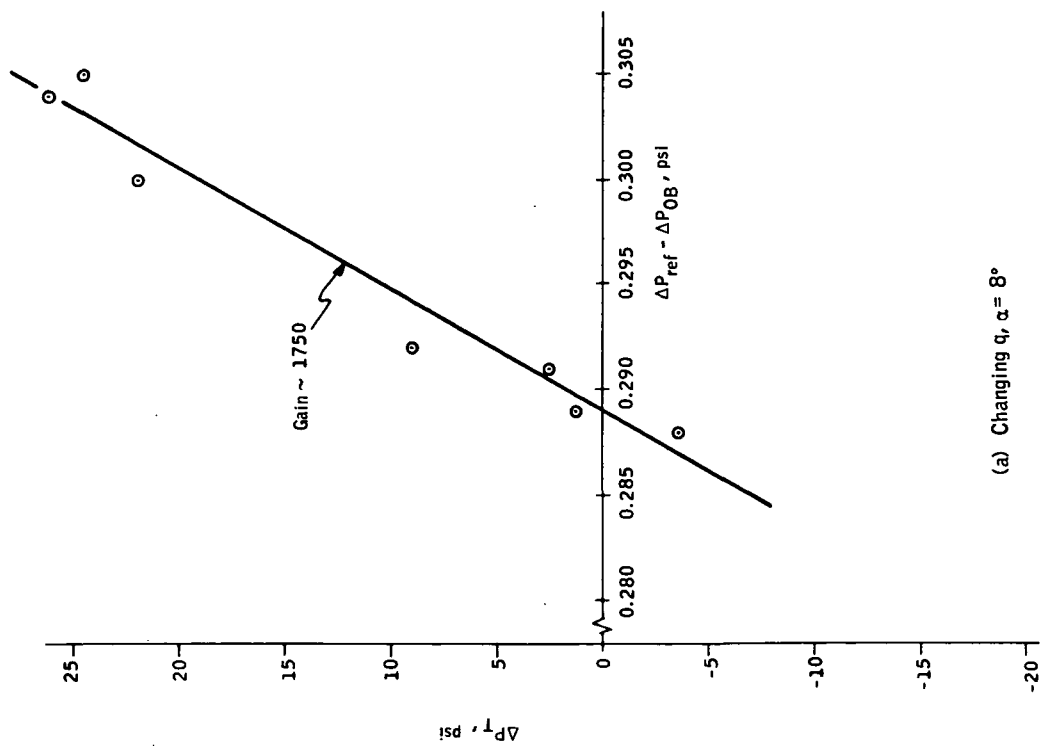
- Constant α , q varying from 10 to 100 psf, and
- Constant q , α varying from -4 to 12 degrees.

Most of the test runs were done with varying q . The test results for varying α were inconsistent, and most of this data has been omitted from the report.

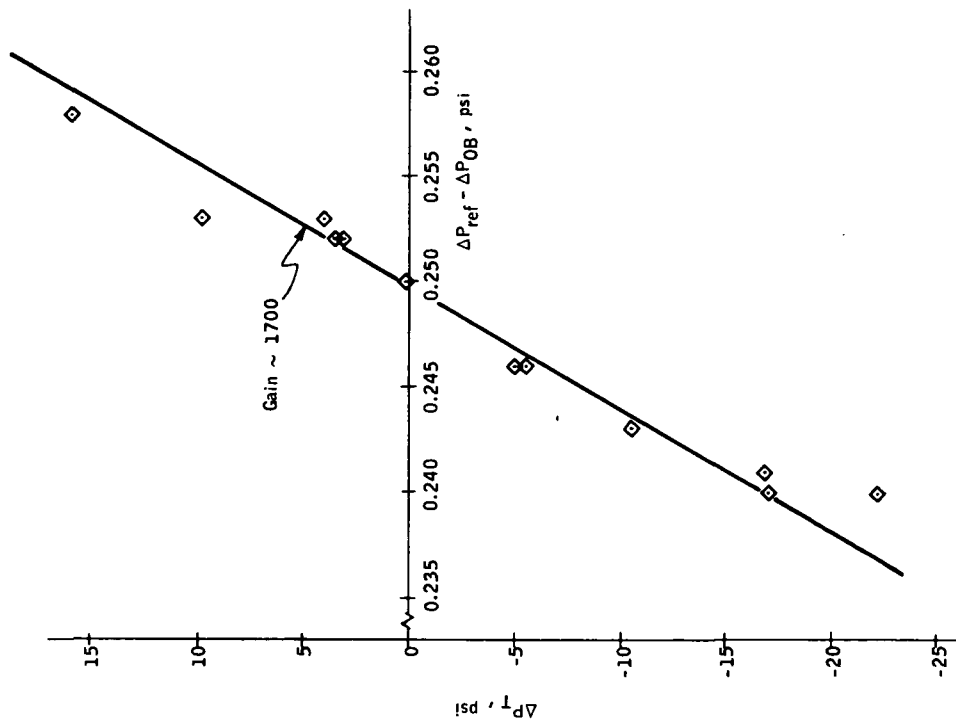
Fluidic amplifier performance. - The control system was designed to have a gain of 2000 from the downstream side of the outbleed system to the VDT plenum chambers. Pressure taps located before the amplifier cascade (Figure 7) measured ΔP_{ref} and ΔP_{OB} and taps in the VDT plenums determined ΔP_{T} . Data from these pressure taps was taken for only a few of the test runs and examples of the results are shown in Figure 55. A variation in the amplifier gain from 1400 to 1950 was noted during testing. However, the fluidic amplifiers generated an average gain of approximately 1700.

Outbleed system and controller gain. - The VDT-blade model surface pressure taps were used to determine the relationship between the outbleed system differential pressure (ΔP_{OB}) and the midchord surface differential pressure ($\Delta P_{\text{c}/2}$). Since a number of surface pressure taps were bad, including those near midchord, pressure-distribution curves were plotted using the good taps and extended through the midchord position to estimate $\Delta P_{\text{c}/2}$.

A linear relationship between the estimated $\Delta P_{\text{c}/2}$ values and ΔP_{OB} was determined as shown in Figure 56. The data scatter shown in Figure 56 is probably the result of inaccuracies in estimating $\Delta P_{\text{c}/2}$ and in determining ΔP_{OB} (which is a small difference of two larger values). However, the trends shown by the data indicate that there was a gain reduction of 1/6 to 1/9 in the outbleed scheme used to transfer $\Delta P_{\text{c}/2}$ to the preamplifiers. Thus, although the fluidic amplifiers operated at a gain of 1700, the overall system gain (defined by the change in VDT tank pressures with changing



(a) Changing α , $\alpha = 8^\circ$



(b) Changing α , $\alpha = 53^\circ$

Figure 55. Fluidic Amplifier Gains from Downstream Side of Outbleed System to VDT Tanks

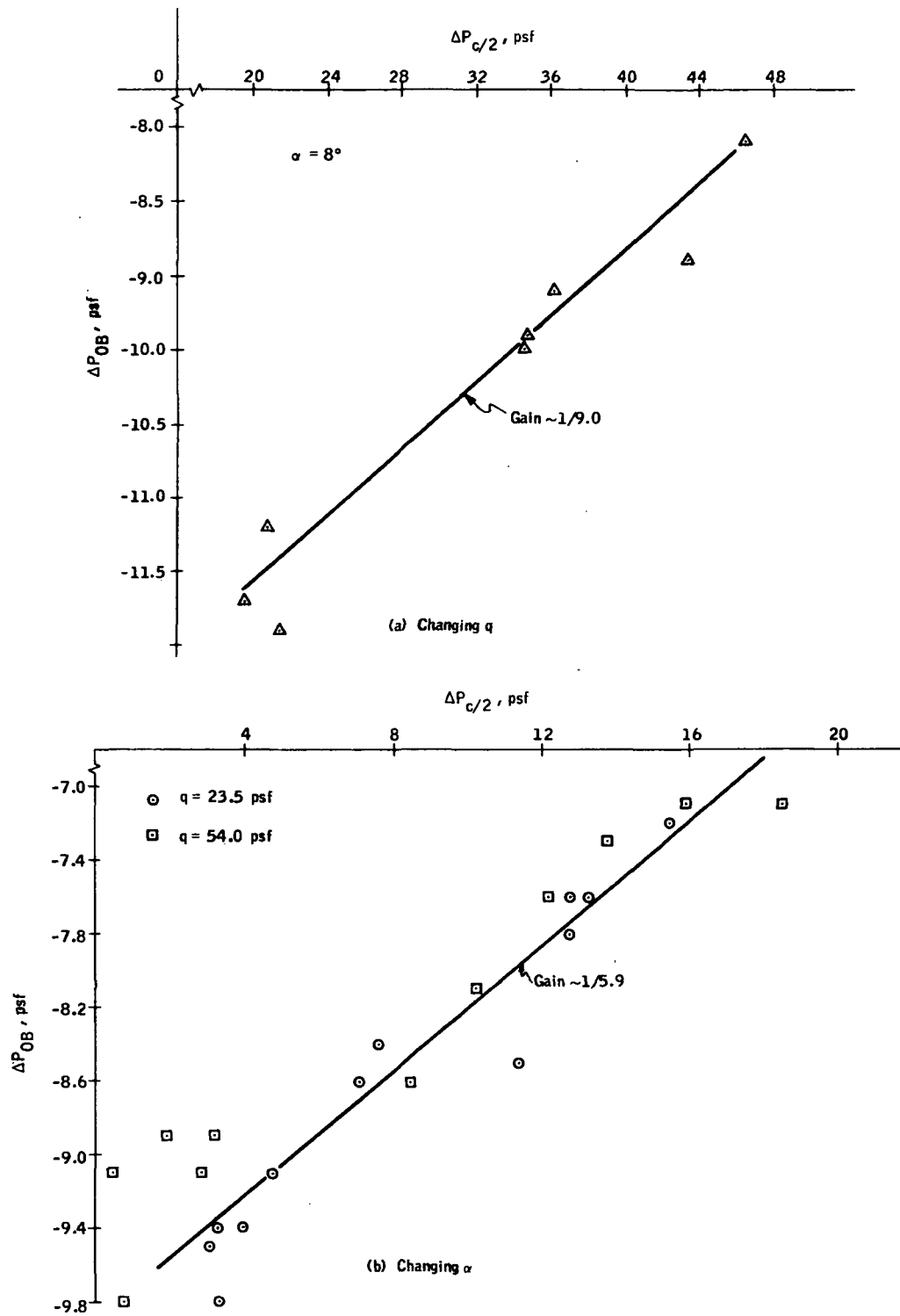


Figure 56. Backpressures in Outbleed System Compared to Wing $\Delta P_{c/2}$

$\Delta P_{c/2}$) is indicated to be in the range from 190 to 280. To more accurately determine the overall system gain, the $\Delta P_{c/2}$ values were plotted versus the VDT tank pressure difference (ΔP_T) in Figure 57. This is a plot of several test runs with α constant and q varying such that the initial conditions for ΔP_T were the same in all cases. A system gain of approximately 225 is indicated from the data in Figure 57.

This reduction in overall system gain was not anticipated prior to the wind tunnel tests. It apparently resulted from a malfunction in the outbleed circuitry and can be eliminated by redesigning the outbleed system or increasing the preamplifier gain. The amplifier gain can be increased by simply adding an additional stage to the amplifier cascade.

The effect of reducing the system gain from the design value of 2000 to 225 was estimated from a math model of the control loop which is derived in the Appendix. Figure 58 shows the expected theoretical lift output of the VDT-controlled airfoil at $\alpha = 12$ degrees. Both curves start with a desired lift of 268 pounds at $q = 14.3$ psf and at $q = 100$ psf the predicted lift is 285 pounds for the system with gain 2000 and 408 pounds for the control system with gain 225. For this particular change in q , the gain 2000 maintains the desired lift within 6.4% and a gain of 225 allows the lift to climb to a value 48.6% higher than that originally desired.

Model spanwise lift characteristics. - The fluidic control system operated to change the jet angle in the VDT-blade model center section only, which was the only blown section for closed-loop operation. Hence, three-dimensional effects are present, and the shed vorticity from the blown section influences the spanwise lift distribution over the complete blade span. This test configuration is similar to a case tested in reference 10 where a two-dimensional NACA 0012 jet flap airfoil model was blown over 46% of the full span. Pressure tap instrumentation along the model span at midchord allowed some estimates of the spanwise lift distribution to be made. Figure 59 shows an example of the distribution found for the part-span blowing tests of reference 10. The present test configuration will result in a similar distribution of lift.

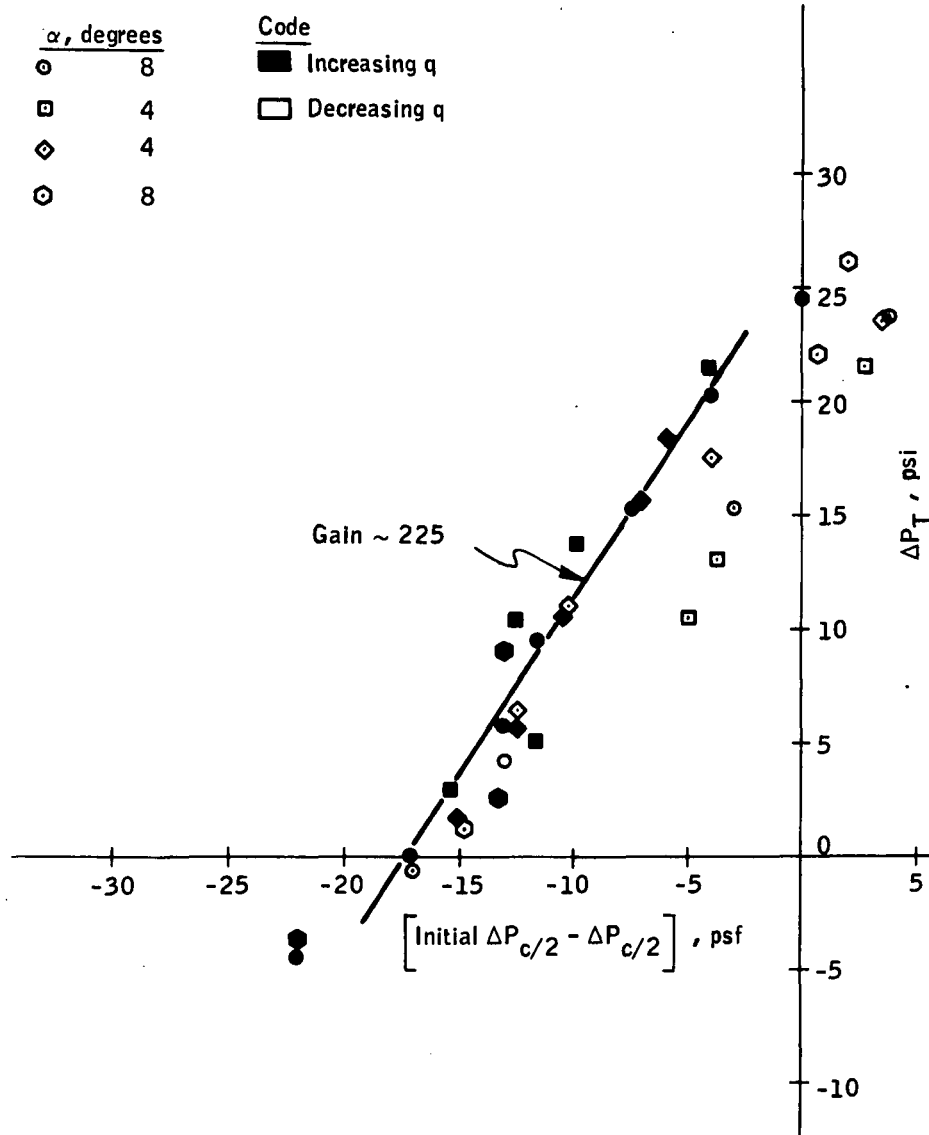
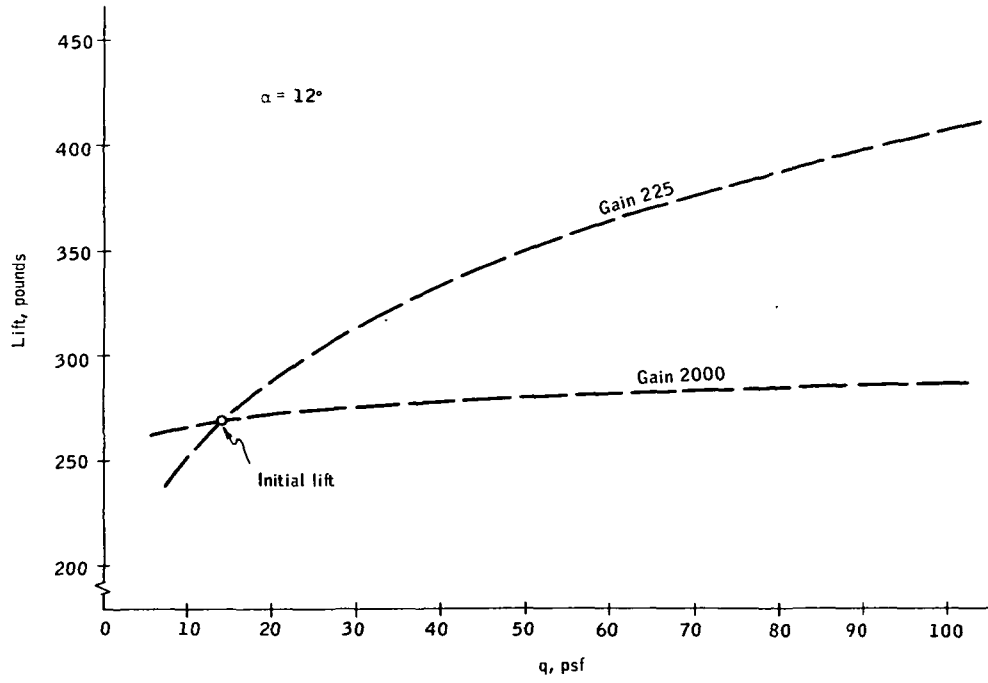
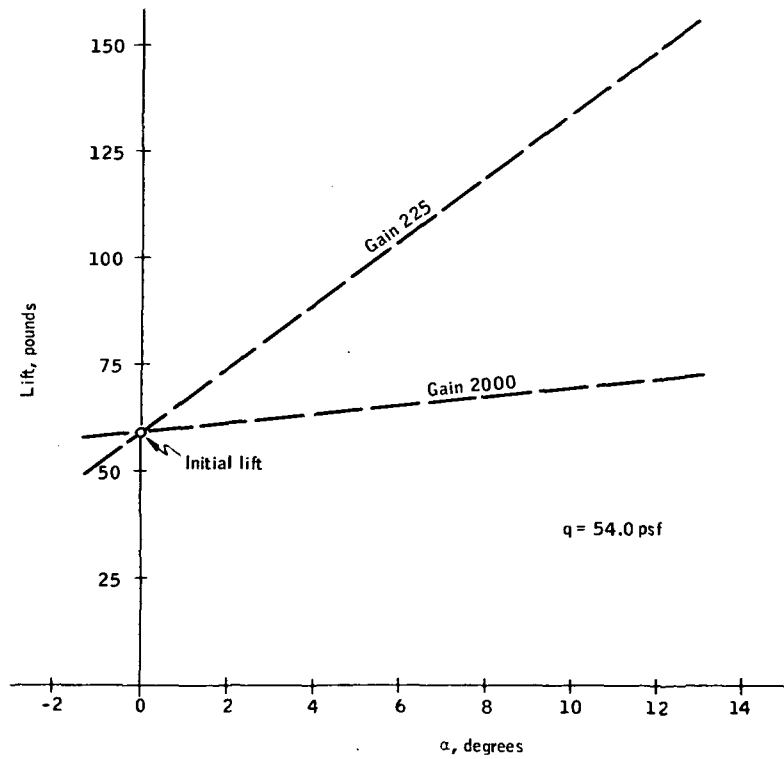


Figure 57. Control System Gain for Changing q-Tests at Constant α



(a) Changing q



(b) Changing α

Figure 58. Theoretical Lift Values Produced by Fluidic Control System on Two-Dimensional VDT-Blade Model

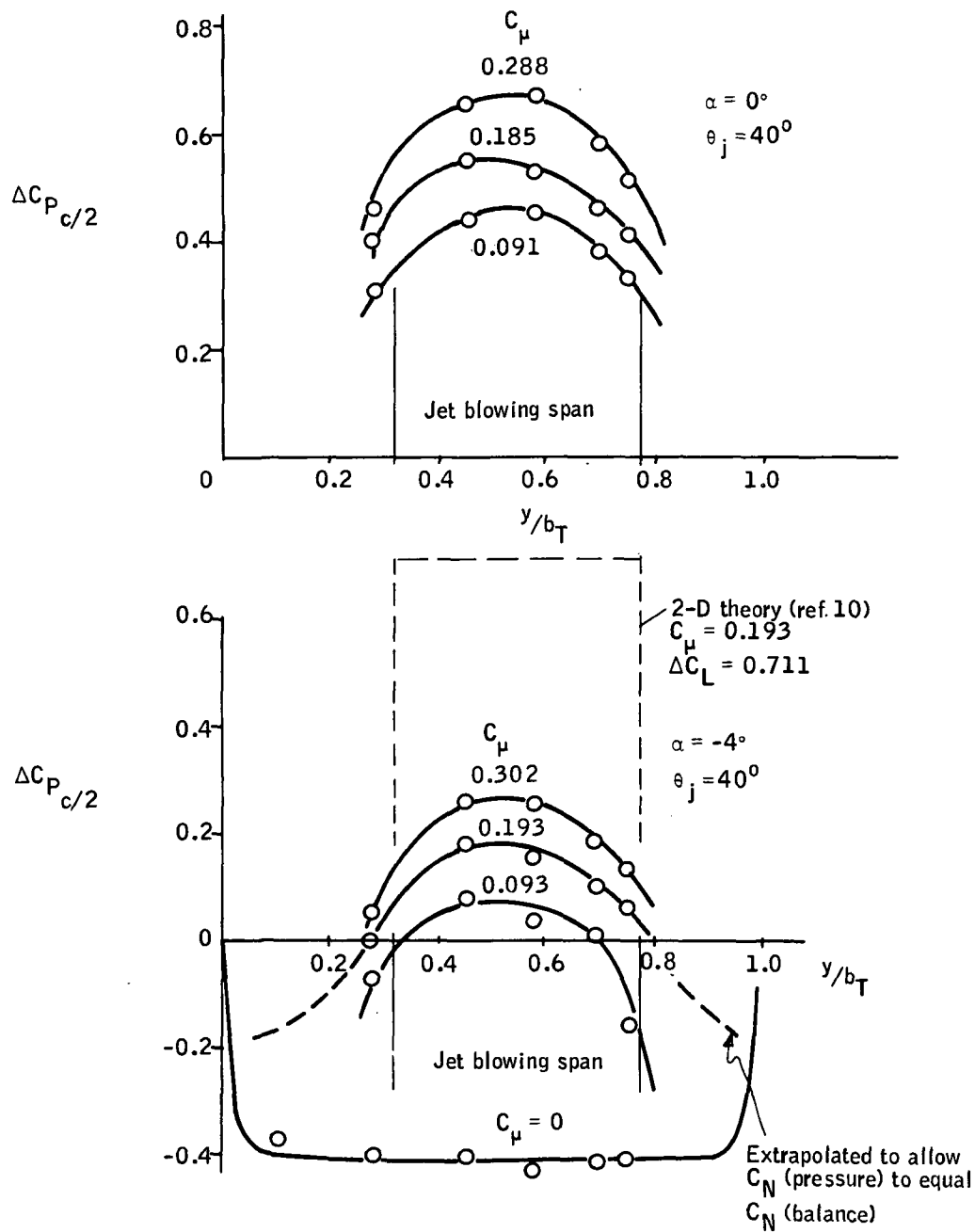


Figure 59. Spanwise Midchord Pressure Distribution - 46-percent Blown Span, Infinite-Aspect-Ratio Wing (ref. 10)

Since a lift roll-off occurs spanwise over the VDT-blade model, the internal balance system (IBS) measures an average lift over the surface. The average lift will be lower than that sensed at the model mid-span and can be less than that required to maintain a constant lift on the model section. To eliminate this difficulty, spanwise pressure-sensing ports at midchord could be used to sense the average lift.

The center-section lift, as measured by the IBS, deviates slightly from a linear relationship but is approximately linear with $\Delta P_c/2$, as shown in Figure 60.

Lift controller results. - Experimental and theoretical curves of lift versus free-stream dynamic pressure, q , for angles of attack from 0 to 12 degrees are presented in Figure 61. Spence's two-dimensional theory (ref. 5) was used in generating the curve of the theoretical lift controller behavior at a gain of 225. For the center-section-blowing-only test configuration, it is seen that the lift measured by the internal balance system is much lower than that which would have been obtained two-dimensionally at the same α , C_μ and θ_j conditions. By assuming that the midspan position of the VDT-blade model sees an essentially two-dimensional flow field, the parameters α , C_μ , and θ_j define a lift according to Spence's equation. The assumption used for this transformation should be a fair approximation to the actual two-dimensional state. The lift data, as corrected to two-dimensional flow, agrees well with the predicted control system lift at a gain of 225, as shown in Figures 61 through 64. It is also seen that the experimental data, although lower than the "2-D corrected lift" data, indicates the same trends as predicted for the control system operating in a two-dimensional environment. At a gain of 225, the control system operates with a large offset or lift error, and a noticeable increase in lift with increasing q results.

The two-dimensional lift which the airfoil would have experienced had the lift controller not changed the VDT jet angle is also shown in Figures 61 through 64. By comparing these curves to the controller operating data, it

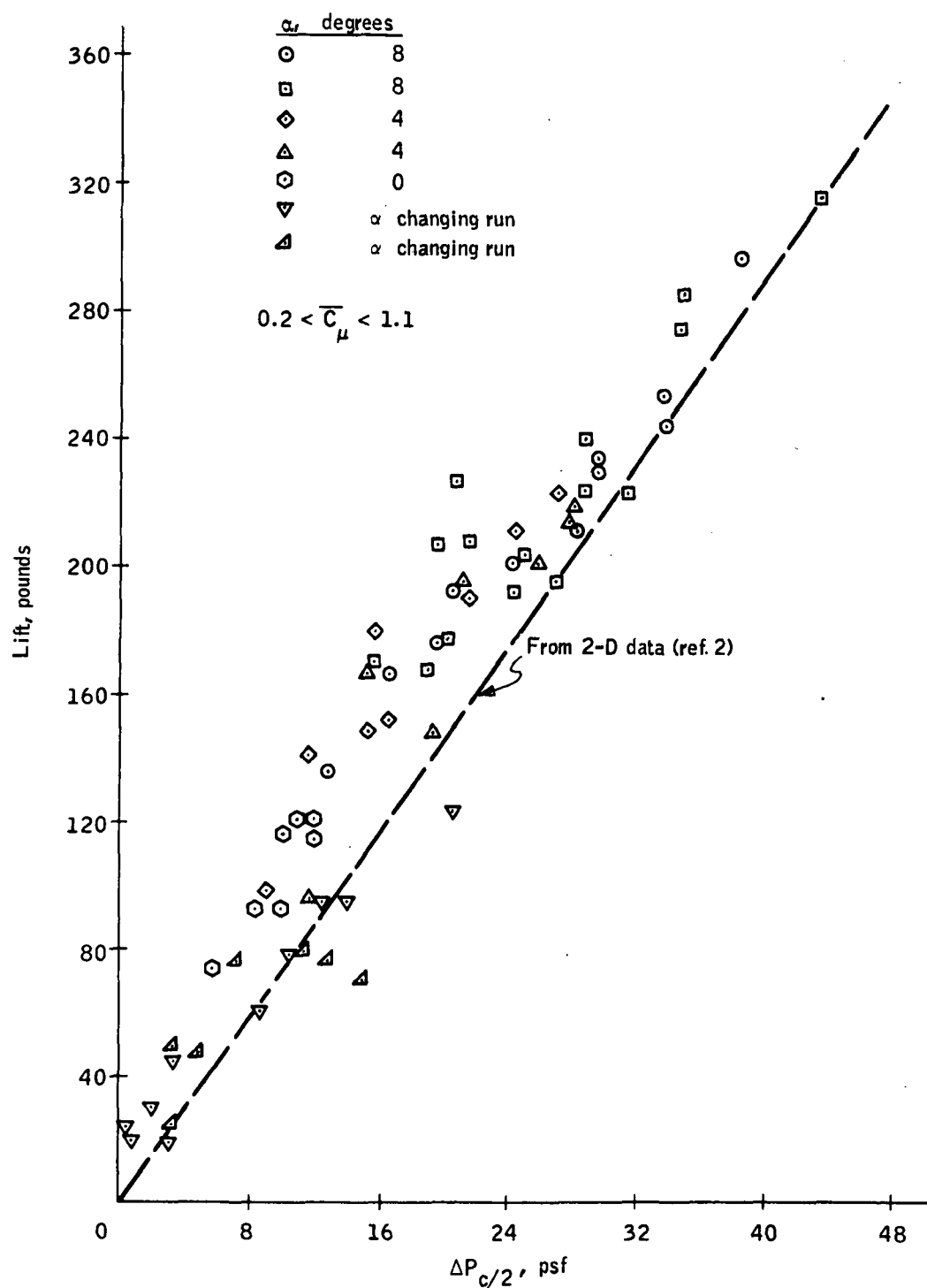


Figure 60. Center-Section Lift as a Function of $\Delta P_{c/2}$ for Center-Section Blowing Only (IBS data)

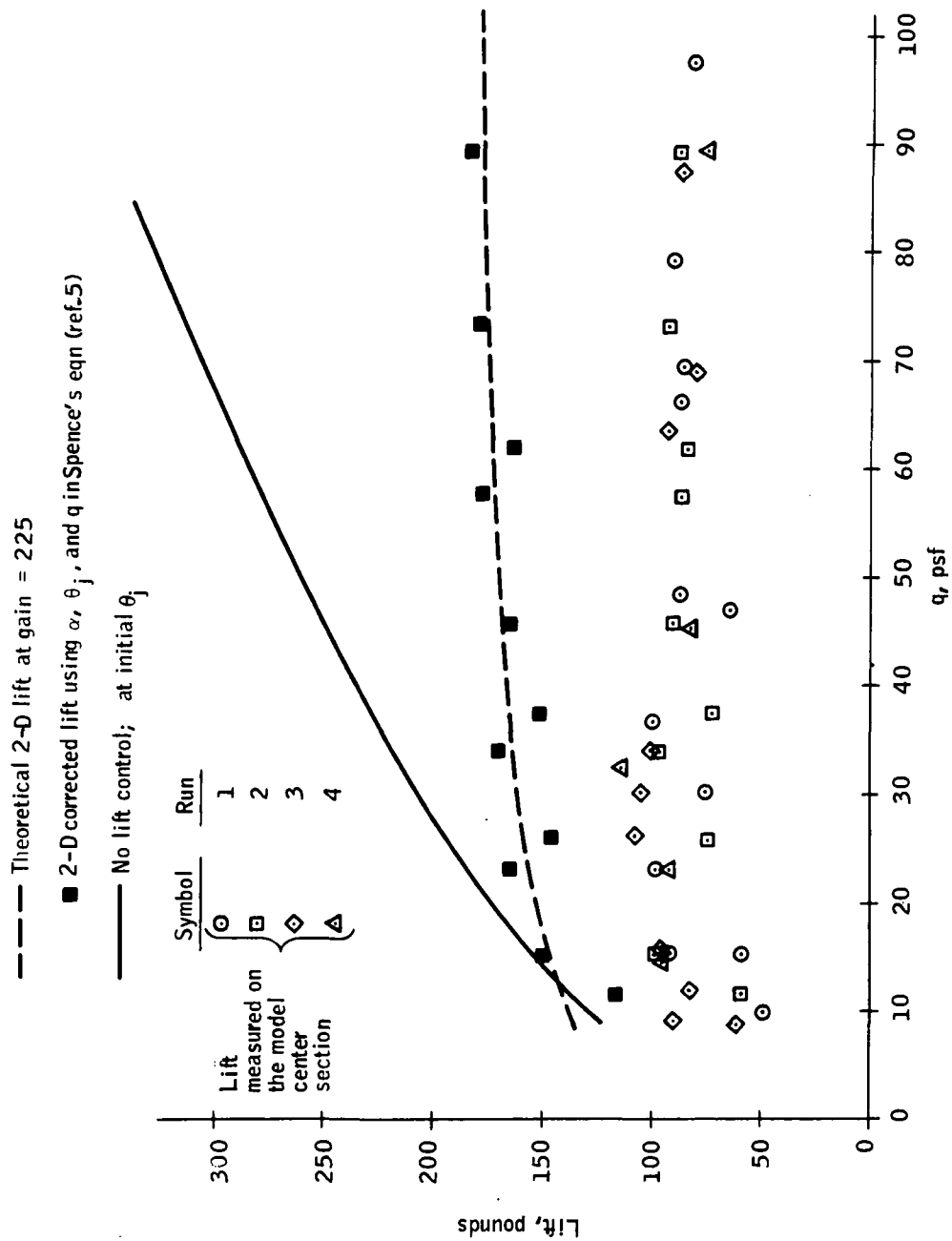


Figure 61. VDT-Blade Lift Variation with Free-Stream Dynamic Pressure - $\alpha = 0$

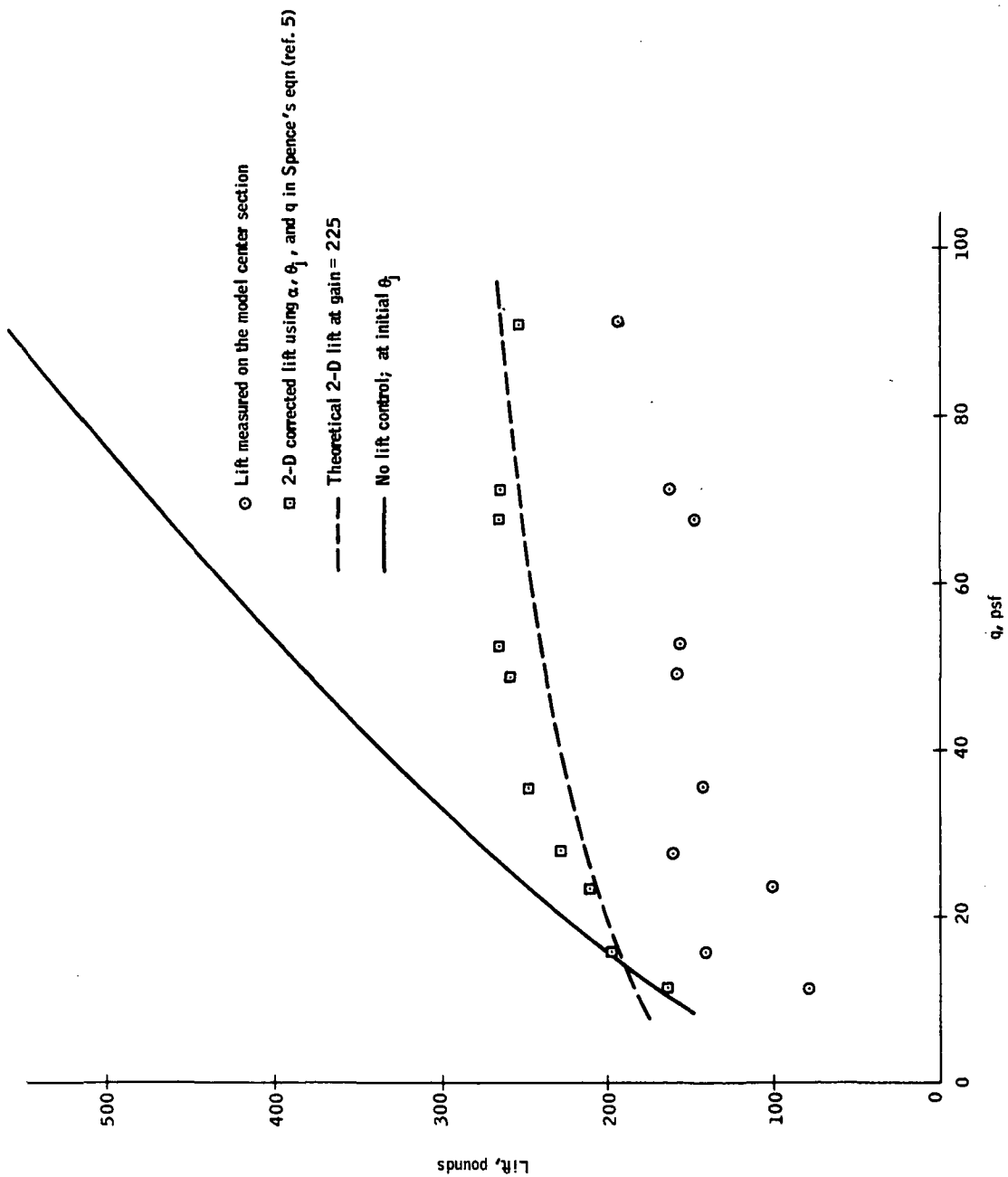


Figure 62. VDT-Blade Lift Variation with Free-Stream Dynamic Pressure - $\alpha = 4$ degrees

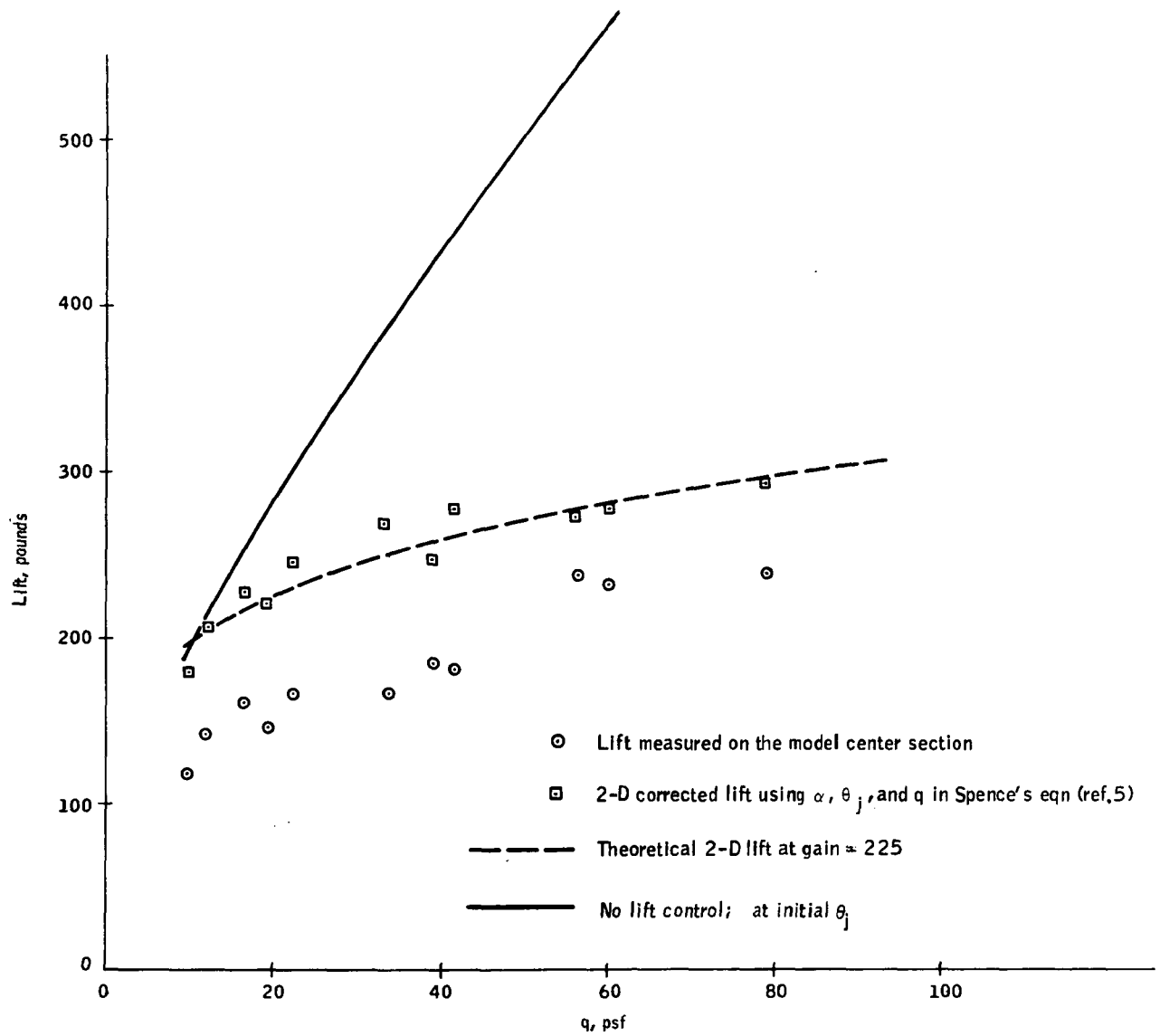


Figure 63. VDT-Blade Lift Variation with Free-Stream Dynamic Pressure - $\alpha = 8$ degrees

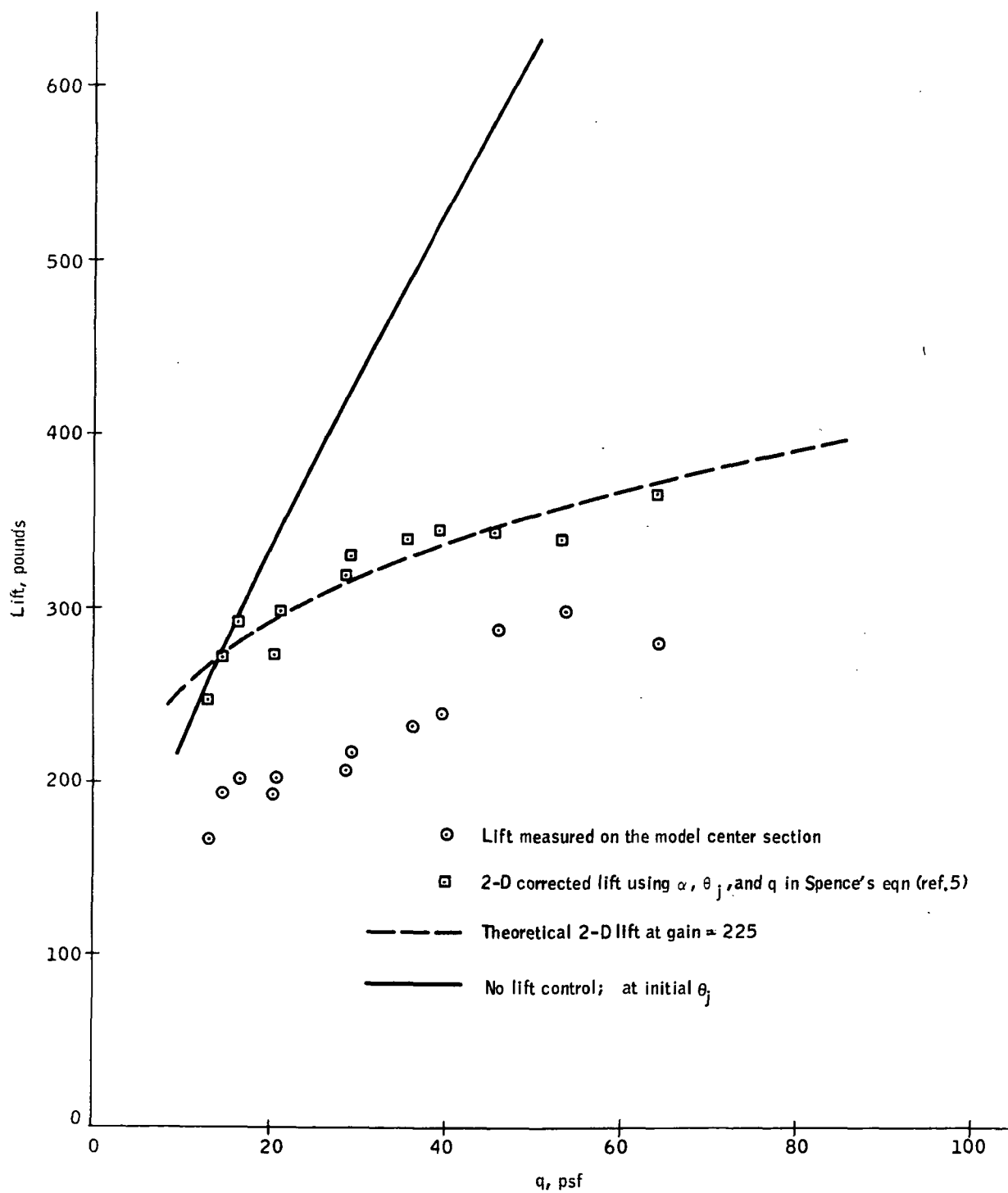


Figure 64. VDT-Blade Lift Variation with Free-Stream Dynamic Pressure - $\alpha = 12$ degrees

can be estimated that the fluidic control system was approximately 82% effective in maintaining a constant lift.

Dynamic Tests

Initially, tests were conducted using the helicopter VDT-blade model to determine the aerodynamic response to time-variable jet angles. A fluidic function generator was connected to the lift controller circuitry in the model center section and used to sinusoidally vary the jet angle for frequencies up to 30 Hz. However, waveforms of the test results showed extraneous signals on the measured normal and chord forces, and the results were inconsistent. These extraneous signals were apparently caused by structural flexibility and mode coupling associated with the internal balance system and model wind tunnel support structure. This resulted in adverse resonance phenomena, and the test results were invalid and not used.

In conjunction with the above tests, dynamic tests were conducted using the center section of the VDT-blade model with one 5 x 8-foot endplate to determine finite-aspect-ratio effects on dynamic lift. This model configuration had an effective aspect ratio of approximately 2.1 (ref. 11) and was attached to the LTV balance system that was used during the Phase I wind tunnel tests (ref. 2). The dynamic valve used for the Phase I dynamic tests was used to oscillate the jet angle at frequencies from 5 to 40 Hz.

Two components of lift on the model were measured as a function of time, as shown in Figure 65. When the resonance effects were subtracted out, two of which were the model-model support structure torsional and flapping modes (at 8 Hz and 24 Hz, respectively), the dynamic lift components were found to be constant up to 20 Hz.

Total lift, as seen in Figure 66, was obtained by taking the difference between the two lift components, since they were 180 degrees out of phase up to a frequency of 24 Hz. Above 24 Hz, the waveforms and phase relationships are complicated by cross-coupling between the drag and lift components.

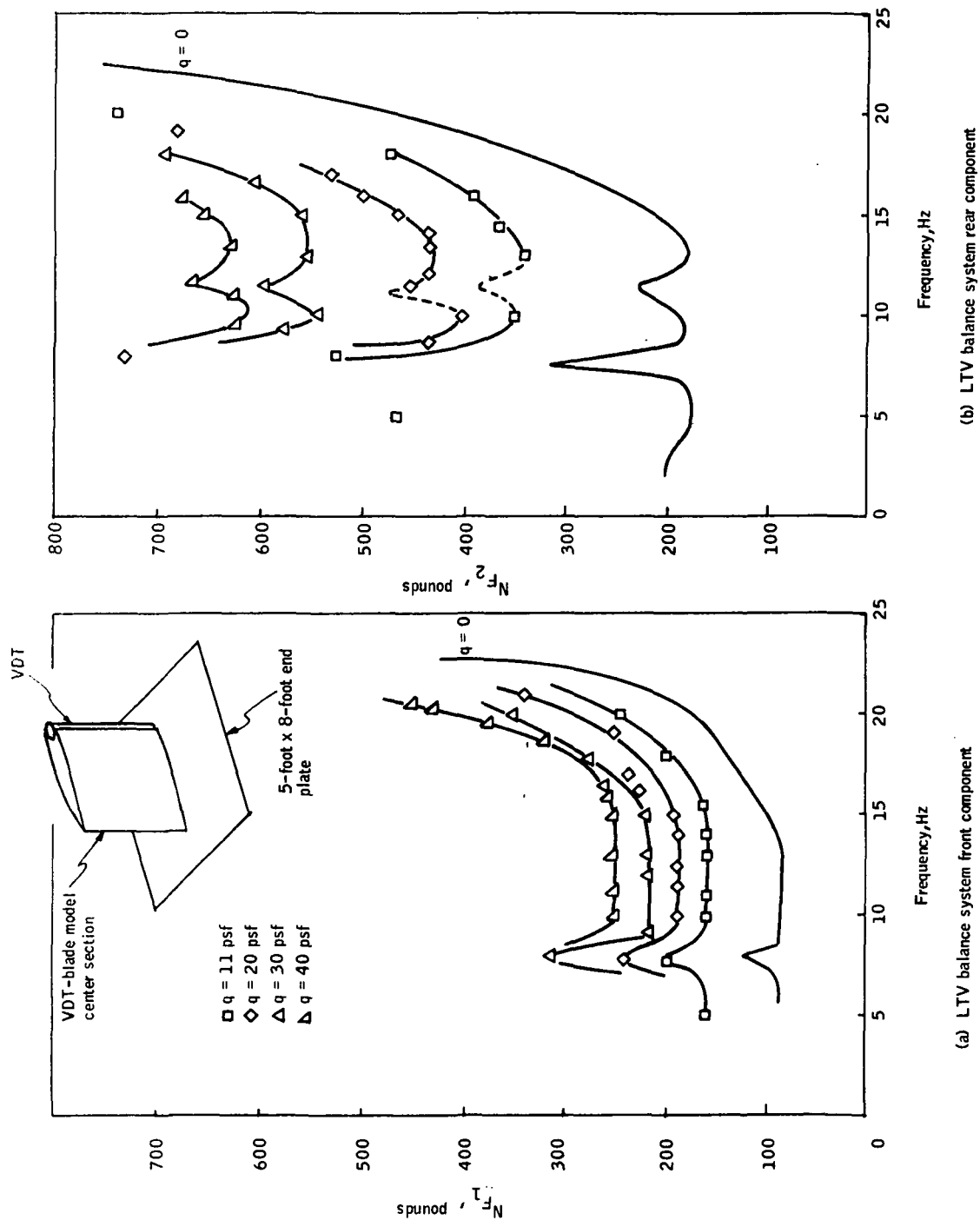


Figure 65. Normal Force as a Function of Jet-Angle Oscillation Frequency

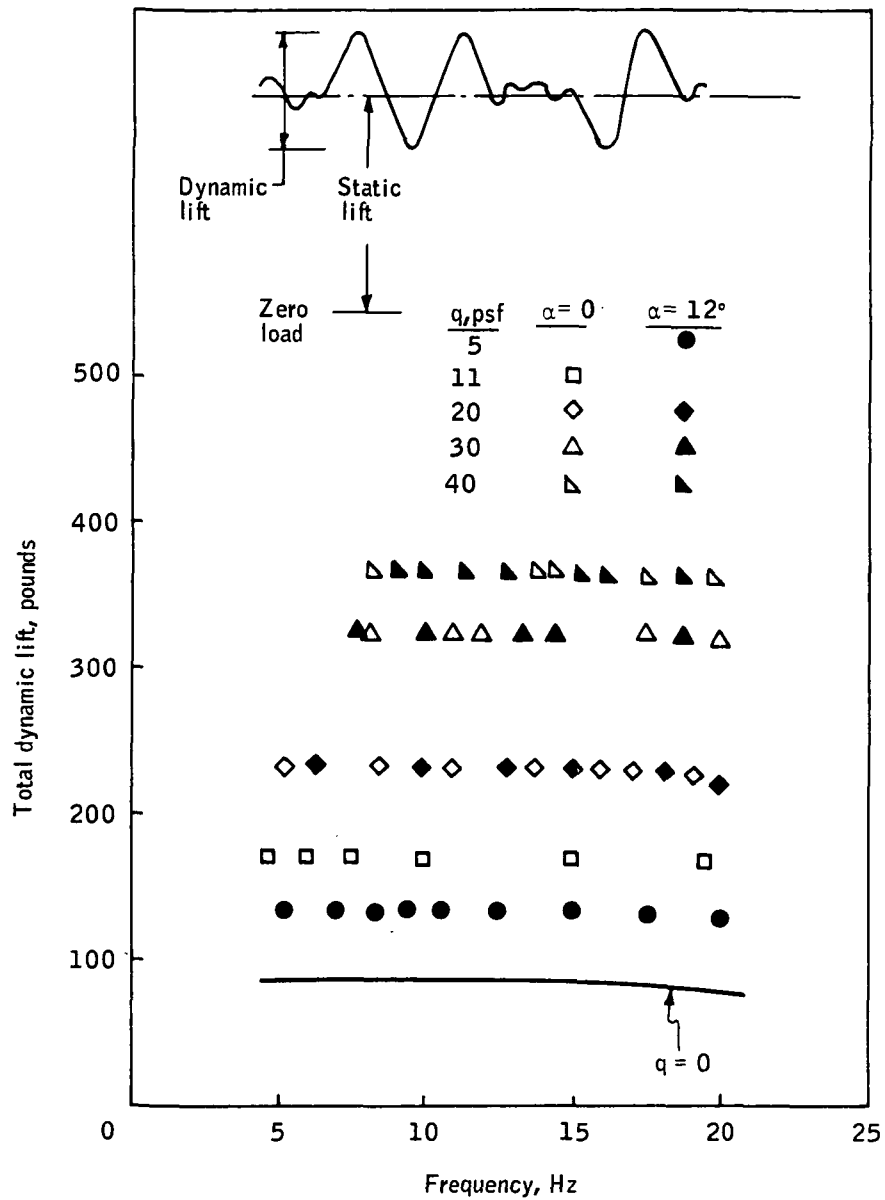


Figure 66. Variation of Dynamic Lift with Jet-Angle Oscillation Frequency

Therefore, only data at frequencies up to 20 Hz were considered sufficiently valid for determining the dynamic lift characteristics. The dynamic lift coefficient, $|C_L|$, as computed from the results of Figure 66, is plotted in Figure 67 versus reduced frequency for three values of blowing coefficient.

For the Phase I dynamic tests it was found that the maximum jet angle decreased as the frequency of oscillation was increased, so the dynamic lift coefficient was divided by a normalized jet angle correction factor, $|\Delta\theta_j|/\Delta\theta_j$, to eliminate the effect of jet angle roll-off (ref. 2). Oil traces taken at 5, 12 and 20 Hz during these dynamic tests to determine the maximum jet angle indicate a jet angle roll-off similar to that observed for the Phase I tests. This is shown in Figure 68 where the maximum dynamic jet angle, $|\Delta\theta_j|$, has been normalized by the maximum jet angle at 5 Hz. This curve shows that the maximum jet angle at 20 Hz is approximately 58% of the maximum jet angle at 5 Hz or that the initial maximum jet angle of 170 degrees at 5 Hz falls off to 100 degrees at 20 Hz.

The curves of Figure 67 were divided by the normalized maximum jet angle, $|\Delta\theta_j|/\Delta\theta_j$, of Figure 68 and crossplotted in Figure 69 to indicate the dynamic lift coefficient with no jet angle roll-off. These curves were extrapolated back to a reduced frequency of zero to give the steady-state (i. e., jet angle fixed at maximum amplitude) value of the dynamic lift coefficient. Figure 70 shows the experimental lift-coefficient/blowing-coefficient relationship for steady-state testing of the center-section/single-endplate configuration at various jet angles and zero angle of attack. Also plotted in Figure 70 are the steady-state lift coefficients from Figure 69. Figure 70 indicates that the steady-state jet angle is approximately 90 degrees (included jet angle of 180 degrees) for all blowing coefficients and compares favorably with the included jet angle of 170 degrees determined by using oil traces at a jet oscillation frequency of 5 Hz.

The curves of Figure 69 were normalized by the steady-state lift coefficients and replotted in Figure 71. The curves for angles of attack of 0 and

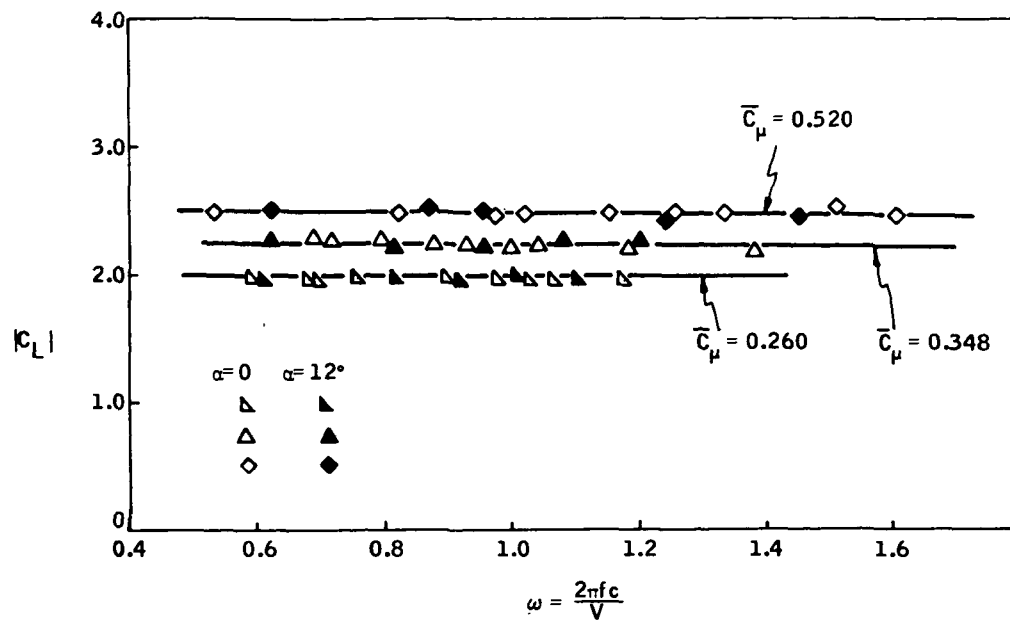


Figure 67. Variation of Uncorrected Coefficient of Lift Amplitude with Reduced Frequency - $\alpha = 0$ and 12 degrees

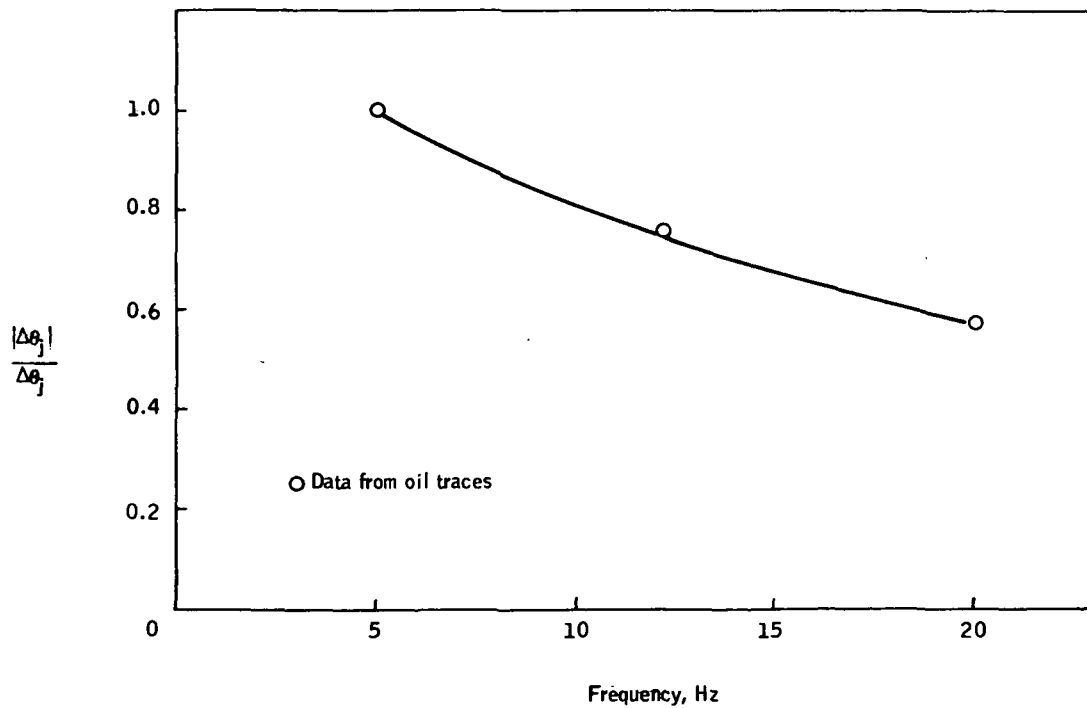


Figure 68. Jet-Angle Correction Factor

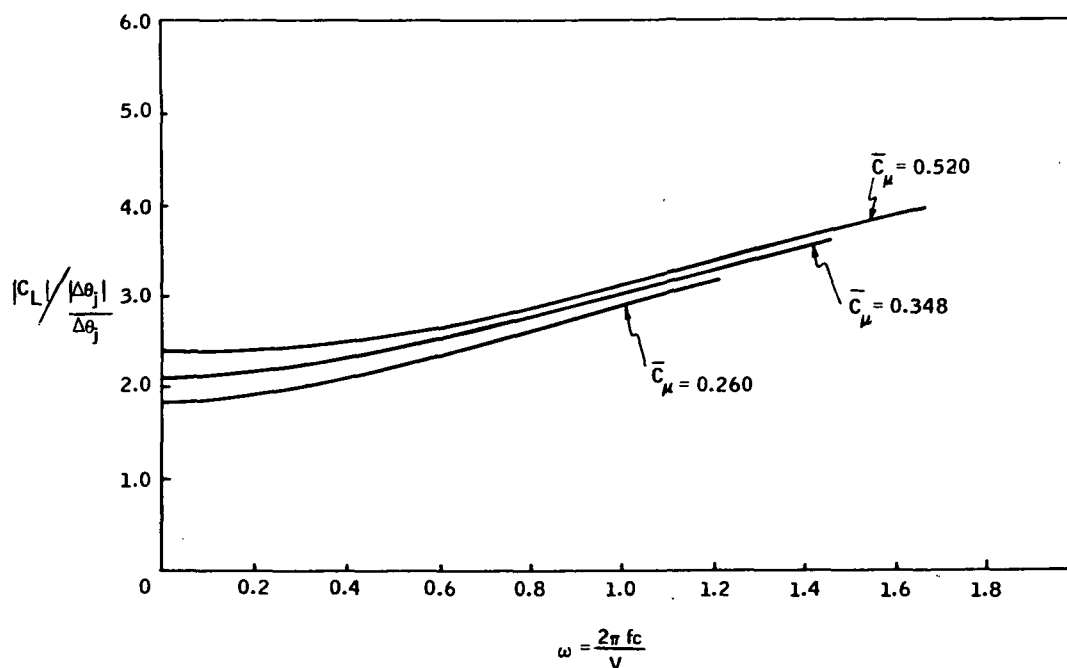


Figure 69. Variation of Corrected Coefficient-of-Lift Amplitude with Reduced Frequency - $\alpha = 0$ and 12 degrees

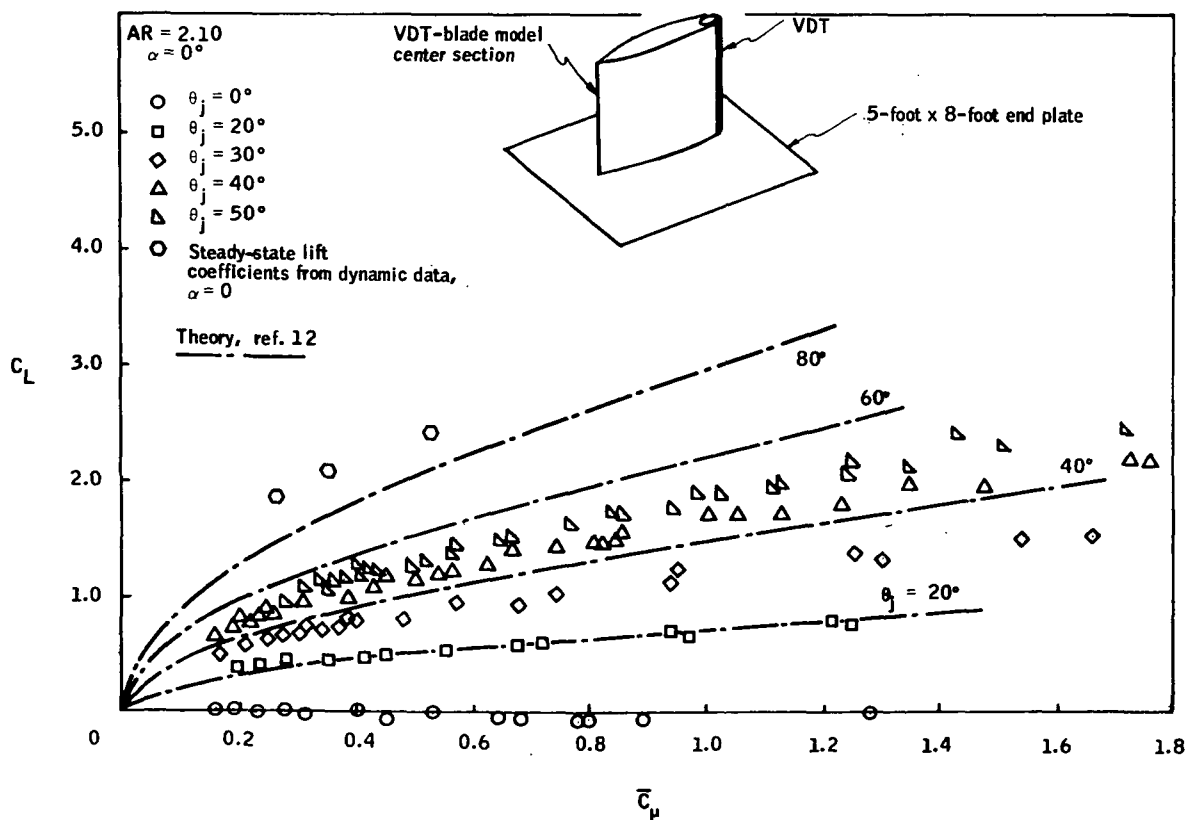


Figure 70. Steady-State Lift-Coefficient/Blowing-Coefficient Relationship for Tests of Center Section with a Single Endplate

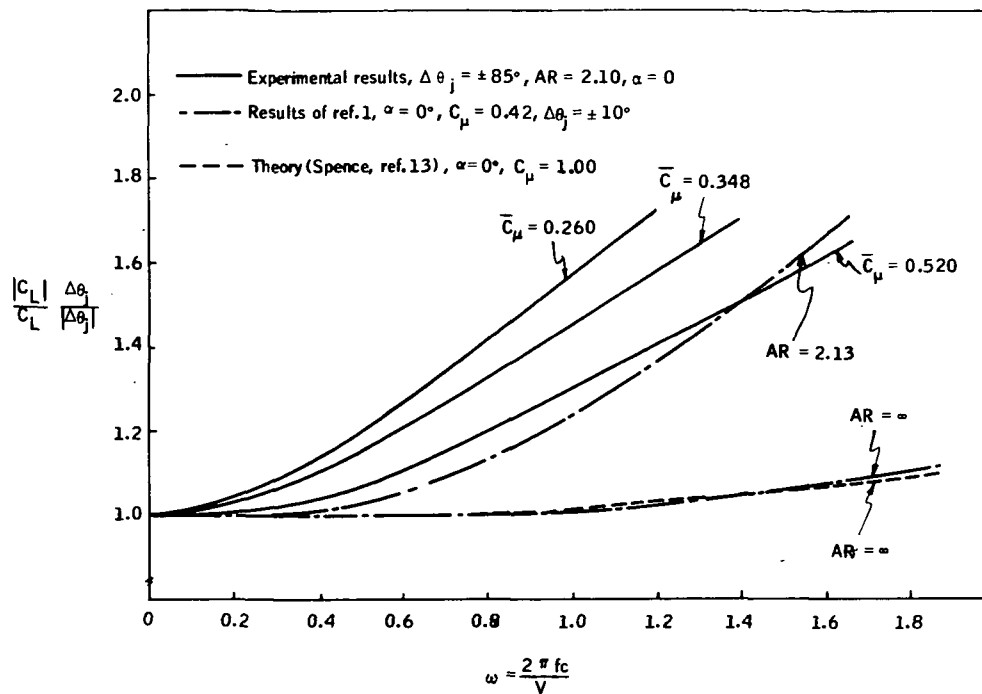


Figure 71. Variation of Normalized Coefficient-of-Lift Amplitude with Reduced Frequency - $\alpha = 0$

12 degrees indicate that the normalized coefficient of lift amplitude decreases with increasing blowing coefficient and increases with increasing reduced frequency.

The experimental results plotted in Figure 71 may be compared with the experimental results of Takeuchi (ref. 1). Takeuchi's results for $AR = 2.13$ and $AR = \infty$ are plotted in Figure 71 along with Spence's theory for $AR = \infty$ (ref. 13). Takeuchi's results show close agreement with Spence's theory and indicate that the effect of finite aspect ratio is to increase the dynamic lift coefficient. The experimental results for the VDT-blade center section configuration exhibit higher dynamic lift coefficients for $AR = 2.10$ than Takeuchi's results for $AR = 2.13$, but this difference should result from the differences in maximum jet angles, $\Delta\theta_j = \pm 10$ degrees in Takeuchi's tests and $\Delta\theta_j = \pm 85$ degrees in the VDT-blade tests.

CONCLUSIONS

In general, the conclusions drawn from these investigations are the same as those found for the Phase I tests of reference 2 and will not be repeated.

However, in addition to conclusions previously drawn, it can be seen from the experimental and theoretical results presented in this report that the idea of sensing and controlling lift with a fluidic control system is feasible. Problems encountered with the outbleed system were unexpected and resulted in a system gain lower than originally intended; but the results have demonstrated that the fluidic amplifier circuit is capable of handling the pressure gains required to provide adequate lift control. More work is needed to develop accurate lift-sensing techniques under three-dimensional conditions.

REFERENCES

1. Takeuchi, Kunihiro, "Two- and Three-Dimensional Unsteady Lift Measurements of Jet-Flapped Wings." M.S. Thesis, Pennsylvania State University, June, 1970.
2. Rose, R. E., Hammer, J. M., and Kizilos, A. P., "Feasibility Study of a Bidirectional Jet Flap Device for Application to Helicopter Rotor Blades," Phase I Final Report. NASA-CR 114359 (Honeywell Document No. 12081-FR1, Honeywell Inc.), July 1971.
3. Kuchemann, D., "A Method for Calculating the Pressure Distribution Over Jet-Flapped Wings." Royal Aircraft Establishment Report No. Aero 2573, 1956. (Also, Aero Res. Council, R and M, No. 3036, 1957.)
4. Yuan, S. W., Westkaemper, J. C., Kemp, L. D., Richter, W. L., "Investigation of Circulation Control Airfoils by Means of Jets." USA AVLABS Technical Report 66-72, 1966.
5. Spence, D. A., "The Lift Coefficient of a Thin Jet-Flapped Wing," Proceedings of the Royal Society, Series A, Vol. 238, No. 1212, pp. 46-68, 1956.
6. Merrill, G. L., "Operational Information for AARL VDT Fluidic Control System." MR-10902, Honeywell Inc., April 1970.
7. Pope, Alan, "Basic Wing and Airfoil Theory," First Edition, McGraw-Hill Book Co., Inc., 1951.
8. Abbott, Ira H., and VonDoenhoff, Albert E., "Theory of Wing Sections," Dover Publications, Inc., 1959.
9. Critzos, Chris C., Heyson, Harry H., and Boswinkle, Robert W. Jr., "Aerodynamic Characteristics of NACA 0012 Airfoil Section at Angles of Attack from 0° to 180°. NACA TN 3364, Jan. 1955.
10. Smith, G. A., Hammer, J. M., and Rose, R. E., "Conceptual Study to Apply Advanced Flight Technology to the COIN or TRIM Aircraft." Honeywell Document No. 12225-FR(R), Honeywell Inc., June 1971.
11. Williams, J., and Alexander, A. I., "Three-Dimensional Wind Tunnel Tests of a 30° Jet Flap Model." ARC-17990, Perf. 1399, FM 2326 S and C 3049, November 1956.
12. McCormick, Barnes W., Jr., "Aerodynamics of V/STOL Flight", Academic Press Inc., New York, 1967.

13. Spence, D. A., "The Flow Past a Thin Wing With an Oscillating Jet-Flap." Rep. Aero 2690, Royal Aircraft Establishment, August 1964.
14. Bailey, R. G., and Hammer, J. M., "Helicopter Application Studies of the Variable Deflection Thruster." Final Report to Office of Naval Research, Honeywell Document 12153-FR1(R), August 1970.

APPENDIX

LIFT CONTROLLER MATH MODEL

This analysis concerns the method for determining the effect of the gain of the fluidic control system on the left error of the system for various states. The effect of the nonlinearities of the aerodynamics such as indicated by equation (A-3) will be included. The state of the system is defined by the value of four pressure differences specified at various points in the control system (see Figure A-1). The four pressure differences are: $\Delta P_{c/2}$ (the pressure difference across the midchord), ΔP_{ref} (the controlling reference pressure), ΔP_{LE} (ΔP_{LE} = lift error = $\Delta P_{ref} - \Delta P_{c/2}$), and ΔP_T (pressure difference between the VDT supply tanks). The underlying principle of the control system is that the lift per unit span is proportional to the pressure difference at the midchord. The controller design is intended to drive the jet angle to keep this wing pressure difference ($\Delta P_{c/2}$) as close as possible to the reference pressure difference (ΔP_{ref}).

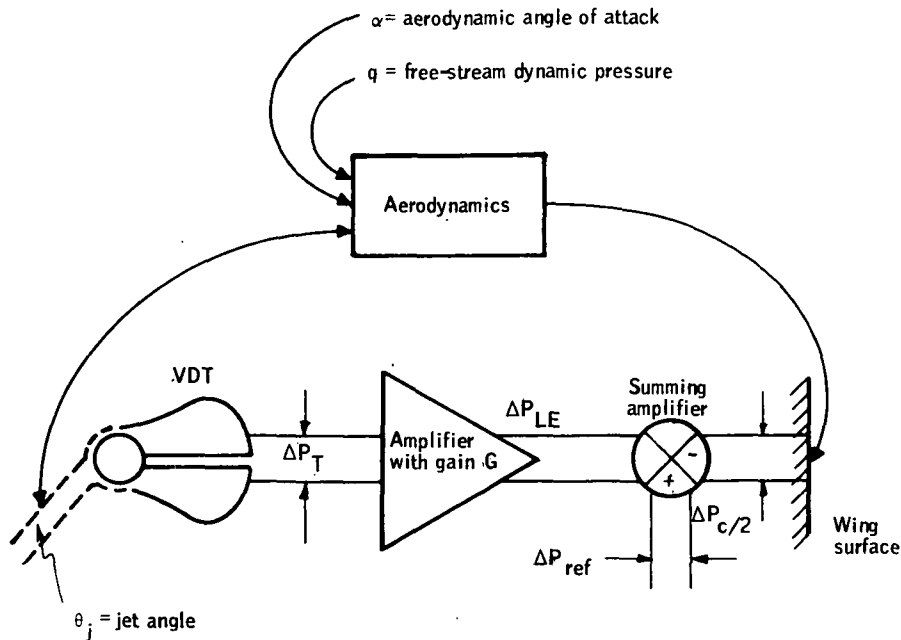


Figure A-1. Fluidic Control System

The system parameters varied during the wind tunnel tests were angle of attack (α), jet angle (θ_j), and test section Mach number (M_∞). The equations which represent the various components of the system shown in Figure A-1 are written for an initial and final set of system parameters (α , θ_j , M_∞). It will be shown that compatibility between initial and final states leads to a nonlinear equation in the unknown jet angle in the final state. When this equation is solved, the final state variables can be determined, and the lift error in the final state can be found

For the initial parameters

$$\begin{aligned}\alpha &= \alpha_I \\ \theta_j &= \theta_I \\ M_\infty &= M_I\end{aligned}\tag{A-1}$$

All the control system state variables can be determined

$$C_{L_I} = C_L(\alpha_I, \theta_I, \bar{C}_{\mu_I})\tag{A-2}$$

The formula for C_L was obtained from a curve fit of previously measured wind tunnel data (see reference 14 for the details of the curve fit formula). This data was taken at essentially infinite aspect ratio so that the results of this analysis will only approximate the actual test conditions, which were conducted for center-section blowing only. The curve fit formula used was

$$\begin{aligned}C_L(\alpha, \theta, \bar{C}_\mu) &= f(\bar{C}_\mu) \left(\frac{\alpha}{2} + \theta_j \right) + 0.11\alpha + 0.75\bar{C}_\mu \sin(\alpha + \theta_j) \\ f(\bar{C}_\mu) &= 3.03 \bar{C}_\mu^{1/2} + 0.40 \bar{C}_\mu - 0.21 \bar{C}_\mu^{3/2}\end{aligned}\tag{A-3}$$

The blowing coefficient \bar{C}_μ is defined as

$$\bar{C}_\mu = \frac{T}{qS}\tag{A-4}$$

where T is the jet thrust. Inherent in proportional fluidic control is the fact that the jet thrust is constant for all jet angles. Thus, for this analysis the blowing coefficient will vary only with q :

$$q_I = \frac{\gamma}{2} P_\infty M_I^2 \quad (A-5)$$

and the lift per unit area is

$$l_I = C_L q_I \quad (A-6)$$

As was mentioned earlier, the fundamental principle of the control system is that the lift is proportional to the midchord pressure difference. The proportionality constant was determined experimentally (ref. 2) to be

$$\Delta P_{c/2_I} = 0.656 l_I \quad (A-7)$$

To determine ΔP_{T_I} from θ_I , the available formulas which relate ΔP_T to θ_j must be inverted. This inversion cannot be performed algebraically, so a Newton's method iteration subroutine was written. This iterative function will be denoted by the following expression:

$$\Delta P_{T_I} = \Delta P_T(\theta_I) \quad (A-8)$$

and from Figure A-1 we have

$$\Delta P_{LE_I} = \Delta P_{T_I} / G \quad (A-9)$$

$$\Delta P_{ref} = \Delta P_{c/2_I} + \Delta P_{LE_I} \quad (A-10)$$

Thus, we have expressed all four state variables in terms of α_I , θ_I , and M_I . Now, if the system is taken to a new state with reference pressure held constant and parameters α_F , θ_F , and M_F , the three remaining variables can be calculated in the new state:

$$\bar{C}_{\mu_F} = \bar{C}_{\mu_I} (M_I/M_F)^2 \quad (A-11)$$

$$C_{L_F} = C_L (\alpha_F, \theta_F, \bar{C}_{\mu_F}) \quad (A-12)$$

$$q_F = \frac{\gamma}{2} P_\infty M_F^2 \quad (A-13)$$

$$L_F = C_{L_F} q_F \quad (A-14)$$

$$\Delta P_{c/2_F} = 0.656 L_F \quad (A-15)$$

$$\Delta P_{LE_F} = \Delta P_{ref} - \Delta P_{c/2_F} \quad (A-16)$$

$$\Delta P_{T_F} = \Delta P_T (\theta_F) \quad (A-17)$$

$$\Delta P_{LE_F} = \Delta P_{T_F} / G \quad (A-18)$$

Notice that we have two expressions for ΔP_{LE_F} . These two expressions can be combined to eliminate ΔP_{LE_F} and the resulting compatibility equation can be solved for the unknown jet angle θ_F .

Thus:

$$\Delta P_{T_F} / G = \Delta P_{ref} - \Delta P_{c/2_F} \quad (A-19)$$

or using equations (A-10) through (A-18), (A-19) becomes

$$\Delta P_T (\theta_F) / G = \Delta P_{ref} - 0.656 C_L (\alpha_F, \theta_F, \bar{C}_{\mu_F}) \frac{\gamma}{2} P_\infty M_F^2 \quad (A-20)$$

As discussed before, $\Delta P_T (\theta_F)$ is an iterative function itself, so that direct determination of a solution to (A-20) by numerical methods is impractical. The solution technique used to find θ_F will be based on physical insight into the system.

If the system is taken from initial to final state with no change in jet angle, the change in lift will be

$$L_I - L_F = C_{L_I} q_I - C_L (\alpha_F, \theta_I, \bar{C}_{\mu_F}) q_F \quad (A-21)$$

or

$$\Delta C_L' = C_{L_I} (q_I/q_F) - C_L (\alpha_F, \theta_I, \bar{C}_{\mu_F}) \quad (A-22)$$

where

$$\Delta C_L' = \frac{L_I - L_F}{q_F}$$

From Figure A-1 we have

$$\Delta P_{ref} = \Delta P_{c/2} + \Delta P_{LE} \quad (A-23)$$

or

$$\Delta P_{ref} = \Delta P_{c/2_I} + \Delta P_{LE_F} \quad (A-24)$$

$$\Delta P_{ref} = \Delta P_{c/2_F} + \Delta P_{LE_F}$$

and therefore,

$$\Delta P_{LE_I} - \Delta P_{LE_F} = \Delta P_{c/2_I} - \Delta P_{c/2_F} \quad (A-25)$$

from (A-7)

$$\frac{\Delta P_{LE_I} - \Delta P_{LE_F}}{0.656} = L_I - L_F \quad (A-26)$$

and from (A-6)

$$\frac{\Delta P_{LE_I} - \Delta P_{LE_F}}{0.656 q_F} = C_{L_I} - C_{L_F} = \Delta C_L \quad (A-27)$$

Thus, ΔC_L is the actual change in lift coefficient which will occur.

The error in the lift coefficient ($\Delta C_L''$) in the final state is

$$\Delta C_L'' = \Delta C_L' - \Delta C_L \quad (A-28)$$

but also

$$\Delta C_L'' = C_{L_I} (q_I/q_F) - C_L (\alpha_F, \theta_F, \bar{C}_{\mu_F}) \quad (A-29)$$

Equations (A-28) and (A-29) form the basis of the calculation. The iterative calculation proceeds from an initial guess for θ_F (usually θ_I). Equations (A-28) and (A-29) are evaluated using the θ_F calculated from the previous iteration. Then θ_F is adjusted to make (A-29) agree exactly with (A-28), and then (A-28) and (A-29) are again evaluated with the improved value of θ_F . The iteration proceeds until Equation (A-20) is satisfied to within a predetermined accuracy limit. The method used to modify θ_F to make (A-29) and (A-28) agree was taken from Appendix F of reference 14. This method was written to deal with lift changes in coefficient form, so that (A-28) and (A-29) were written in coefficient form also.